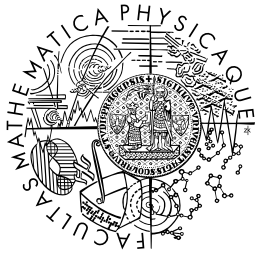

FACULTY
OF MATHEMATICS
AND PHYSICS
Charles University

DOCTORAL THESIS

Štěpán Marek

Electronic Structure Effects in Molecular Junctions

Department of Condensed Matter Physics

Supervisor of the doctoral thesis: Ing. Richard Korytár, Ph. D.

Study programme: Condensed Matter Physics and Materials Research

Study branch: Physics

Prague 2023

I declare that I carried out this doctoral thesis independently, and only with the cited sources, literature and other professional sources. It has not been used to obtain another or the same degree.

I understand that my work relates to the rights and obligations under the Act No. 121/2000 Sb., the Copyright Act, as amended, in particular the fact that the Charles University has the right to conclude a license agreement on the use of this work as a school work pursuant to Section 60 subsection 1 of the Copyright Act.

In ..... date ....

Author's signature

I wish to thank my supervisor Richard Korytár for many insights over the four years of my Ph. D. program and for introducing me to the molecular junctions community. I also wish to thank Dr. Jan Wilhelm and Prof. Ferdinand Evers for many insightful discussions and together with Prof. Wulf Wulfhekel for the formulation of the problem of rotating molecule. Furthermore, I would like to thank Dr. Marius Buerkle for answering my many queries about the software I used during my studies.

Finally, I would like to thank my family and friends for their support during my time as PhD student.

Title: Electronic Structure Effects in Molecular Junctions

Author: Štěpán Marek

Department: Department of Condensed Matter Physics

Supervisor: Ing. Richard Korytár, Ph. D., Department of Condensed Matter Physics

Abstract: Molecular electronics is a field investigating transport and transport induced phenomena on the one of the smallest functional circuit components - molecules. In this work, we explore the effect of electronic structure effects on the conductance and rotation of the molecules in the junction. We use density functional theory, *GW* approximation and simple analytical models to understand experimentally observed phenomena and warn about possible drawbacks of adapting *GW* for cluster based conductance calculations.

Keywords: molecular junctions *GW* DFT molecular conductance

Contents

1. Introduction

1.1 Molecular Electronics

The miniaturisation of electronics lead to great advancements in availability and utility of electronic devices in the last century[1]. The current size of transistors is in order of nanometres [2]. At this scale, quantum effects due to the wavefunctions of moving electrons become apparent and dictate the transport properties. While this poses a challenge to the design and manufacture of transistor chips, a new field known as molecular electronics emerged from the need to accurately describe electron transport in quantum regime inside nanoscale systems coupled to mesoscopic/macroscopic reservoirs.

The goal of molecular electronics is not necessarily to design better transistors, but rather to describe fundamental physics inherent to these systems. Indeed, many interesting physical phenomena occur in molecular junctions, interested reader might find review[3] useful. The effects range from electronic structure influences on the conductance of junctions to correlated transport phenomena and mechanical effects.

At present, the molecular electronics field has somewhat matured - the experimental and theoretical methods for the study are tested, with theoretical predictions usually giving qualitatively correct description of the observed phenomena, but precise quantitative agreements remain elusive[3].

From experimental methods, we mention the molecular break junction (MBJ) technique, which uses piezoelectric bending to form a nanogap in conducting wires that can be occupied by a molecule[1], or scanning tunnelling microscopy (STM) technique, which scans the STM tip across a conducting surface with adsorbed molecules.

Among the theoretical methods, the numerical calculations proved to be indispensable to increase the accuracy of the predictions, taking into account many degrees of freedom of the molecular junction system - the molecule hybridises with the electrodes, changing the electronic structure of the molecule and the electrode tips[1], leading to significant corrections to the observed properties. The junction system is inherently an open, (slightly) out of equilibrium system and the non-equilibrium Green's function methods (NEGF) are used to describe the system response to external voltage[1, 3].

The precise study of the electronic structure of the molecules inside junctions and linking of the electronic properties to observed transport effects is the broad focus of this work. More specifically, we investigate the effects of molecular structure of two types of molecules and the associated observed properties of the molecular junctions. Furthermore, we discuss possible improvements to numerical calculations and their possible drawbacks. These problems are now introduced in more detail.

1.2 Ferrocene Molecular Junction

Ferrocene is an organometallic molecule with conjugated electron structure, consisting of two cyclopentadiene rings connected by an iron ion (see Fig. 1.1). It

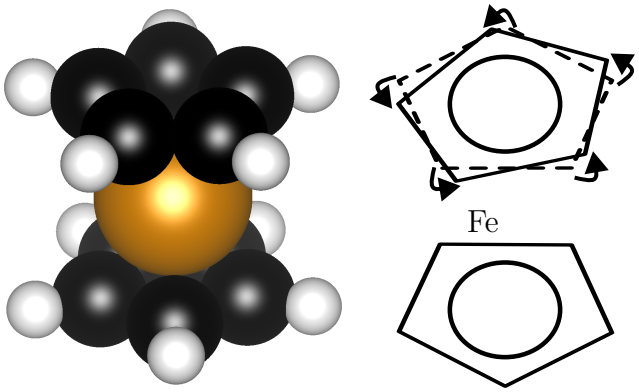

(a) (b)

Figure 1.1: A three dimensional model (a) and schematic electronic structure (b) of the ferrocene molecule. The carbon atoms are in black, hydrogen atoms are in white and iron atom is in dark orange. The rings and the iron form a conjugated system. The rings can rotate with respect to each other, as depicted in (b).

was previously shown to exhibit destructive interference in electronic transport[4] for specific rotations of the two carbon rings (see Fig. 1.1b for illustration of ring rotation).

We here discuss a possibility for different mode of electron transport across the ferrocene molecule - without the linker groups, ferrocene interacts with the metallic electrodes directly. This notion is motivated by relatively high conductance observed in MBJ experiments, as is presented in a our joined experimental-theoretical paper[5]. This mode of electron transport produces molecular conductance independent of relative cyclopentadiene ring rotation. Instead, the transport seems to occur directly through the iron atom which hybridises with the atoms of the electrode tip.

We calculate the electronic structure of the extended molecule (molecule + part of electrodes) using density functional theory[6] (DFT) with dispersion corrections[7] to evaluate the energy of the junction. Applying the NEGF formalism, we evaluate the conductance of the junction and we investigate the local density of states (LDOS) and the shape of molecular orbitals to motivate our conclusions.

1.3 Helical Molecules

Chiral molecules are molecules whose mirror image is structurally different from the original molecule. Such molecules exhibit interesting properties in molecular junctions, for example they induce spin filtering of the transported electrons, resulting in famous chirality induced spin selectivity effect (CISS effect)[8].

Typical example of chiral molecule is a helical molecule[9]. We here however explore a different type of helicity - helicity in the electronic structure of the molecule rather than in the geometry of atomic nuclei. Helical molecular orbitals are present in one-dimensional conjugated systems such as cumulenes[10, 11] or linkers in "Geländer"-type molecules[12] (see Fig. 1.2 for illustration).

The Geländer molecules are of special interest to us as they have been observed

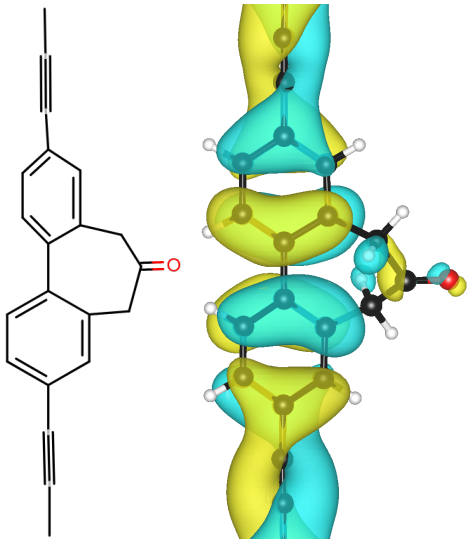

(a) Chemical structure (b) Example of molecular orbital

Figure 1.2: (a) Schematic structure of the symmetrized version of the Geländer molecule. The linker between the two benzene cores has incommensurate length, causing the cores to be rotated with respect to each other. Such non-planar part of the molecule induces ring currents and orbital helicity around the triple bonds (see (b) for detail) at the edges of the molecule.

to rotate under current flow from STM tip to the molecules mounted on a tripod structure attached to metallic surface [13]. We investigate the electronic structure of these molecules and present arguments based on electronic momentum transfer to the molecules that can explain the most puzzling feature of the rotations - the rotation direction remains the same irrespective of the current direction.

1.4 *GW* Approximation for Metallic Clusters

One of the possible ways to further enhance accuracy of the numerical modelling of molecular junctions is the application of the *GW* approximation[14] for calculation of the electronic structure. The *GW* approximation tries to build upon the DFT and fix some of its problems, namely inaccuracies in the determination of the charged gap[3, 15, 16]. Such inaccuracies are especially damning to attempts to evaluate molecular conductance, as the conductance can change by orders of magnitude for small changes in energy of the excited states of the molecule.

Some calculations have been realized previously[17], but to our knowledge, when applying *GW* in cluster based junction calculation, convergence of the observables with the size of the electrode cluster has not been investigated. On a model metallic electrodes, consisting of sodium atoms, we investigate the quasiparticle spectrum in eigenvalue-only *GW*[15] (ev*GW*) and determine that the finite size of the cluster induces an artificially increased gap that would not be present in the wire of realistic size. Such increase might lead to unphysical decrease in conductance, overshadowing the possible increase in the accuracy given by the ev*GW* calculation.

2. Theory

For our purposes of study of molecular junctions, we shall use mainly four observables - the total current through the junction under steady state conditions, the current density in steady state conditions with the associated angular momentum and the local density of states. In this section, we derive expressions for these observables in the NEGF framework, with notation mostly inspired by [1] and [18]. We work in SI units, which introduces some factors of $\hbar$ to certain Green's function expressions, see A.1 for details.

The model for the effectively non-interacting, coherent transport through molecular junctions has a form of tight-binding[19] system representing the molecular junction separated into three subsystems - the left electrode (here usually marked by lower index L), the molecule and the right electrode (here usually marked by the lower index R). As we will show, this model is generalizable by assuming different forms of self-energy to model the influence of the electrodes on the molecule [20]. Such model assumes that the electrons in the molecule and electrodes can be modelled as effectively non-interacting, with the Hamiltonian operator $\hat{H}$ in second quantisation given as follows[1]

$$\hat{H} = \overbrace{\sum_{j\in L} \epsilon_j \hat{a}_j^\dagger \hat{a}_j}^{\hat{H}_L} + \overbrace{\sum_{p\in R} \epsilon_p \hat{a}_p^\dagger \hat{a}_p}^{\hat{H}_R} + \overbrace{\sum_{\alpha\in M} \epsilon_\alpha \hat{a}_\alpha^\dagger \hat{a}_\alpha}^{\hat{H}_M} + \tag{2.1}$$

$$+ \overbrace{\sum_{j\in L,\alpha\in M} t_{\alpha j}\left(\hat{a}_\alpha^\dagger \hat{a}_j + \hat{a}_j^\dagger \hat{a}_\alpha\right)}^{\hat{H}_{LM}} + \overbrace{\sum_{p\in R,\alpha\in M} t_{\alpha p}\left(\hat{a}_\alpha^\dagger \hat{a}_p + \hat{a}_p^\dagger \hat{a}_\alpha\right)}^{\hat{H}_{RM}}, \tag{2.2}$$

where we implicitly take the operators to be evaluated at the same time t and $\hat{H}_L$ is the uncoupled left-electrode Hamiltonian, $\hat{H}_R$ is the uncoupled right electrode Hamiltonian and $\hat{H}_M$ is the uncoupled molecule Hamiltonian. The electrodes are coupled by tight-binding terms $\hat{H}_{(L/R)M}$ to the molecule. The $\hat{a}$ and $\hat{a}^\dagger$ operators are fermionic annihilation and creation operators, respectively, of the true many body eigenstates of the electrode/molecule systems. We use indices $j, k, l, ...$ to indicate degrees of freedom of the left electrode, indices $p, q, r, ...$ to indicate degrees of freedom of the right electrode and $\alpha, \beta, \gamma, ...$ to indicate degrees of freedom of the molecule. The fermionic operators follow the anticommutation relation

$$\left\{\hat{a}_j(t), \hat{a}_k^\dagger(t)\right\} = \delta_{jk} \tag{2.3}$$

and same for all other types of indices. All other anticommutators for creation/annihilation operators at the same time are zero. Given this Hamiltonian, the three observables of interest are now explored.

2.1 Total Charge Current through the Junction

Under the assumption of steady state solution for small non-equilibrium [1], we can assume that the current through the molecule will be given by the decrease

of the number of electrons in the left electrode (for current direction from left to right), i.e.

$$\hat{I}(t) = (-e)\left(-\frac{\partial \hat{n}_L}{\partial t}\right) = e\frac{\partial \hat{n}_L}{\partial t}\,, \tag{2.4}$$

where $\hat{n}_L(t) = \sum_{j\in L} \hat{a}_j^\dagger(t)\hat{a}_j(t)$ is the total number operator in the left electrode. The time derivative of the operator follows from the Schrödinger equation in Heisenberg representation [18]

$$\frac{\partial \hat{n}_L}{\partial t} = \frac{i}{\hbar}\left[\hat{H}, \hat{n}_L\right](t)\,. \tag{2.5}$$

Inspecting the form of $\hat{H}$ ((2.1) and (2.2)), we can see that only $\hat{H}_L$ and $\hat{H}_{LM}$ have operators that can produce non-commuting results the $\hat{n}_L$ operator, since all other terms include pairs of exactly anticommuting operators. The commutation with $\hat{H}_L$ is trivial (implicitly assuming same time evaluation in the following equations)

$$\begin{aligned}
\left[\hat{H}_L, \hat{n}_L\right] &= \sum_{j,k\in L} \epsilon_j \left[\hat{a}_j^\dagger\hat{a}_j, \hat{a}_k^\dagger\hat{a}_k\right] = \sum_{j,k} \epsilon_j \left(\hat{a}_j^\dagger\hat{a}_j\hat{a}_k^\dagger\hat{a}_k - \hat{a}_k^\dagger\hat{a}_k\hat{a}_j^\dagger\hat{a}_j\right) = \\
&= \sum_{j,k} \epsilon_j \left(\hat{a}_j^\dagger\hat{a}_j\hat{a}_k^\dagger\hat{a}_k - \hat{a}_k^\dagger\left(-\hat{a}_j^\dagger\hat{a}_k + \delta_{jk}\right)\hat{a}_j\right) = \\
&= \sum_{j,k} \epsilon_j \left(\hat{a}_j^\dagger\hat{a}_j\hat{a}_k^\dagger\hat{a}_k + \hat{a}_j^\dagger\hat{a}_k^\dagger\hat{a}_j\hat{a}_k - \hat{a}_k^\dagger\hat{a}_j\delta_{jk}\right) = \\
&= \sum_{j,k} \epsilon_j \left(\hat{a}_j^\dagger\hat{a}_j\hat{a}_k^\dagger\hat{a}_k + \hat{a}_j^\dagger\left(-\hat{a}_j\hat{a}_k^\dagger + \delta_{jk}\right)\hat{a}_k - \hat{a}_k^\dagger\hat{a}_j\delta_{jk}\right) = \\
&= \sum_{jk} \epsilon_j\delta_{jk}\left(\hat{a}_j^\dagger\hat{a}_k - \hat{a}_k^\dagger\hat{a}_j\right) = 0\,.
\end{aligned} \tag{2.6}$$

Therefore, the only two non-trivial commutators to evaluate following from $\hat{H}_{LM}$ are

$$\begin{aligned}
\left[\hat{a}_\alpha^\dagger\hat{a}_j, \hat{a}_k^\dagger\hat{a}_k\right] &= \hat{a}_\alpha^\dagger\hat{a}_j\hat{a}_k^\dagger\hat{a}_k - \hat{a}_k^\dagger\hat{a}_k\hat{a}_\alpha^\dagger\hat{a}_j = \hat{a}_\alpha^\dagger\hat{a}_j\hat{a}_k^\dagger\hat{a}_k + \hat{a}_\alpha^\dagger\hat{a}_k^\dagger\hat{a}_j\hat{a}_k = \\
&= \hat{a}_\alpha^\dagger\hat{a}_j\hat{a}_k^\dagger\hat{a}_k + \hat{a}_\alpha^\dagger\left(-\hat{a}_j\hat{a}_k^\dagger + \delta_{jk}\right)\hat{a}_j = \hat{a}_\alpha^\dagger\hat{a}_j\delta_{jk}
\end{aligned} \tag{2.7}$$

and

$$\begin{aligned}
\left[\hat{a}_j^\dagger\hat{a}_\alpha, \hat{a}_k^\dagger\hat{a}_k\right] &= \hat{a}_j^\dagger\hat{a}_\alpha\hat{a}_k^\dagger\hat{a}_k - \hat{a}_k^\dagger\hat{a}_k\hat{a}_j^\dagger\hat{a}_\alpha = \hat{a}_j^\dagger\hat{a}_\alpha\hat{a}_k^\dagger\hat{a}_k - \hat{a}_k^\dagger\left(-\hat{a}_j^\dagger\hat{a}_k + \delta_{jk}\right)\hat{a}_\alpha = \\
&= \hat{a}_j^\dagger\hat{a}_\alpha\hat{a}_k^\dagger\hat{a}_k + \hat{a}_j^\dagger\hat{a}_k^\dagger\hat{a}_\alpha\hat{a}_k - \hat{a}_k^\dagger\hat{a}_\alpha\delta_{jk} = -\hat{a}_k^\dagger\hat{a}_\alpha\delta_{jk}\,.
\end{aligned} \tag{2.8}$$

Therefore

$$\begin{aligned}
\left[\hat{H}_{LM}, \hat{n}_L\right] &= \sum_{\alpha\in M;j,k\in L} t_{\alpha j}\left[\hat{a}_\alpha^\dagger\hat{a}_j, \hat{a}_k^\dagger\hat{a}_k\right] + t_{\alpha j}\left[\hat{a}_j^\dagger\hat{a}_\alpha, \hat{a}_k^\dagger\hat{a}_k\right] = \\
&= \sum_{\alpha\in M;j\in L} t_{\alpha j}\hat{a}_\alpha^\dagger\hat{a}_j - t_{\alpha j}\hat{a}_j^\dagger\hat{a}_\alpha\,.
\end{aligned} \tag{2.9}$$

Overall, we have therefore

$$\hat{I}(t) = e\frac{\partial \hat{n}_L}{\partial t} = \frac{ei}{\hbar}\left[\hat{H}, \hat{n}_L\right] = \frac{ei}{\hbar}\sum_{\alpha\in M;j\in L} t_{\alpha j}\hat{a}_\alpha^\dagger(t)\hat{a}_j(t) - t_{\alpha j}\hat{a}_j^\dagger(t)\hat{a}_\alpha(t)\,. \tag{2.10}$$

Since the Hamiltonian does not depend explicitly on time, Green's function is only a function of the time difference $(t - t')$ (see A.1 for details). Therefore, the expectation value of the current operator is given in terms of lesser Green's function

$$G^<_{ij}(t - t') = \frac{i}{\hbar} \left\langle \hat{a}^\dagger_i(t')\hat{a}_j(t) \right\rangle \,, \tag{2.11}$$

which leads to

$$\left\langle \hat{I}(t) \right\rangle = e \sum_{\alpha \in M; j \in L} t_{\alpha j} G^<_{\alpha j}(0) - t_{j\alpha} G^<_{\alpha j}(0) \,, \tag{2.12}$$

so we can see that the current is time independent - represents a steady state solution.

For systems for which the spectrum ϵ_α is known, it is useful to transform to energy dependent Green's functions via Fourier transform [18]. This is done as

$$\begin{aligned} G^<_{jk}(t) &= \int_{-\infty}^{\infty} \frac{d\omega}{2\pi} e^{-i\omega t} G^<_{jk}(\hbar\omega) = \int_{-\infty}^{\infty} \frac{dE}{2\pi\hbar} e^{-i\frac{E}{\hbar}t} G^<_{jk}(E) \\ &= \frac{1}{h} \int_{-\infty}^{\infty} dE e^{-i\frac{E}{\hbar}t} G^<_{jk}(E) \,. \end{aligned} \tag{2.13}$$

Hence we can determine the current as

$$\left\langle \hat{I} \right\rangle = \frac{e}{h} \int_{-\infty}^{\infty} dE \sum_{\alpha \in M; j \in L} t_{\alpha j} G^<_{\alpha j}(E) - t_{\alpha j} G^<_{j\alpha}(E) \,. \tag{2.14}$$

In this form, the Green's function still explicitly contains indices referring to the (left) electrode. This can in fact be reformulated so that only elements of Green's function in the subspace of the molecule are involved. In order to do that, we need to determine the Green's function of the model more explicitly. We can use the equation of motion (EoM) method [18] to proceed.

2.1.1 Determining Junction Green's Functions via Equation of Motion Method

Equation of motion method is formulated for retarded Green's function (see A.1) as follows - we take the derivative of the retarded Green's function and try to close the hierarchy of newly generated Green's functions. Because the Hamiltonian in (2.2) is quadratic, this hierarchy will be closed already in the first step.

To determine the current via $G^<$ as in (2.14), we need retarded Green's function elements of form

$$G^R_{j\alpha}(t) = \frac{-i}{\hbar} \theta(t) \langle \{ \hat{a}_j(t), \hat{a}^\dagger_\alpha(0) \} \rangle \quad . \tag{2.15}$$

Taking the derivative and multiplying by $i\hbar$

$$i\hbar \frac{\partial}{\partial t} G^R_{j\alpha}(t) = \delta(t) \langle \{ \hat{a}_j(t), \hat{a}^\dagger_\alpha \} \rangle + \theta(t) \langle \{ \frac{\partial \hat{a}_j}{\partial t}, \hat{a}^\dagger_\alpha \} \rangle \,. \tag{2.16}$$

The time derivative of the operator is again determined by the Schrödinger equation[18]

$$\frac{\partial \hat{a}_j}{\partial t} = \frac{i}{\hbar}\left[\hat{H}, \hat{a}_j\right](t) = \sum_{j'} \frac{i\epsilon_{j'}}{\hbar}\left[\hat{a}^\dagger_{j'}\hat{a}_{j'}, \hat{a}_j\right] + \sum_{j',\alpha'} \frac{it_{\alpha' j'}}{\hbar}\left[\hat{a}^\dagger_{j'}\hat{a}_{\alpha'}, \hat{a}_j\right] . \tag{2.17}$$

We now decompose the commutator into anticommutators[18]

$$\left[\hat{a}^\dagger_{j'}\hat{a}_{\alpha'}, \hat{a}_j\right] = \hat{a}^\dagger_{j'}\{\hat{a}_{\alpha'}, \hat{a}_j\} - \{\hat{a}^\dagger_{j'}, \hat{a}_j\}\hat{a}_{\alpha'} = -\delta_{jj'}\hat{a}_{\alpha'} \tag{2.18}$$

$$\left[\hat{a}^\dagger_{j'}\hat{a}_{j'}, \hat{a}_j\right] = \hat{a}^\dagger_{j'}\{\hat{a}_{j'}, \hat{a}_j\} - \{\hat{a}^\dagger_{j'}, \hat{a}_j\}\hat{a}_{j'} = -\delta_{jj'}\hat{a}_{j'} , \tag{2.19}$$

where we used the fermionic anticommutation canonical quantisation conditions (2.3). Hence

$$\frac{\partial \hat{a}_j}{\partial t} = \frac{-i}{\hbar}\left(\epsilon_j \hat{a}_j + \sum_{\alpha'} t_{\alpha' j}\hat{a}_{\alpha'}\right) . \tag{2.20}$$

Substituting back into (2.16) and recognizing

$$\delta(t)\langle\{\hat{a}_j(t), \hat{a}^\dagger_\alpha\}\rangle = \delta(t)\langle\{\hat{a}_j, \hat{a}^\dagger_\alpha\}\rangle = 0 , \tag{2.21}$$

as the molecular indices α never overlap with (left) electrode indices j, we have

$$i\hbar\frac{\partial}{\partial t}G^R_{j\alpha} = \epsilon_j G^R_{j\alpha}(t) + \sum_{\alpha'} t_{\alpha' j} G^R_{\alpha',\alpha} . \tag{2.22}$$

Fourier transforming to energy domain leads to [18]

$$(E + i\eta - \epsilon_j)G^R_{j\alpha}(E) = \sum_{\alpha'} t_{\alpha' j} G^R_{\alpha',\alpha}(E) . \tag{2.23}$$

Notice that this equation enables us to write $G^R_{j\alpha}(E)$ purely in terms of spectrum of the uncoupled reservoir ϵ_j, coupling constants $t_{\alpha',j}$ and the Green's function restricted to the molecule subspace. Furthermore, we can recognize the matrix structure and Green's function of the uncoupled electrode

$$g^R_{jj'}(E) = \frac{\delta_{jj'}}{E + i\eta - \epsilon_j} \tag{2.24}$$

in order to write

$$G^R_{j\alpha}(E) = \sum_{j'\alpha'} g^R_{jj'}(E) t_{\alpha' j'} G^R_{\alpha',\alpha}(E) . \tag{2.25}$$

Similarly, we can derive the Green's function elements in the opposite order

$$i\hbar\frac{\partial}{\partial t}G^R_{\alpha j} = \theta(t)\left\langle\left\{\hat{a}_\alpha, \frac{\partial}{\partial t}(\hat{a}^\dagger_j(-t))\right\}\right\rangle . \tag{2.26}$$

Here, we can determine

$$\frac{\partial}{\partial t}(\hat{a}^\dagger_j(-t)) = \frac{\partial}{\partial t}e^{-\frac{i}{\hbar}\hat{H}t}\hat{a}^\dagger_j e^{\frac{i}{\hbar}\hat{H}t} = \frac{-i}{\hbar}\left[\hat{H}, \hat{a}^\dagger_j\right](-t) . \tag{2.27}$$

We again determine the commutator

$$\left[\hat{H}, \hat{a}_j^\dagger\right] = \sum_{j'} \epsilon_{j'} \left[\hat{a}_{j'}^\dagger \hat{a}_{j'}, \hat{a}_j^\dagger\right] + \sum_{\alpha', j'} t_{\alpha' , j'} \left[\hat{a}_{\alpha'}^\dagger \hat{a}_{j'}, \hat{a}_j^\dagger\right] = \epsilon_j \hat{a}_j^\dagger + \sum_{\alpha'} t_{\alpha' j} \hat{a}_{\alpha'}^\dagger \,. \tag{2.28}$$

Substituting back leads to

$$i\hbar \frac{\partial}{\partial t} G_{\alpha j}^R = \epsilon_j G_{\alpha j}^R(t) + \sum_{\alpha'} t_{\alpha' j} G_{\alpha \alpha'}^R(t) \,. \tag{2.29}$$

Finally, transforming to energy domain and reordering the terms leads to

$$G_{\alpha j}^R(E) = \sum_{\alpha', j'} G_{\alpha \alpha'}^R(E) t_{\alpha' j'} g_{j' j}^R(E) \,. \tag{2.30}$$

Therefore, we have expressed Green's function elements present in the current formula (2.14) via elements in the subspace of the molecule only. Solving the equation of motion for these elements of the Green's function further shows that the uncoupled reservoir Green's functions are present in the self-energy

$$\begin{aligned} i\hbar \frac{\partial}{\partial t} G_{\alpha \alpha'}^R = \delta(t)\delta_{\alpha\alpha'} + \epsilon_\alpha G_{\alpha\alpha'}^R + \sum_j t_{\alpha j} G_{j\alpha'}^R + \sum_p t_{\alpha p} G_{p\alpha'}^R = \\ = \delta(t)\delta_{\alpha\alpha'} + \epsilon_\alpha G_{\alpha\alpha'}^R + \sum_{j j' \alpha''} t_{\alpha j} g_{j j'}^R t_{j' \alpha''} G_{\alpha'' \alpha'}^R + \sum_{p p' \alpha''} t_{\alpha p} g_{p p'}^R t_{\alpha'' p'} G_{\alpha'' \alpha'}^R \,. \end{aligned} \tag{2.31}$$

We can recognize this as a form of Dyson equation with self-energies due to left and right electrode added together

$$\Sigma_{L/R, \alpha\alpha'}^R = \sum_{p/j, p'/j'} t_{\alpha p/j} g_{p/j, p'/j'}^R t_{\alpha' p'/j'} \,. \tag{2.32}$$

We define the matrices in the subspace of the molecule as

$$\left(\boldsymbol{G}^R(E)\right)_{\alpha\alpha'} = G_{\alpha\alpha'}^R(E) \tag{2.33}$$

in order to rewrite the equation of motion for the molecular Green's function as

$$\left(\boldsymbol{G}^R(E)\right)^{-1} = E\boldsymbol{I} - \boldsymbol{\epsilon} - \boldsymbol{\Sigma}_L^R - \boldsymbol{\Sigma}_R^R \,, \tag{2.34}$$

where $(\boldsymbol{\epsilon})_{\alpha\alpha'} = \epsilon_\alpha \delta_{\alpha\alpha'}$ and $\boldsymbol{I}$ is the identity matrix.

In order to determine the lesser Green's function, we need to analytically continue the expressions (2.25) and (2.30) onto the Keldysh contour. This results in [21]

$$G_{j\alpha}^< (E) = \sum_{\alpha' j'} g_{j j'}^R(E) t_{\alpha' j'} G_{\alpha' \alpha}^<(E) + g_{j j'}^<(E) t_{\alpha' j'} G_{\alpha' j}^A(E) \tag{2.35}$$

$$G_{\alpha j}^< (E) = \sum_{\alpha' j'} G_{\alpha \alpha'}^R(E) t_{\alpha' j'} g_{j' j}^<(E) + G_{\alpha\alpha'}^<(E) t_{\alpha' j'} g_{j' j}^A(E) \,. \tag{2.36}$$

To determine the lesser Green's function in the molecular subspace, we use the steady state approximation [21, 1] to generalized Kadanoff-Baym equation as

$$G_{\alpha\alpha'}^< = \sum_{\beta\beta'} G_{\alpha\beta}^R \left(\Sigma_{L,\beta\beta'}^< + \Sigma_{R,\beta\beta'}^<\right) G_{\beta'\alpha'}^A \,. \tag{2.37}$$

Substituting into (2.14) results in

$$\left\langle \hat{I} \right\rangle = \frac{e}{h} \int dE \sum_{\alpha\alpha',jj'} \Big(G^R_{\alpha\alpha'} t_{\alpha' j'} g^<_{j'j} t_{\alpha j} + \\ + \sum_{\beta\beta'} G^R_{\alpha\beta} \left(\Sigma^<_{L,\beta\beta'} + \Sigma^<_{R,\beta\beta'} \right) G^A_{\beta'\alpha'} t_{\alpha' j'} g^A_{j'j} t_{\alpha j} - \\ - \sum_{\beta\beta'} t_{\alpha j} g^R_{jj'} t_{\alpha' j'} G^R_{\alpha'\beta} \left(\Sigma^<_{L,\beta\beta'} + \Sigma^<_{R,\beta\beta'} \right) G^A_{\beta'\alpha} - t_{\alpha j} g^<_{jj'} t_{\alpha' j} G^A_{\alpha'\alpha} \Big) \,, \tag{2.38}$$

where the energy dependence is implied for the Green's functions and self-energies. Recognizing the self-energies, we can leave only matrices restricted to the molecular subspace and write

$$\left\langle \hat{I} \right\rangle = \frac{e}{h} \int dE \, \mathrm{Tr} \left(\boldsymbol{G}^R \boldsymbol{\Sigma}^<_L + \boldsymbol{G}^R \left(\boldsymbol{\Sigma}^<_L + \boldsymbol{\Sigma}^<_R \right) \boldsymbol{G}^A \boldsymbol{\Sigma}^A_L - \\ - \boldsymbol{\Sigma}^<_L \boldsymbol{G}^A - \boldsymbol{\Sigma}^R_L \boldsymbol{G}^R \left(\boldsymbol{\Sigma}^<_L + \boldsymbol{\Sigma}^<_R \right) \boldsymbol{G}^A \right) \,, \tag{2.39}$$

where Tr denotes trace over the molecular states.

The lesser self-energies are proportional to uncoupled reservoir lesser Green's function (see A.1 for details), and hence can be written as

$$\boldsymbol{\Sigma}^<_{L/R} = \left(\boldsymbol{\Sigma}^A_{L/R} - \boldsymbol{\Sigma}^R_{L/R} \right) f_{L/R} \,, \tag{2.40}$$

where $f_{L/R}$ is the Fermi-Dirac distribution of the left/right reservoir. Hence

$$\left\langle \hat{I} \right\rangle = \frac{e}{h} \int dE \, \mathrm{Tr} \Big(\left(\boldsymbol{\Sigma}^A_L - \boldsymbol{\Sigma}^R_L \right) \Big(f_L \left[\boldsymbol{G}^R - \boldsymbol{G}^A + \boldsymbol{G}^R \left(\boldsymbol{\Sigma}^A_L - \boldsymbol{\Sigma}^R_L \right) \boldsymbol{G}^A \right] + \\ + \, f_R \boldsymbol{G}^R \left(\boldsymbol{\Sigma}^A_R - \boldsymbol{\Sigma}^R_R \right) \boldsymbol{G}^A \Big) \Big) \,. \tag{2.41}$$

Here, we can recognize

$$\boldsymbol{G}^R - \boldsymbol{G}^A + \boldsymbol{G}^R \left(\boldsymbol{\Sigma}^A_L - \boldsymbol{\Sigma}^R_L \right) \boldsymbol{G}^A = \boldsymbol{G}^R \left((\boldsymbol{G}^A)^{-1} - (\boldsymbol{G}^R)^{-1} + \boldsymbol{\Sigma}^A_L - \boldsymbol{\Sigma}^R_L \right) \boldsymbol{G}^A \,. \tag{2.42}$$

Substituting from (2.34) leads to

$$\boldsymbol{G}^R - \boldsymbol{G}^A + \boldsymbol{G}^R \left(\boldsymbol{\Sigma}^A_L - \boldsymbol{\Sigma}^R_L \right) \boldsymbol{G}^A = \tag{2.43}$$

$$= \boldsymbol{G}^R \left(\boldsymbol{\Sigma}^R_R + \boldsymbol{\Sigma}^R_L - \boldsymbol{\Sigma}^A_R - \boldsymbol{\Sigma}^A_L + \boldsymbol{\Sigma}^A_L - \boldsymbol{\Sigma}^R_L \right) \boldsymbol{G}^A = \\ = \boldsymbol{G}^R \left(\boldsymbol{\Sigma}^R_R - \boldsymbol{\Sigma}^R_A \right) \boldsymbol{G}^A \,. \tag{2.44}$$

Hence, for the current, we have

$$\left\langle \hat{I} \right\rangle = \frac{e}{h} \int dE \, \mathrm{Tr} \left(\left(\boldsymbol{\Sigma}^A_L - \boldsymbol{\Sigma}^R_L \right) \boldsymbol{G}^R \left(\boldsymbol{\Sigma}^R_R - \boldsymbol{\Sigma}^A_R \right) \boldsymbol{G}^A \right) \left(f_L - f_R \right) \,. \tag{2.45}$$

Defining the anti-hermitian part of the advanced self-energy as

$$\boldsymbol{\Gamma}^A_{L/R} = i \left(\boldsymbol{\Sigma}^A_{L/R} - \boldsymbol{\Sigma}^R_{L/R} \right) \tag{2.46}$$

we can write the familiar Landauer formula[1] for total current through junction

$$\left\langle \hat{I} \right\rangle = \frac{e}{h} \int_{-\infty}^{\infty} dE \overbrace{\mathrm{Tr}\left(\mathbf{\Gamma}_L^A \boldsymbol{G}^R(E) \mathbf{\Gamma}_R^A \boldsymbol{G}^A(E) \right)}^{T(E)} \left(f_L(E) - f_R(E) \right) , \tag{2.47}$$

where $T(E)$ is the so-called transmission function. The problem of determining the expected current through junction therefore becomes the problem of determining the transmission function, which involves Green's functions restricted to the molecular subspace with self-energy that includes the effect of coupling to the electrodes. This self-energy can be approximated by a variety of assumptions, here we mostly apply wide band approximation as formulated in [20]. Since the spectrum of the (extended) molecule can be determined by numerical methods, the only free parameters are used to determine the form of self-energy, and for sufficiently large electrodes should not influence the junction properties[22].

2.2 Current Density

Besides the total current, the spatially resolved current density is also of interest to us. In this work, it is mainly used to derive the angular momentum associated with the current. Hence, we only investigate particle current density instead of charge current density, as the angular momentum is independent of the charge of the particles. A single particle current density operator has the following form [23]

$$\hat{j}_S(\boldsymbol{r}, t) = \frac{1}{2m} \left\{ \delta(\hat{r} - \boldsymbol{r}), \hat{p} \right\} (t) , \tag{2.48}$$

where $\hat{p}$ is the momentum operator and $\hat{r}$ is the position operator. For a state $|\alpha\rangle$ with wavefunction $\langle \boldsymbol{r} | \alpha \rangle = \psi_\alpha(\boldsymbol{r})$, the current density results in the familiar conserved current

$$\begin{aligned} \langle \alpha | \hat{j}_S(\boldsymbol{r}, t) | \alpha \rangle &= \frac{1}{2m} \left(\psi_\alpha^*(\boldsymbol{r}, t) \langle \boldsymbol{r} | \hat{p}(t) | \alpha \rangle + \langle \alpha | \hat{p}(t) | \boldsymbol{r} \rangle \psi_\alpha(\boldsymbol{r}, t) \right) = \\ &= \frac{-i\hbar}{2m} \left(\psi_\alpha^*(\boldsymbol{r}, t) \nabla \left[\psi_\alpha(\boldsymbol{r}, t) \right] - \psi_\alpha(\boldsymbol{r}, t) \nabla \left[\psi_\alpha^*(\boldsymbol{r}, t) \right] \right) , \end{aligned} \tag{2.49}$$

where we moved the time dependence to wavefunctions in order to show the familiar form of the conserved current in the Schrödinger equation.

In a many particle system, the current density is obtained as summation over current densities of all single particle states. Therefore, it can be written as [18]

$$\hat{j}(\boldsymbol{r}, t) = \sum_{\alpha,\beta} \langle \alpha | \hat{j}_S(\boldsymbol{r}, 0) | \beta \rangle \hat{a}_\alpha^\dagger(t) \hat{a}_\beta(t) , \tag{2.50}$$

where we returned to the Heisenberg representation. Evaluating the matrix element of the single-particle operator explicitly

$$\hat{j}(\boldsymbol{r}, t) = \sum_{\alpha,\beta} \frac{-i\hbar}{2m} \left(\psi_\alpha^*(\boldsymbol{r}) \nabla \left[\psi_\beta(\boldsymbol{r}) \right] - \psi_\beta(\boldsymbol{r}) \nabla \left[\psi_\alpha^*(\boldsymbol{r}) \right] \right) \hat{a}_\alpha^\dagger(t) \hat{a}_\beta(t) . \tag{2.51}$$

For eigenstates of the many-body Hamiltonian, the expectation value of the current density is stationary and is given by lesser Green's function

$$\left\langle \hat{j}(\boldsymbol{r},t)\right\rangle = \left\langle \hat{j}(\boldsymbol{r})\right\rangle = \sum_{\alpha,\beta} \frac{\hbar^2}{2m} \left(\nabla\left[\psi^*_\alpha(\boldsymbol{r})\right]\psi_\beta - \psi^*_\alpha(\boldsymbol{r})\nabla\left[\psi_\beta(\boldsymbol{r})\right]\right) G^<_{\alpha\beta}(t=0)\,. \tag{2.52}$$

Again, we express the Green's function in the energy domain as

$$\left\langle \hat{j}(\boldsymbol{r})\right\rangle = \int_{-\infty}^{\infty} \frac{dE}{2\pi\hbar} \underbrace{\sum_{\alpha,\beta} \frac{\hbar^2}{2m} \left(\nabla\left[\psi^*_\alpha(\boldsymbol{r})\right]\psi_\beta - \psi^*_\alpha(\boldsymbol{r})\nabla\left[\psi_\beta(\boldsymbol{r})\right]\right) G^<_{\alpha\beta}(E)}_{\left\langle \hat{j}(\boldsymbol{r},E)\right\rangle}\,. \tag{2.53}$$

Expressing the lesser Green's function as in (2.37) and the lesser self-energy as in (2.40), we obtain[22]

$$\boldsymbol{G}^<(E) = i\boldsymbol{G}^R(E)\left(\boldsymbol{\Gamma}^A_R f_R(E) + \boldsymbol{\Gamma}^A_L f_L(E)\right)\boldsymbol{G}^A(E)\,. \tag{2.54}$$

When the junction is under bias, the left and the right electrodes no longer have coinciding chemical potential, leading to non-zero difference $f_L(E) - f_R(E)$ at least for some E. The interval of E where the difference is non-zero is called the transport window here. The current density difference in the biased and the equilibrium situation can then be determined as

$$\begin{aligned}\left\langle \hat{j}_{\text{bias}}(\boldsymbol{r},E) - \hat{j}_{\text{eq.}}(\boldsymbol{r},E)\right\rangle = \sum_{\alpha,\beta} \frac{i\hbar^2}{2m} \left(\nabla\left[\psi^*_\alpha(\boldsymbol{r})\right]\psi_\beta(\boldsymbol{r}) - \psi^*_\alpha(\boldsymbol{r})\nabla\psi_\beta(\boldsymbol{r})\right) \sum_{\alpha',\beta'} \times \\ \times\, G^R_{\alpha\alpha'}(E)\left(\Gamma^A_{L,\alpha'\beta'}(E)\left[f_{L,\text{bias}}(E) - f_{L,\text{eq.}}(E)\right] + \right. \\ \left. +\, \Gamma^A_R\left[f_{R,\text{bias}}(E) - f_{R,\text{eq.}}(E)\right]\right) G^A_{\beta'\beta}(E)\,.\end{aligned} \tag{2.55}$$

In the STM case (which is where we use the current density observable in this work), we usually vary only one electrodes potential, and the other remains fixed. Explicitly, for varying chemical potential of the left electrode, we have $f_{L,\text{eq.}}(E) = f_{R,\text{eq.}}(E) = f_{R,\text{bias}}$, which leads to only the term proportional to

$$f_{L,\text{bias}}(E) - f_{L,\text{eq.}}(E) = f_{L,\text{bias}}(E) - f_{R,\text{bias}}(E) \tag{2.56}$$

being non-zero. We usually drop the bias notation and redefine the current density as the non-equilibrium contribution only

$$\begin{aligned}\left\langle \hat{j}(\boldsymbol{r},E)\right\rangle = \sum_{\alpha,\beta} \frac{i\hbar^2}{2m} \left(\nabla\left[\psi^*_\alpha(\boldsymbol{r})\right]\psi_\beta(\boldsymbol{r}) - \psi^*_\alpha(\boldsymbol{r})\nabla\psi_\beta(\boldsymbol{r})\right) \times \\ \times \left(\boldsymbol{G}^R(E)\boldsymbol{\Gamma}^A_L(E)\boldsymbol{G}^A(E)\right)_{\alpha\beta} \left(f_L(E) - f_R(E)\right)\,,\end{aligned} \tag{2.57}$$

where we used the matrix notation as before. We can see that the transport window determines the contributions from the Green's functions, same as in the case of formula for total current (2.47).

2.2.1 Angular Momentum

We can relate the current density to angular momentum in the system as follows. The single particle angular momentum operator has three components defined by

$$\hat{L}_{j,S} = \epsilon_{jkl}\hat{r}_j k\hat{p}_l \, . \tag{2.58}$$

Note that the position and momentum component operators commute here, as the Levi-Civita symbol ϵ_{jkl} does not allow for the components in the same direction. Hence, the many-body operator associated with angular momentum is given as

$$\begin{aligned}\hat{L}_j(t) &= \sum_{\alpha,\beta}\langle\alpha|\epsilon_{jkl}\hat{r}_j\hat{p}_l|\beta\rangle\hat{a}^\dagger_\alpha(t)\hat{a}_\beta(t) = \\ &= \sum_{\alpha,\beta}\hat{a}^\dagger_\alpha\hat{a}_\beta\epsilon_{jkl}\int d^3r\psi^*_\alpha(\boldsymbol{r})r_j\langle\boldsymbol{r}|\hat{p}_l|\beta\rangle = \\ &= -i\hbar\sum_{\alpha,\beta}\hat{a}^\dagger_\alpha\hat{a}_\beta\epsilon_{jkl}\int d^3r\psi^*_\alpha(\boldsymbol{r})r_j\left(\partial_l\psi_\beta(\boldsymbol{r})\right) \, .\end{aligned} \tag{2.59}$$

Since the angular momentum is an observable, we can make the Hermiticity more apparent by setting

$$\begin{aligned}\hat{L}_j(t) &= \frac{1}{2}\left(\hat{L}_j(t) + \hat{L}^\dagger_j(t)\right) = \\ &= \frac{-i\hbar}{2}\epsilon_{jkl}\sum_{m,n}\int d^3r\left(\hat{a}^\dagger_\alpha\hat{a}_\beta r_k\psi^*_\alpha(\boldsymbol{r})\partial_l\psi_\beta(\boldsymbol{r}) - \hat{a}^\dagger_\beta\hat{a}_\alpha r_k\psi_\alpha(\boldsymbol{r})\partial_l\psi^*_\beta(\boldsymbol{r})\right) \, .\end{aligned} \tag{2.60}$$

Exchanging the index labels under the second term then yields

$$\begin{aligned}\hat{L}_j(t) &= \frac{-i\hbar}{2}\epsilon_{jkl}\sum_{\alpha,\beta}\hat{a}^\dagger_\alpha(t)\hat{a}_\beta(t)\int d^3r r_k\left(\psi^*_\alpha(\boldsymbol{r})\partial_l\psi_\beta(\boldsymbol{r}) - \psi_\beta(\boldsymbol{r})\partial_l\psi^*_\alpha(\boldsymbol{r})\right) = \\ &= m\int d^3r\left[\boldsymbol{r}\times\left(\frac{-i\hbar}{2m}\sum_{\alpha,\beta}\left(\psi^*_\alpha(\boldsymbol{r})\nabla\psi_\beta(\boldsymbol{r}) - \psi_\beta(\boldsymbol{r})\nabla\psi^*_\alpha(\boldsymbol{r})\right)\hat{a}^\dagger_\alpha(t)\hat{a}_\beta(t)\right)\right]_j \, .\end{aligned} \tag{2.61}$$

As shown in (2.51), the bracketed term just corresponds to the current density operator, and we can therefore conclude

$$\hat{L}_j(t) = m\int d^3r\left(\boldsymbol{r}\times\hat{j}(\boldsymbol{r},t)\right)_j \, . \tag{2.62}$$

Again, this expression can be Fourier transformed to get the energy dependent form. Here, we refer to this Fourier transform as the angular momentum energy density $\lambda(E)$, and it follows that

$$\hat{\lambda}_j(E) = m\int d^3r\left(\boldsymbol{r}\times\hat{j}(\boldsymbol{r},E)\right)_j \, . \tag{2.63}$$

2.3 Local Density of States

Local density of states is obtained by projecting the spectral function [18] onto a local basis of orbitals. It is a useful observable that enables us to probe the

occupation of certain local orbitals as function of energy. Suppose we have set of orbital indices M we want to project onto. We define local density of states on set M as [24]

$$\rho_M(E) = -\frac{1}{\pi} \sum_{j \in M} \mathrm{Im} G^R_{jj}(E) \,. \tag{2.64}$$

The relation of the local density of states to the transport problems can be illustrated by further inspection of relation (2.47). The trace in the integral for overall current can be further changed into

$$\begin{aligned} \mathrm{Tr}\left[\boldsymbol{\Gamma}_L \boldsymbol{G}^R \boldsymbol{\Gamma}_R \boldsymbol{G}^A\right] &= i\,\mathrm{Tr}\left[\left(E - \boldsymbol{H} - \boldsymbol{\Sigma}^A_L - (E - \boldsymbol{H} - \boldsymbol{\Sigma}^A_L)^\dagger\right) \boldsymbol{G}^R \boldsymbol{\Gamma}_R \boldsymbol{G}^A\right] = \\ &= i\,\mathrm{Tr}\left[\boldsymbol{G}^A \left((\boldsymbol{G}^A)^{-1} + \boldsymbol{\Sigma}^A_R - (\boldsymbol{G}^R)^{-1} - \boldsymbol{\Sigma}^R_R\right) \boldsymbol{G}^R \boldsymbol{\Gamma}_R\right] = \\ &= i\,\mathrm{Tr}\left[\left(\underbrace{\boldsymbol{G}^R - \boldsymbol{G}^A}_{2i\mathrm{Im}\boldsymbol{G}^R} + \boldsymbol{G}^A \left(\boldsymbol{\Sigma}^A_R - \boldsymbol{\Sigma}^R_R\right) \boldsymbol{G}^R\right) \boldsymbol{\Gamma}_R\right] \,. \end{aligned} \tag{2.65}$$

We can therefore see that the spectral function and by extension the local density of states is directly present in the formula for total current. The local projection then leads to additional information about current flowing through specified orbitals.

3. Computational Methodology

3.1 DFT for Extended Molecules

3.1.1 Kohn-Sham DFT

As a starting point to all calculations, we use the ab-initio density functional theory (DFT) [6]. DFT is a mean field theory, replacing the problem of exponentially growing Hilbert space for interacting particles with problem of finding self-consistent electron density n such that the total energy of the system is minimized. In the Kohn-Sham variant, we use certain basis of states to express electronic states as effective single particle states $|\phi_i>$[25]

$$|\phi_i>=\sum_n c_{in}|\beta_n>\,, \tag{3.1}$$

where $|\beta_n>$ is the basis state and c_{in} are the expansion coefficients. The electron density operator is then expressed as[25]

$$\hat{n}=\sum_{i\,\text{occupied}}|\phi_i><\phi_i|\,, \tag{3.2}$$

where the summation runs only over the occupied orbitals, i.e. for system containing N electrons, over the N least energetic orbitals (with different orbitals for different spins).

Typically, states are expressed as wavefunctions and the electron density as scalar field in position coordinates. The (effective) Kohn-Sham Hamiltonian then has form[25]

$$\hat{H}=\hat{T}+V_{\mathrm{I}}(\boldsymbol{r})+V_{\mathrm{H}}[\hat{n}(\boldsymbol{r})]+V_{\mathrm{xc}}[\hat{n}(\boldsymbol{r}),\nabla\hat{n}(\boldsymbol{r})]\,, \tag{3.3}$$

where $\hat{T}$ is the kinetic energy operator, V_{I} is the potential due to static background (most commonly created by presence of ions), V_{H} is the classical Coulomb repulsion of electrons, commonly denoted as Hartree term of electron interaction, and V_{xc} is the exchange-correlation potential, which accounts for the more complicated aspects of electron interaction. The last two potentials are functionals of the electron density, hence the name of this approach. Furthermore, exchange-correlation potential can also depend on the gradient of the electron density.

The exact exchange-correlation potential is unknown, but good approximate functionals are available. For most calculations in this work, we employ the pbe functional[26]. Besides the choice of functional, precision of the DFT calculation is mainly tuned by the choice of basis. Larger basis allows for a more complete expansion of the real many-body states and convergence of physical properties should be established with respect to the basis size. Here, we mostly use localised cartesian Gaussian orbital basis sets def2-SVP and def2-TZVP[27].

We use the DFT implementation by the TURBOMOLE[28] program and by the FHI-AIMS[29] program. We do not use the resolution of identity (RI) approximation[30] in TURBOMOLE.

3.1.2 Extended Molecule

In a typical molecular break junction setup [18, 1], molecule sits between two macroscopic electrodes. In order to describe the interaction with the electrodes correctly, one needs to describe correctly the bonding of the molecule to these electrodes, including the geometry and electronic density. Common approach is to include parts of the electrodes in the DFT calculation together with the molecule[3], forming the so called extended molecule. Then, at least a part of the molecule-electrode bonding is described accurately with the numerical methods. The electrode clusters themselves are coupled to reservoirs by a model self-energy, in this work we assume wide band approximation[20], described below.

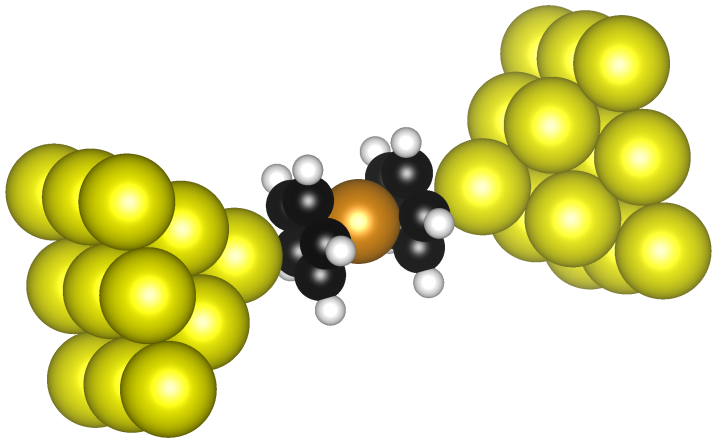

Figure 3.1: Molecule of ferrocene together with part of golden electrodes forms a so called extended molecule. Entire extended molecule needs to be treated at the ab-initio level to properly model the effect of molecule bonding to the electrodes.

The exact shape of the electrode clusters in the extended molecule however plays important role. For example, symmetrical clusters can incorporate symmetries which would not be present in realistic (infinite) electrodes. The last part of this work (see 4.3) illustrates the effects of the electrode size and shape.

3.2 Model Self Energy

As shown in 2, the transport observables are tied to values of Green's function, which relies on knowledge of self-energy. The self-energy is not known a priori and hence needs to be either calculated or approximated.

For systems where the electrodes are wire-like (effectively 1D), we are explicitly calculating the self-energy by iteratively projecting the effects of unit cells of the wire onto itself, as shown in Fig. 3.2 and implemented in TSaint code[22]. Part of the wire electrode is included in the extended molecule and the self-energy is included with it. In practice, this means that two calculations are necessary to calculate the conductance and other properties of the junction - the bulk calculation, where the self-energy is iteratively evaluated in the wire and device calculation, where the self-energy is added to the extended molecule and the transport observables are determined. This approach is used for the Geländer molecule ab-initio calculations.

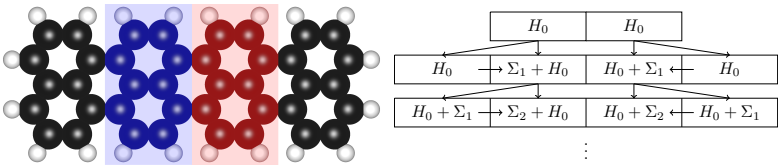

(a) Unit cell of the electrode wire and iterative self-energy determination

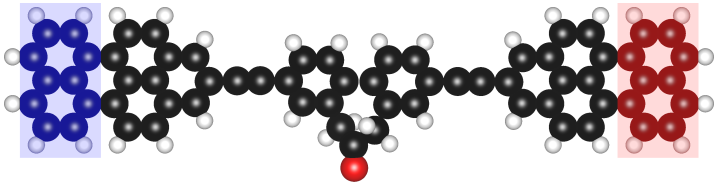

(b) Layers of electrodes in the extended molecule with self-energy

Figure 3.2: (a) : Illustration of the calculation of self-energy by iterative projections of influence of unit cells onto themselves. (b) : The layers of the electrodes included in the extended molecule with non-zero self-energy.

For a more general type of electrode (and for the other calculations presented in this work), an approximate form of the self-energy is used, as defined in [20] - the wide band approximation results in on-diagonal energy independent self-energy in the basis of local atomic orbitals, which can be expressed as

$$\hat{\Sigma}^A = \sum_{a \in A_E} |a\rangle\langle a|(\epsilon_a + i\eta_a)\,, \tag{3.4}$$

where A_E is the set of chosen atomic orbitals, ϵ_a is real energy shift caused by the reservoir and η_a is real and sets the absorbing/creating boundary conditions.

In order to emulate coupling to the infinite reservoir, only few layers of the electrode clusters from the extended molecule are chosen to accommodate the self-energy - only for those orbitals $|a\rangle$ the self-energy is non-zero. Such choice also allows us to separate the self-energy due to left and right reservoir, as need for formulas such as (2.47).

The model self-energy in this case contains set of free parameters ϵ_a and η_a. Parameter ϵ_a can be further constrained by balancing it such that the extended molecule is charge neutral. This leaves only η_a, which can be chosen to approximately model the band width of the reservoirs, but the dependence of the transport observables on η_a is usually trivial[20].

In either case, once the self-energy and Green's functions are determined, various transport observables can be determined, as shown previously in 2.

3.3 Electronic Structure in the *GW* Approximation

In context of ab-initio electronic structure, the *GW* approximation is often used [15] to refine a mean-field results (obtained for example from DFT) by including approximate electron interactions in a self-consistent way. *GW* approximations

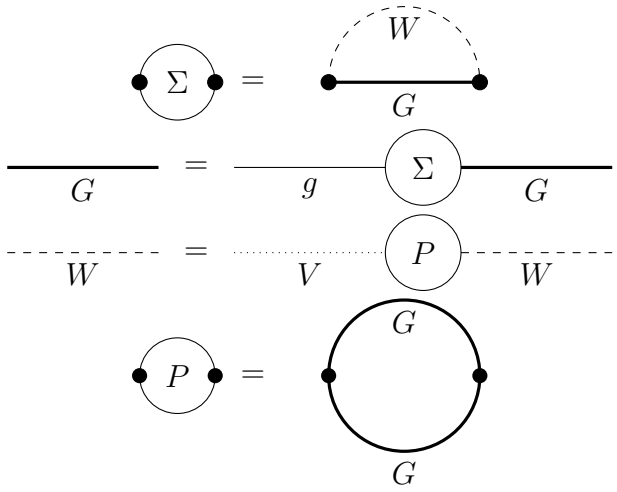

Figure 3.3: Self-consistent set of Feynman diagrams for the GW approximation. The vertex corrections would be present in the term for the self-energy of electrons (Σ) and bosons (P). By neglecting them, we are left with two Dyson equations for electrons and bosons and two self-energy equations.

simplifies the form of the interaction self-energy derived from the Hedin equations [14]. Specifically, the vertex corrections due to electron interaction are neglected, leaving the self energy in a form of product of Green's function and the screened potential W, hence the name of the approximation. See Fig. 3.3 for representation of Hedin equations as Feynman diagrams[18].

Compared to DFT, GW promises to include parts of the electron correlation that are not present in the typical DFT calculations. Specifically, DFT is known to introduce significant errors in the estimation of LUMO-HOMO gaps [3]. The GW approximation describes the excited state of the system more accurately, leading to a better estimation of the gap.

The self-consistent solution to the Hedin equations requires a start solution that is iterated until a stationary solution is found. Furthermore, many flavours of GW are commonly used [15] which reduce the full self-consistency to only partial self-consistency.

In our approach, we take the DFT solution to the many-body problem as starting point for the GW calculation and only require self-consistency in the eigenvalues of the effective Hamiltonian constructed from the Green's function. This so called evGW is implemented in the TURBOMOLE package as well [31].

3.4 Graphical Tools

The 3D models of the molecules/cluster were made using the VESTA[32] software, the figures were made using python interface to matplotlib[33]. Many of the scripts used for data visualisation are made available in python package compphysutils[34].

4. Results and Discussion

4.1 Molecular Conductance of Ferrocene

As stated before, we initially investigated the effect of rotation of cyclopentadiene rings in ferrocene on the conductance (see Fig. 4.1 for extremes of the ring rotations and Fig. 1.1b for sketch of rotation). The effect for bare ferrocene in the junction proved to be negligible, as will be illustrated later. In order to understand this observation together with the experimental results [5], we investigated the electronic structure of bare ferrocene in the junction. The transport seems to occur resonantly through the analogue of isolated lowest unoccupied molecular orbital (LUMO) of gas phase ferrocene.

We summarize the results for the ferrocene calculations in the sections below. Unless otherwise stated, we study the transport at the DFT level, with basis set def2-TZVP[27], pbe functional[26] and DFT-D4 dispersion correction[7]. We chose the model on-diagonal energy independent self-energy as described in 3 with constant parameter $\eta = 0.1$ H.

4.1.1 Ferrocene - Geometry and Electronic Structure

The ferrocene molecule consists of two cyclopentadiene rings parallel to each other surrounding an iron ion. The unpaired electrons on the cyclopentadienes are shared through the iron, creating a conjugate system. Depending on the relative rotation of the (cyclopentadiene) rings, ferrocene can exist on a spectrum from eclipsed to staggered geometry, as shown in Fig. 4.1. In gas phase, the eclipsed geometry is reported to have minimum energy[35].

The frontier molecular orbitals of ferrocene are shown in Fig. 4.2, as calculated in the TURBOMOLE[28] suite with the aforementioned parameters. The geometry of the molecule has been optimized so that the elements of gradient of total energy with respect to ion coordinates is less than 0.001 a.u. Note the shape of these orbitals for the following sections, were the ferrocene molecule is placed in the junction.

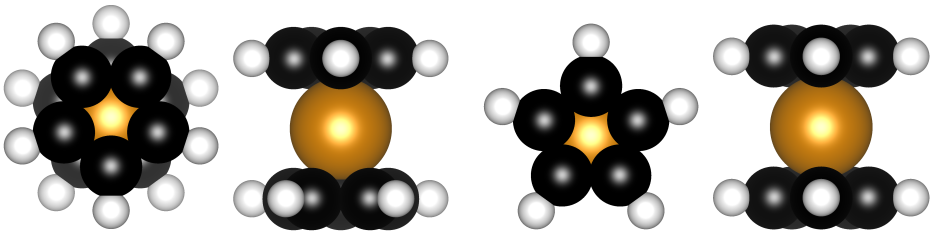

(a) The staggered geometry (b) The eclipsed geometry

Figure 4.1: Two geometries of the ferrocene molecule - staggered and eclipsed, named after the relative rotation of the cyclopentadiene rings surrounding the iron ion.

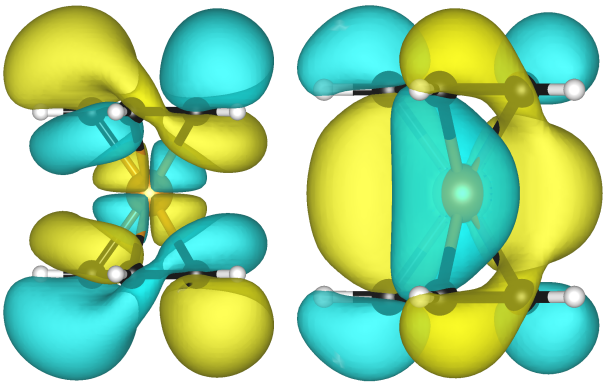

(a) LUMO of eclipsed ferrocene

(b) HOMO of eclipsed ferrocene

Figure 4.2: The LUMO (lowest unoccupied molecular orbital) and HOMO (highest occupied molecular orbital) of molecular ferrocene. Plotted are the isosurfaces of the Kohn-Sham wavefunctions at absolute value 0.01. Blue colour indicates negative values, yellow indicates positive values. Both of these orbitals show strong electron presence on the iron ion which binds the two rings together. The LUMO orbital features a distinguishable two-fold rotational symmetry around the iron ion, and resembles a *d*-type orbital at the iron site.

4.1.2 Junction Formation - Optimal Distance and Energy

The experimental setup[5] uses pure ferrocene (without linker groups) to bind to two gold electrodes in a mechanical-break junction setup. The exact tip-to-tip distance of the electrodes is not experimentally accessible, so in order to determine possible modes of transport, number of different distances need to be investigated.

We initially tried to determine the optimal electrode distance by minimising the energy vs. electrode distance curve. But, since the breaking of the junction is not an equilibrium process[3], the point of minimum energy does not necessarily correspond to the most probable state of the system. Therefore, we considered also the symmetry of the junction - for molecule significantly tilted/moved towards a single electrode, we decreased the distance in order to form a symmetric junction.

We studied two distinct geometries, which we called the parallel and perpendicular geometry. For the parallel geometry (see Fig. 4.3a), the ferrocene molecule is stable at the symmetric position in the middle of the junction for wide range of electrode distances, and therefore we decided to minimize the energy to choose the optimum distance of 4.1 Å from central iron ion to the apex atom of the electrode on either side.

For the perpendicular geometry (see Fig. 4.3b), the ferrocene molecule tilts and moves towards one electrode for all distances above 2.7 Å. In order to determine the conductance and other properties of the junction, we used distance 2.6 Å from central iron ion to the apex atom of electrode. For details about energy of the given geometries, see A.2

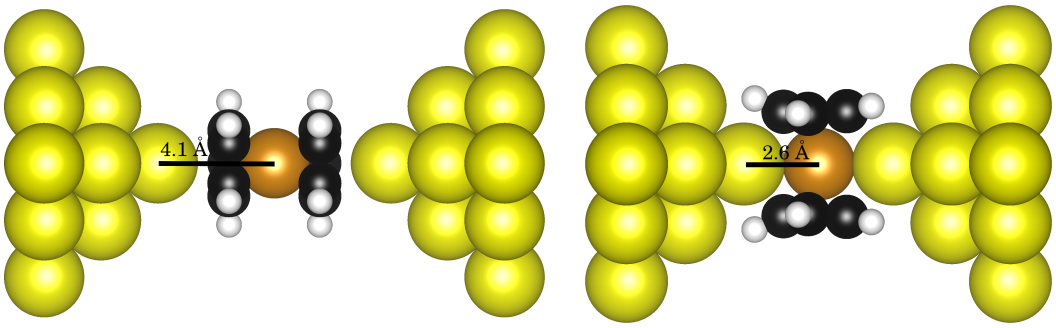

(a) The parallel geometry. (b) The perpendicular geometry.

Figure 4.3: The junction geometries of the ferrocene. For perpendicular geometry to form a symmetrical junction, the molecule has to be somewhat deformed by the closeness to gold electrodes.

4.1.3 Conducting LUMO Channel through the Iron Ion

Firstly, we were interested in the influence of relative rotation of the rings on the overall conductance of the junction. While in [4], the rotation of the rings is associated with significant changes in conductance, no such change was observed in our calculations, as shown in Fig. 4.4. We believe the cause of the interference observed in [4] is the interaction of ferrocene with the system of phenyl linkers - the ferrocene moves in the junction as the rings rotate, while in our case ring rotation does not change the orientation of the ferrocene in the nanogap.

With this knowledge, further results are only presented for initially eclipsed geometry. Then, the positions of the atoms contained in ferrocene molecule are optimised so that the gradient of total energy with respect to atomic coordinates of ferrocene has components of magnitude less than 0.001 a.u.

In order to account for possible amorphous structure of the electrodes (measurements in [5] happen at room temperature), we added ad-atoms to break the crystalline symmetry. We also checked that our basis set is of sufficient size. These results are summarized for both geometries in Fig. 4.5. We should note that while we used TURBOMOLE for the parallel geometry, calculations for the perpendicular geometry were done using the FHI-AIMS[36] package with Van der Waals correction due to problems with convergence in the TURBOMOLE suite. We used the default tight basis in FHI-AIMS.

For the neighbourhood of the Fermi energy, it is clear that the junction in the perpendicular geometry is more conducting, as the nearby resonant peak increases the current flowing through the junction. This peak corresponds to the LUMO molecular state, and its wavefunction on the extended molecule is shown in Fig. 4.6.

This orbital has been identified by masking the contributions to transmission function from other orbitals. Explicitly, in the determination of the trace that leads to transmission function as in (2.47), we add an extra multiplication by masking matrix M_{ij}, where the elements of M_{ij} are 1 if either i or j are in a set of chosen indices and zero otherwise.

We refer the reader to [37] to compare the results for parallel calculation with similar calculation using silver electrodes. Clearly, the transport in the parallel geometry is also resistant to electrode changes and hence we postulate that it

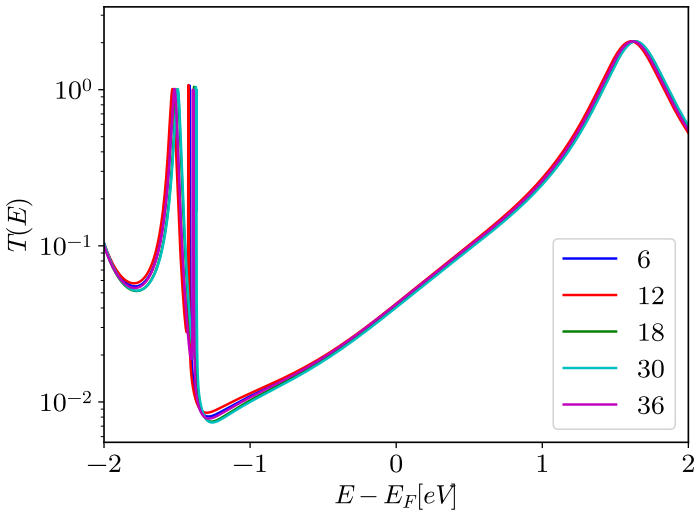

Figure 4.4: Transmission of the ferrocene molecular junction in the parallel geometry for multiple relative angles of the cyclopentadiene rings. No significant deviations from the mean transmission is observed. The labels of the curves correspond to relative rotation of the rings from the eclipsed position in degrees (36 degrees corresponds to exactly staggered position).

reflects the transport through molecular orbitals as well. The resonant orbital is identified and visualised in Fig. 4.7.

In both geometries, the transport state is significantly associated with the iron *d*-state which is present in the LUMO orbital. To further show the role of iron, we plotted the local density of states on the iron orbitals of the molecule, shown in Fig. 4.8. Hence, we conclude that the transport through the iron orbital is more defining for the junction properties in this setup than the relative rotation of the ferrocene rings.

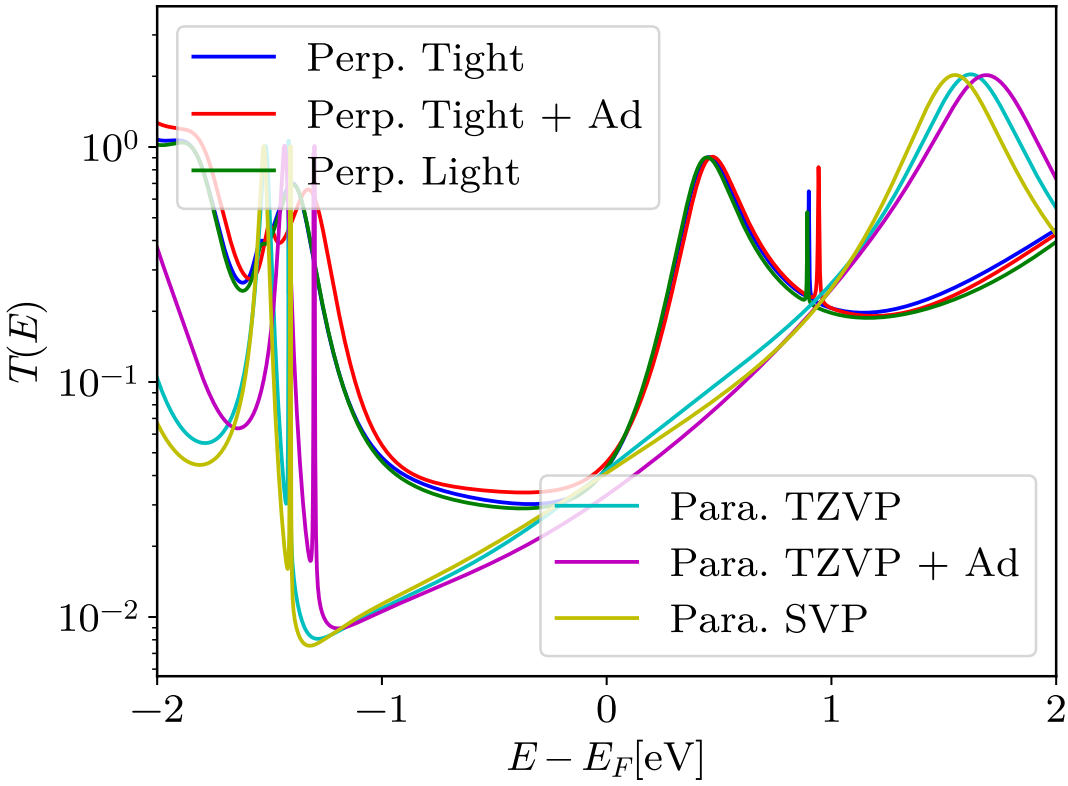

Figure 4.5: Robustness of transmission function with respect to geometry perturbations of the electrodes is demonstrated by the inclusion of ad-atoms to the electrode structure. These do not change the overall shape of the transmission function. Furthermore, we showcase that decreasing the basis set size does not change the overall transmission function shape, signalling that our basis set is of sufficient size.

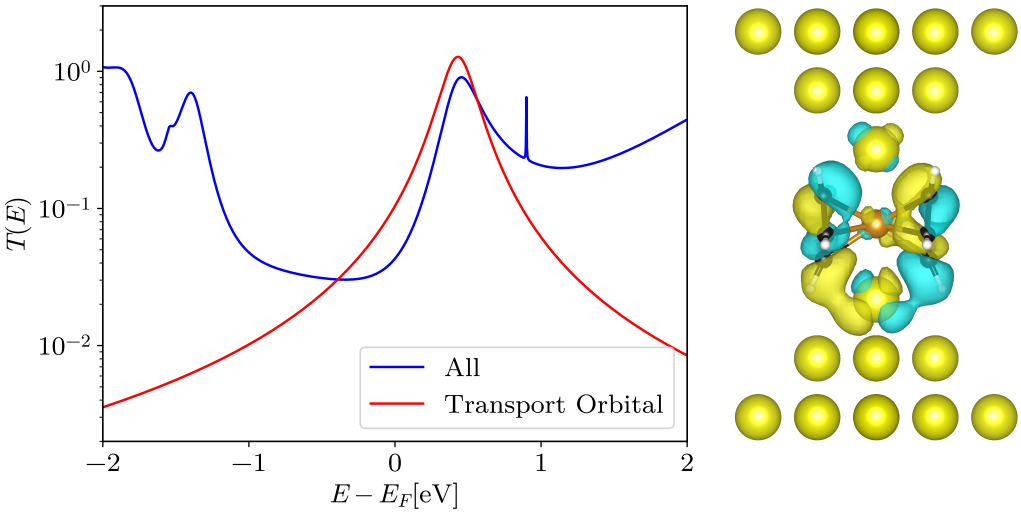

(a) Transmission function of transport orbital.

(b) Transport orbital wavefunction.

Figure 4.6: The decomposition of the transmission function into the dominant transport state for perpendicular junction geometry. Since the single state transmission function is at certain energy points larger than the total transmission function, there are some small interference effects present in the overall transmission function. The state resembles the molecular LUMO state of the ferrocene. The plotted isosurfaces are given at value 0.01, with yellow surfaces representing positive values and blue surfaces representing negative values.

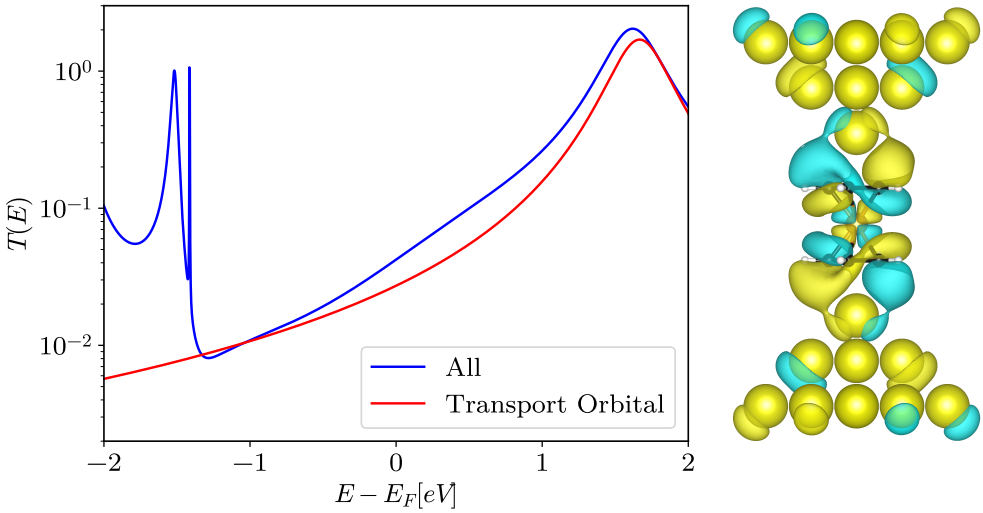

(a) Transmission function of transport orbital.

(b) Transport orbital wavefunction.

Figure 4.7: The decomposition of the transmission function into the dominant transport state. The geometry of the junction is parallel. The state resembles the molecular LUMO state of the ferrocene. The plotted isosurfaces are given at value 0.01, with yellow surfaces representing positive values and blue surfaces representing negative values.

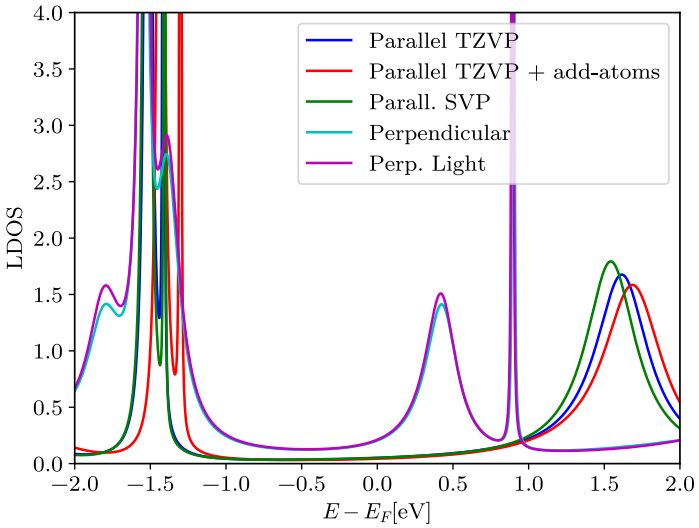

Figure 4.8: The local density of states (LDOS) projected onto the iron orbitals in the ferrocene molecule. The LDOS reflects the profile of overall transmission in the states closest to the Fermi energy, and positions of others states correspond with peaks in transmission function as well, although the relative magnitude of the peaks differs.

4.2 Helical Orbitals and Ring Currents

Next topic explored in our work is motivated by scanning tunnelling microscopy experiments described in [13]. In these experiments, a Geländer molecule (see Fig. 4.9) was observed rotating in a direction irrespective of the bias applied to the junction. Due to the counter-intuitive nature of this observation, we decided to investigate the system first from first principles and then to rationalize the results using a simple toy model of the system, inspired by model discussed in [11].

An overarching idea for the source of molecule rotation in our approach is momentum transfer from the electronic current to the molecule. We postulate that given a molecular current with non-zero angular momentum, the molecule acquires angular momentum in the opposite direction. This simplistic viewpoint does not explore the dynamics of the molecular rotation, and therefore should be taken as a qualitative exploration of the sources of the rotation. Nevertheless, we derive conditions for the correct bias (in)dependence of the current induced molecular rotation.

4.2.1 Ab-Initio Calculations

In order to determine the angular momentum, we follow the formulas derived in 2.2.1, specifically (2.63). For ab-initio calculations, we use the TURBOMOLE [28] program to get the effective Hamiltonian, which is then used in the TSaint[22] program to determine the current density as function of energy. The molecule model is shown in Fig. 4.9. The electrodes used in ab-initio calculations are nanoribbons of graphene, as the TSaint code is optimised to work with such electrodes.

The bulk calculation is done on a graphene nanoribbon supercell. The result of the bulk calculation is the self-energy on central two cells due to presence of surrounding nanoribbon cells, as described in [22] and previously in 3. The self-energy is determined in iterations, which effectively elongates the nanoribbon. The convergence checks for the number of iterations of self-energy calculations, basis set size and more are included in A.3.

The consequent device calculation uses the self-energy determined in bulk calculation to induce current across the molecular junction and to determine the associated current density. We integrate the current density to determine the angular momentum density in energy space. The actual angular momentum at given bias is determined by integrating the angular momentum density with difference of occupations between left and right electrode, as dictated by formulas (2.57) and (2.63).

4.2.2 Helical Orbitals and Currents in Ab-Initio

For orbitals near Fermi energy, one observes the helical structure around the triple bonds that connect the molecule to the graphene nanoribbons, as shown in Fig. 4.10

The helical orbitals are associated with circular ring currents along the triple bond, as discussed in [10]. The angular momentum of these ring currents switches around the Fermi energy, as shown in Fig. 4.11

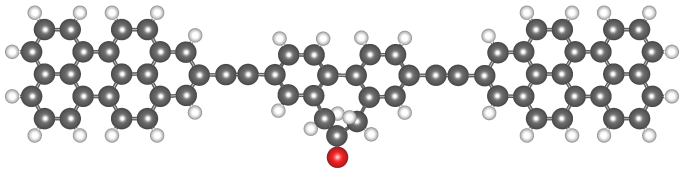

(a) Molecule with electrodes

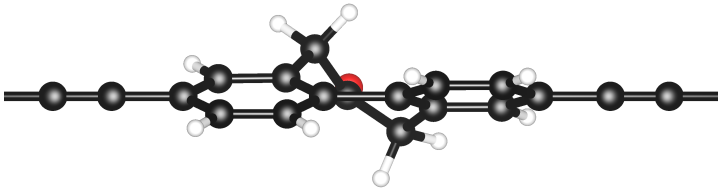

(b) Detail of the central region

Figure 4.9: The molecule consists of two benzene rings which are forced into relative rotation by a linker group (see detail (b)). The molecule is connected to electrodes by triple bonds of carbon. The electrodes in ab-initio calculations are taken as 2D graphene slices.

Consider now the following - the angular momentum acquired by the electrons through transport is given by integrating the angular momentum energy density (see (2.63)) in the transport window (see Fig. 4.11 for visualisation)

$$L_z = \int_{-\infty}^{\infty} dE\lambda_z(E)(f_L(E;\mu_0 - eV) - f_R(E;\mu_0)) \approx \int_{\mu_0}^{\mu_0 - eV} dE\lambda_z(E)\,, \qquad (4.1)$$

where μ_0 is the equilibrium chemical potential of both electrodes and V is the applied bias.

For negative bias the integral probes the energies above the Fermi energy, while for positive bias, the integral runs over energies below Fermi energy and introduces an extra minus sign. Therefore, if the angular momentum energy density for the states below Fermi energy is opposite to angular momentum energy density of states above the Fermi energy, the observed angular momentum remains the same, irrespective of the bias direction.

This is the basic postulate by which we explain the experimental observation of molecule rotating in a directed way. Furthermore, in the next few sections, we try to explore what gives rise to this asymmetry of the angular momentum energy density.

We also provide more explicit view of the changing current circulation in Fig. 4.12.

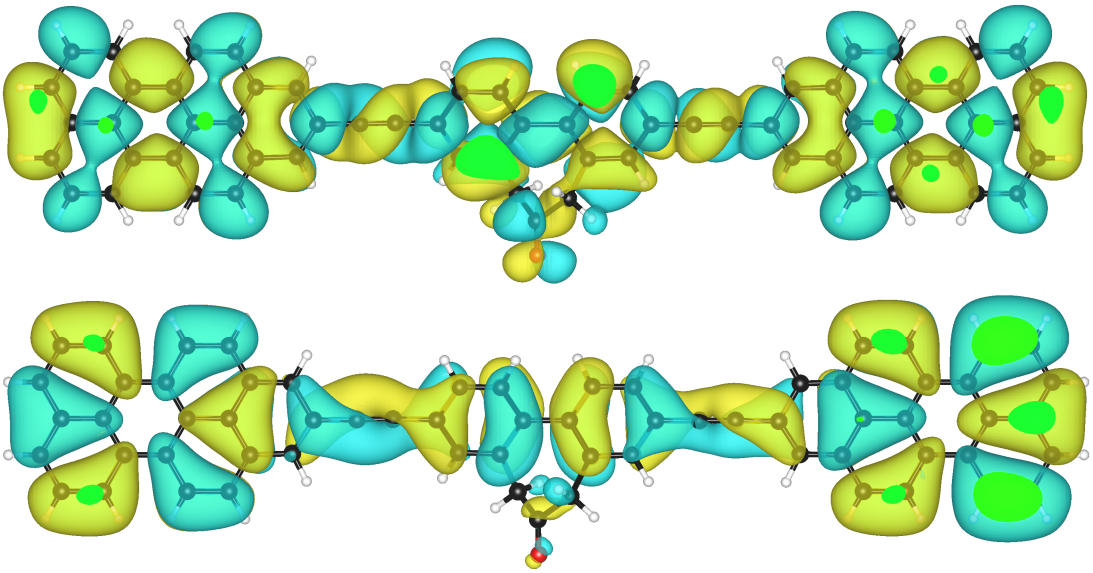

Figure 4.10: The helical orbitals present along the triple bonds in the Geländer molecule. The top orbital has energy above Fermi energy of the system, the bottom one has energy below it. The sense of rotation of the helicities is different for the two orbitals and same for both sides at the same orbital. The isosurface level is chosen to be 0.005, yellow implies positive values, blue negative values.

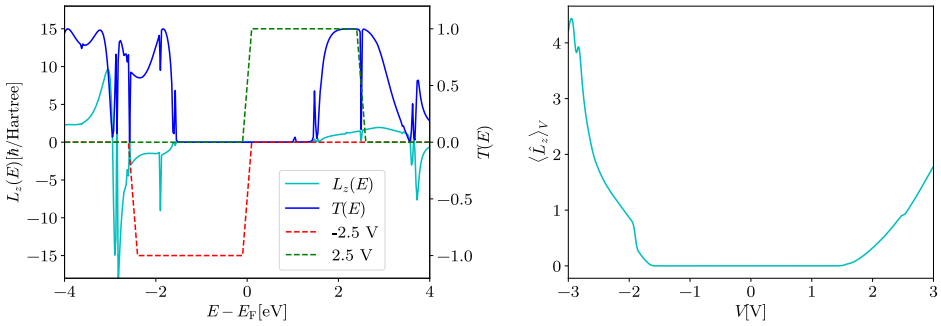

(a) Momentum energy density and transmission function

(b) Momentum at given bias

Figure 4.11: Angular momentum density $\lambda_z(E)$ along the easy axis of the molecular junction is shown in (a). The asymmetry around the Fermi energy means that the angular momentum for both positive and negative bias has the same direction, as shown in (b), where $\lambda_z(E)$ is integrated in the transport window.

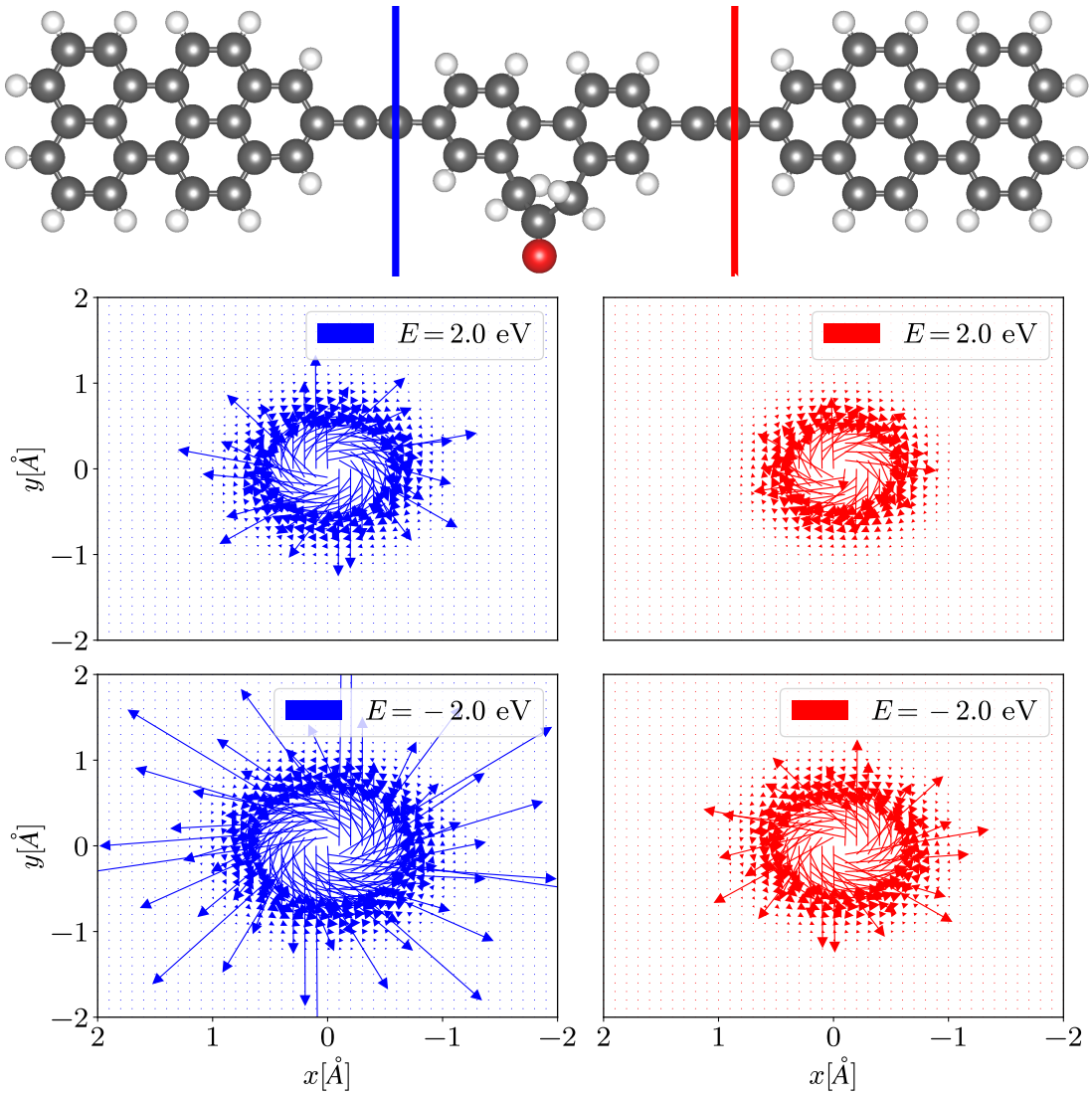

Figure 4.12: A cross-section of the Geländer molecule showing the current density profile around the carbon atoms forming the triple bond. The generated current is the same for both cross-sections for a given energy, and switches direction for opposite energies. Energies are given with respect to the equilibrium Fermi energy of the system.

4.2.3 Toy Model for Helical Orbitals and Currents

The triple bonds are the drivers of the angular momentum generation and are known to have helical orbitals with switching helicities, so we will try to replicate and extend the results of some previous works [11, 10] to discover what lies at the core of this switching behaviour. We shall define a toy model describing a triple bond conjugated system in a Hückel-like Hamiltonian[25]. We consider a chain of carbon atoms of length N, each with 2 perpendicular p-type orbitals, pointing in direction also perpendicular to the axis of the system. In general, the pairs of p-type orbitals could be rotated by an arbitrary angle, but this rotation can be removed by unitary transformation (see A.5). Hence, without loss of generality, we can assume that the orbital pairs are aligned, as shown in Fig. 4.13, with Hamiltonian

$$\boldsymbol{H} = -t \begin{pmatrix} \mathbf{0} & \boldsymbol{I} & \mathbf{0} & \mathbf{0} & \dots \\ \boldsymbol{I} & \mathbf{0} & \boldsymbol{I} & \mathbf{0} & \dots \\ \mathbf{0} & \boldsymbol{I} & \mathbf{0} & \boldsymbol{I} & \dots \\ \vdots & \vdots & \vdots & \vdots & \dots \\ \dots & \mathbf{0} & \mathbf{0} & \boldsymbol{I} & \mathbf{0} \end{pmatrix} , \tag{4.2}$$

where $\boldsymbol{I}$ is the 2x2 identity matrix and $t > 0$ determines the energy scale.

The Hamiltonian follows from the overlaps of p orbitals restricted to nearest neighbour elements, for which

$$\langle p_\beta | p_\gamma \rangle = \cos(\gamma - \beta) e^{-ad^2/2} , \tag{4.3}$$

where

$$\langle \boldsymbol{x} | p_\beta \rangle = N\rho \cos(\phi - \beta) e^{-a(\rho^2 + z^2)} \tag{4.4}$$

is the wavefunction of the p-orbital in the cylindrical polar coordinates (ρ, ϕ, z) with z axis coinciding with the axis of the chain and a is inverse distance parameter - product ad^2 together sets the effective distance of the p-orbitals. From this form of the overlap matrix, one can deduce that for $\beta, \gamma \in \{0, \frac{\pi}{2}\}$, orbitals along initial direction, say x, only couple to other orbitals along the x direction.

We exchange the overlap parameter for generic energy parameter t, but otherwise, we retain the same matrix structure to construct the Hamiltonian matrix.

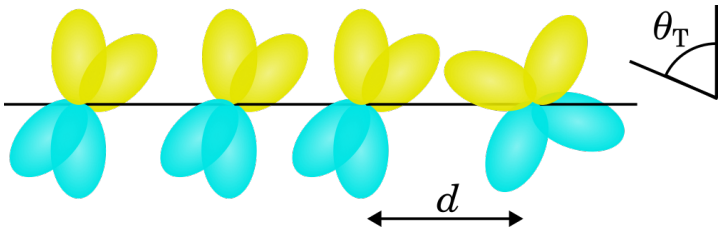

Figure 4.13: The illustration of orbitals present in the toy model. The N carbon atoms form a linear chain with equal distance d between sites. At each site, pair of p-orbitals is present. At the end of the chain, a perturbation is introduced which effectively rotates the orbital pair by twist angle θ_T.

In order to create helical orbitals, one must couple the x and y sectors (sectors with p-orbital angles β, γ taking values 0 and $\pi/2$, respectively) orbitals to each other. The analytical solution presented in [11] used a lone rotated p-orbital to couple the two "strands" of orbitals to each other. Here, we slightly generalize this approach by introducing an energy penalty for one strand of orbitals in the original Hamiltonian, i.e. we define perturbation $\boldsymbol{V}$

$$\boldsymbol{V} = \begin{pmatrix} \boldsymbol{\epsilon} & \mathbf{0} & \mathbf{0} & \mathbf{0} & \dots \\ \mathbf{0} & \mathbf{0} & \mathbf{0} & \mathbf{0} & \dots \\ \vdots & \vdots & \vdots & \vdots & \ddots \\ \dots & \mathbf{0} & \mathbf{0} & \mathbf{0} & \boldsymbol{R}(\theta_{\mathrm{T}})\boldsymbol{\epsilon}\boldsymbol{R}(\theta_{\mathrm{T}})^{\dagger} \end{pmatrix} , \tag{4.5}$$

where

$$\boldsymbol{\epsilon} = \begin{pmatrix} 0 & 0 \\ 0 & \epsilon \end{pmatrix} , \tag{4.6}$$

where $\epsilon > 0$ is the energy penalty and θ_{T} is the twist angle of the last pair of bases - the energy penalty is split between the two basis states as if the basis was rotated by θ_{T}. Our next goal is to determine how this coupling matrix brings forth the helicity in the orbitals. We will employ the degenerate perturbation theory to this goal [38, 39].

4.2.4 Helicity via Perturbation Theory

Before we embark onto the journey of perturbation theory, we define the helicity more rigorously. Since the Hamiltonian in (4.2) is real, eigenstates can be in general chosen real as well. In order to represent the helicity, one can represent the eigenstates projected onto single carbon sites as vector in real space with components along the two perpendicular p-orbital directions [11]. The helicity can then be defined as measure of misalignment of consecutive vectors. Such measure is provided by vector product in three dimensions.

More rigorously, we define the local polarisation vector $\boldsymbol{P}_{k,\psi}$ of state $|\psi\rangle$ at site k as

$$\boldsymbol{P}_k = \begin{pmatrix} \langle p_{k,x}|\psi\rangle \\ \langle p_{k,y}|\psi\rangle \end{pmatrix} \tag{4.7}$$

and the helicity at site k as

$$h_{k,\psi} = \boldsymbol{P}_{k,\psi} \times \boldsymbol{P}_{k+1,\psi} = \left(\langle p_{k,x}|\psi\rangle\langle p_{k+1,y}|\psi\rangle - \langle p_{k,y}|\psi\rangle\langle p_{k+1,x}|\psi\rangle\right) . \tag{4.8}$$

Since the eigenvectors can be chosen real, we can symmetrize the expression to get

$$h_{k,\psi} = \frac{1}{2}\left(\langle\psi|p_{k+1,y}\rangle\langle p_{k,x}|\psi\rangle + \langle\psi|p_{k,x}\rangle\langle p_{k+1,y}|\psi\rangle - \right. \tag{4.9}$$

$$\left. \langle\psi|p_{k,y}\rangle\langle p_{k+1,x}|\psi\rangle - \langle\psi|p_{k+1,x}\rangle\langle p_{k,y}|\psi\rangle\right) , \tag{4.10}$$

which leads us to a definition of total helicity operator

$$\hat{h} = \frac{1}{2}\sum_{k=1}^{N-1} |p_{k,x}\rangle\langle p_{k+1,y}| - |p_{k,y}\rangle\langle p_{k+1,x}| + \mathrm{h.c.} , \tag{4.11}$$

where h.c. stands for Hermitian conjugate of the previous two terms.

The matrix structure of such operator is also very simple

$$\boldsymbol{h} = \frac{1}{2}\begin{pmatrix} \mathbf{0} & \boldsymbol{R}\left(-\frac{\pi}{2}\right) & \mathbf{0} & ... \\ \boldsymbol{R}\left(\frac{\pi}{2}\right) & \mathbf{0} & \boldsymbol{R}\left(-\frac{\pi}{2}\right) & ... \\ \mathbf{0} & \boldsymbol{R}\left(\frac{\pi}{2}\right) & \mathbf{0} & ... \\ \vdots & \vdots & \vdots & \ddots \\ ... & \mathbf{0} & \boldsymbol{R}\left(\frac{\pi}{2}\right) & \mathbf{0} \end{pmatrix} . \tag{4.12}$$

We can test our helicity operator by inquiring its expectation value for simple rotated state

$$|\psi\rangle = \begin{pmatrix} \frac{1}{\sqrt{2}} \\ 0 \\ \frac{\cos\gamma}{\sqrt{2}} \\ \frac{\sin\gamma}{\sqrt{2}} \\ 0 \\ 0 \\ \vdots \end{pmatrix} . \tag{4.13}$$

We find that

$$\langle\psi|\hat{h}|\psi\rangle = \frac{1}{2}\sin\gamma\,, \tag{4.14}$$

which is a good measure of the polarisation vector rotation. The $\frac{1}{2}$ factor occurs due to product of magnitudes of polarisation vectors at site 1 and site 2.

We should also note that while we are in the end interested in the angular momentum, orbital helicity is a good proxy for the presence of non-zero net orbital angular momentum, because the two operators commute in our model. The angular momentum operator along the axis of the site chain is defined in position representation as[38]

$$\hat{L} = -i\hbar\frac{\partial}{\partial\phi} \tag{4.15}$$

Resolving this operator in the basis states written in (4.4) leads to matrix (neglecting the matrix elements proportional to intersite overlaps)

$$\boldsymbol{L} = \hbar\begin{pmatrix} \boldsymbol{\sigma}_2 & \mathbf{0} & \mathbf{0} & \dots \\ \mathbf{0} & \boldsymbol{\sigma}_2 & \mathbf{0} & \dots \\ \vdots & \vdots & \vdots & \ddots \\ \dots & \mathbf{0} & \mathbf{0} & \boldsymbol{\sigma}_2 \end{pmatrix} , \tag{4.16}$$

where

$$\boldsymbol{\sigma}_2 = \begin{pmatrix} 0 & -i \\ i & 0 \end{pmatrix} \tag{4.17}$$

is the second Pauli matrix. The commutator with the helicity operator matrix is then

$$[\boldsymbol{L},\boldsymbol{h}] = \boldsymbol{L}\boldsymbol{h} - \boldsymbol{h}\boldsymbol{L} = \frac{\hbar}{2}\begin{pmatrix} \mathbf{0} & \boldsymbol{\sigma}_2 i\boldsymbol{\sigma}_2 & \mathbf{0} & \mathbf{0} & \dots \\ \boldsymbol{\sigma}_2(-i)\boldsymbol{\sigma}_2 & \mathbf{0} & \boldsymbol{\sigma}_2 i\boldsymbol{\sigma}_2 & \dots & \\ \vdots & \vdots & \vdots & \ddots & \\ \dots & \mathbf{0} & \boldsymbol{\sigma}_2(-i)\boldsymbol{\sigma}_2 & \mathbf{0} & \end{pmatrix} - \tag{4.18}$$

$$-\frac{\hbar}{2}\begin{pmatrix} \mathbf{0} & i\boldsymbol{\sigma}_2\boldsymbol{\sigma}_2 & 0 & \dots \\ (-i)\boldsymbol{\sigma}_2\boldsymbol{\sigma}_2 & 0 & i\boldsymbol{\sigma}_2\boldsymbol{\sigma}_2 & \dots \\ \vdots & \vdots & \vdots & \ddots \\ \dots & \mathbf{0} & (-i)\boldsymbol{\sigma}_2\boldsymbol{\sigma}_2 & \mathbf{0} \end{pmatrix} = 0\,, \tag{4.19}$$

where we used the fact that $\boldsymbol{R}(\pm\pi/2) = \mp i\boldsymbol{\sigma}_2$.

With this definition of helicity operator as a proxy to angular momentum operator, we can move to the perturbation theory. Without the perturbation $\boldsymbol{V}$, the eigenvectors of $\boldsymbol{H}$ can be determined exactly [11] and take the following form

$$|\phi^0_{n,\alpha}\rangle = Z\begin{pmatrix} \sin\left(\frac{n\pi}{N+1}\right)\boldsymbol{v}_\alpha \\ \sin\left(\frac{2n\pi}{N+1}\right)\boldsymbol{v}_\alpha \\ \vdots \\ \sin\left(\frac{Nn\pi}{N+1}\right)\boldsymbol{v}_\alpha \end{pmatrix}\,, \tag{4.20}$$

where $\boldsymbol{v}_\alpha$ is a polarisation vector that remains constant through the entire chain, n is a quantum number and Z is the normalisation constant (see A.4 for details)

$$Z = \sqrt{\frac{2}{N+1}}\,. \tag{4.21}$$

We can determine the eigenvalue of such eigenvector by application of the Hamiltonian

$$\hat{H}|\phi^0_{n,\alpha}\rangle = (-t)\begin{pmatrix} \mathbf{0} & \boldsymbol{I} & \mathbf{0} & \mathbf{0} & \dots \\ \boldsymbol{I} & \mathbf{0} & \boldsymbol{I} & \mathbf{0} & \dots \\ \mathbf{0} & \boldsymbol{I} & \mathbf{0} & \boldsymbol{I} & \dots \\ \vdots & \vdots & \vdots & \vdots & \ddots \\ \dots & \mathbf{0} & \mathbf{0} & \boldsymbol{I} & \mathbf{0} \end{pmatrix}\begin{pmatrix} \sin\left(\frac{n\pi}{N+1}\right)\boldsymbol{v}_\alpha \\ \sin\left(\frac{2n\pi}{N+1}\right)\boldsymbol{v}_\alpha \\ \vdots \\ \sin\left(\frac{Nn\pi}{N+1}\right)\boldsymbol{v}_\alpha \end{pmatrix} = \tag{4.22}$$

$$= (-t)\begin{pmatrix} \sin\left(\frac{2n\pi}{N+1}\right)\boldsymbol{v}_\alpha \\ \vdots \\ \left[\sin\left(\frac{(k-1)n\pi}{N+1}\right) + \sin\left(\frac{(k+1)n\pi}{N+1}\right)\right]\boldsymbol{v}_\alpha \\ \vdots \\ \sin\left(\frac{(N-1)n\pi}{N+1}\right)\boldsymbol{v}_\alpha \end{pmatrix} = -2t\cos\left(\frac{n\pi}{N+1}\right)|\phi^0_{n,\alpha}\rangle\,, \tag{4.23}$$

where we used

$$\sin\left(\frac{Nn\pi}{N+1}\right) = \sin\left(\frac{(N+1-1)n\pi}{N+1}\right) = -\sin\left(\frac{n\pi}{N+1}\right)\cos(n\pi) = \tag{4.24}$$

$$= (-1)^{n+1}\sin\left(\frac{n\pi}{N+1}\right)\,, \tag{4.25}$$

and similarly

$$\cos\left(\frac{Nn\pi}{N+1}\right) = (-1)^n \cos\left(\frac{n\pi}{N+1}\right) . \tag{4.26}$$

Hence, the eigenvalues are given as

$$E_n^0 = -2t\cos\left(\frac{n\pi}{N+1}\right) . \tag{4.27}$$

The quantum number n clearly takes integer values from 1 to N. It is clear that the spectrum of the Hamiltonian is double degenerate - we can always choose at least two perpendicular polarisation vectors $\boldsymbol{v}_{\alpha/\beta}$, which will have the same energy. In order to get the first order corrections to the eigenstates due to the perturbation $\boldsymbol{V}$, and hence the first order corrections to the expectation value of helicity, we need to find a suitable polarisation basis that diagonalizes elements of $\boldsymbol{V}$ in the polarisation vector subspace. To that end, we determine the matrix elements of the $\boldsymbol{V}$ matrix in an arbitrary basis and solve the eigenvalue problem, as the eigenvectors of the matrix restricted to the polarisation vector subspace can be used to diagonalize it.

We choose $\boldsymbol{v}_x^\dagger = \begin{pmatrix}1 & 0\end{pmatrix}$ and $\boldsymbol{v}_y^\dagger = \begin{pmatrix}0 & 1\end{pmatrix}$ as our initial guess polarisation basis, which leads to matrix elements of type (for $\xi, \xi' \in \{x, y\}$, see A.6, here element at first row and second column corresponds to $\langle\phi_{n,x}^0|\hat{V}|\phi_{n,y}^0\rangle$ etc.)

$$\langle\phi_{n,\xi}^0|\hat{V}'|\phi_{n,\xi'}^0\rangle = \epsilon Z^2 \sin^2\left(\frac{n\pi}{N+1}\right)\begin{pmatrix}\sin^2(\theta_\mathrm{T}) & -\sin(\theta_\mathrm{T})\cos(\theta_\mathrm{T}) \\ -\sin(\theta_\mathrm{T})\cos(\theta_\mathrm{T}) & 1+\cos^2(\theta_\mathrm{T})\end{pmatrix} , \tag{4.28}$$

The eigenvalues of this matrix are

$$E_{n\alpha} = 2\epsilon Z^2 \sin^2\left(\frac{n\pi}{N+1}\right)\cos^2\left(\frac{\theta_\mathrm{T}}{2}\right) \tag{4.29}$$

$$E_{n\beta} = 2\epsilon Z^2 \sin^2\left(\frac{n\pi}{N+1}\right)\sin^2\left(\frac{\theta_\mathrm{T}}{2}\right) \tag{4.30}$$

with associated eigenvectors

$$\boldsymbol{v}_\alpha = \begin{pmatrix}\sin(\theta_\mathrm{T}/2) \\ -\cos(\theta_\mathrm{T}/2)\end{pmatrix} , \ \boldsymbol{v}_\beta = \begin{pmatrix}\cos(\theta_\mathrm{T}/2) \\ \sin(\theta_\mathrm{T}/2)\end{pmatrix} . \tag{4.31}$$

With this choice of polarisation vectors, the matrix elements of $\boldsymbol{V}$ are diagonal. The first order energy corrections due to $\boldsymbol{V}$ are the eigenvalues $E_{n\alpha}$ and $E_{n\beta}$, which are added to the unperturbed energy (4.27).

With this knowledge, we can proceed to determine the first order corrections to these states. These are given only in terms of states for different quantum numbers, i.e. (for $\xi \in \{\alpha, \beta\}$) [38]

$$|\phi_{n,\xi'}^1\rangle = \sum_{m\neq n,\xi} \frac{-\langle\phi_{m,\xi}^0|\hat{V}|\phi_{n,\xi'}^0\rangle}{E_m^0 - E_n^0}|\phi_{m,\xi}^0\rangle . \tag{4.32}$$

Therefore, to proceed, we need to determine the matrix elements for different quantum numbers. These are determined in A.6.1 as (again, element at first

row and first column corresponds to $\xi = \alpha, \xi' = \alpha$, second row first column corresponds to $\xi = \beta, \xi' = \alpha$ etc.)

$$\langle \phi^0_{m,\xi} | \hat{V} | \phi^0_{n,\xi'} \rangle = \epsilon Z^2 \sin\left(\frac{n\pi}{N+1}\right) \sin\left(\frac{m\pi}{N+1}\right) \times \tag{4.33}$$

$$\times \begin{pmatrix} \cos^2(\theta_\mathrm{T}/2)\left((-1)^{m+n}+1\right) & \sin(\theta_\mathrm{T}/2)\cos(\theta_\mathrm{T}/2)\left((-1)^{m+n}-1\right) \\ \sin(\theta_\mathrm{T}/2)\cos(\theta_\mathrm{T}/2)\left((-1)^{m+n}-1\right) & \sin^2(\theta_\mathrm{T}/2)\left((-1)^{m+n}+1\right) \end{pmatrix} . \tag{4.34}$$

We can see that the diagonal terms are only non-zero for $m+n$ even, while off-diagonal elements are only non-zero for $m+n$ odd. Hence, the corrections to the state with polarisation α is given as

$$|\phi^1_{n,\alpha}\rangle = \epsilon Z^2 \left(\sum_{m\neq n,(m+n)\text{ even}} \frac{\sin\left(\frac{n\pi}{N+1}\right)\sin\left(\frac{m\pi}{N+1}\right)\cos^2(\theta_\mathrm{T}/2)}{t\left(\cos\left(\frac{m\pi}{N+1}\right)-\cos\left(\frac{n\pi}{N+1}\right)\right)} |\phi^0_{m,\alpha}\rangle - \tag{4.35}$$

$$- \sum_{m\neq n,(m+n)\text{ odd}} \frac{\sin\left(\frac{n\pi}{N+1}\right)\sin\left(\frac{m\pi}{N+1}\right)\sin(\theta_\mathrm{T}/2)\cos(\theta_\mathrm{T}/2)}{t\left(\cos\left(\frac{m\pi}{N+1}\right)-\cos\left(\frac{n\pi}{N+1}\right)\right)} |\phi^0_{m,\beta}\rangle \right) . \tag{4.36}$$

Similarly,

$$|\phi^1_{n,\beta}\rangle = \epsilon Z^2 \left(\sum_{m\neq n,(m+n)\text{ even}} \frac{\sin\left(\frac{n\pi}{N+1}\right)\sin\left(\frac{m\pi}{N+1}\right)\sin^2(\theta_\mathrm{T}/2)}{t\left(\cos\left(\frac{m\pi}{N+1}\right)-\cos\left(\frac{n\pi}{N+1}\right)\right)} |\phi^0_{m,\beta}\rangle - \tag{4.37}$$

$$- \sum_{m\neq n,(m+n)\text{ odd}} \frac{\sin\left(\frac{n\pi}{N+1}\right)\sin\left(\frac{m\pi}{N+1}\right)\sin(\theta_\mathrm{T}/2)\cos(\theta_\mathrm{T}/2)}{t\left(\cos\left(\frac{m\pi}{N+1}\right)-\cos\left(\frac{n\pi}{N+1}\right)\right)} |\phi^0_{m,\alpha}\rangle \right) . \tag{4.38}$$

With these corrections to the state, we can calculate the corrections to helicity

$$h^1_{n\alpha,n\alpha} = \left(\langle\phi^0_{n,\alpha}| + \langle\phi^1_{n,\alpha}|\right)\hat{h}\left(|\phi^0_{n,\alpha}\rangle + |\phi^1_{n,\alpha}\rangle\right) \approx \langle\phi^0_{n,\alpha}|\hat{h}|\phi^1_{n,\alpha}\rangle + \langle\phi^1_{n,\alpha}|\hat{h}|\phi^0_{n,\alpha}\rangle , \tag{4.39}$$

where we kept only contributions to the first order and used $\langle\phi^0_{n,\alpha}|\hat{h}|\phi^0_{n,\alpha}\rangle = 0$. Again, we will need to calculate matrix elements, this time of the helicity operator. The general form is

$$\langle \phi^0_{n,\xi} | \hat{h} | \phi^0_{m,\mu} \rangle = \frac{Z^2}{2} \begin{pmatrix} \sin\left(\frac{n\pi}{N+1}\right)\boldsymbol{v}^\dagger_\xi & \sin\left(\frac{2n\pi}{N+1}\right)\boldsymbol{v}^\dagger_\xi & \ldots \end{pmatrix} \times \tag{4.40}$$

$$\times \begin{pmatrix} \sin\left(\frac{2m\pi}{N+1}\right)\boldsymbol{R}(-\pi/2)\boldsymbol{v}_\mu \\ \sin\left(\frac{3m\pi}{N+1}\right)\boldsymbol{R}(-\pi/2)\boldsymbol{v}_\mu + \sin\left(\frac{m\pi}{N+1}\right)\boldsymbol{R}(\pi/2)\boldsymbol{v}_\mu \\ \vdots \\ \sin\left(\frac{(N-1)m\pi}{N+1}\right)\boldsymbol{R}(\pi/2)\boldsymbol{v}_\mu \end{pmatrix} . \tag{4.41}$$

Using $\boldsymbol{R}(\pi/2) = -R(-\pi/2)$, we determine

$$\langle \phi^0_{n,\xi} | \hat{h} | \phi^0_{m,\mu} \rangle = Z^2 \sin\left(\frac{m\pi}{N+1}\right) \begin{pmatrix} \sin\left(\frac{n\pi}{N+1}\right)\boldsymbol{v}^\dagger_\xi & \sin\left(\frac{2n\pi}{N+1}\right)\boldsymbol{v}^\dagger_\xi & \ldots \end{pmatrix} \times \tag{4.42}$$

$$\times \begin{pmatrix} \cos\left(\frac{m\pi}{N+1}\right)\boldsymbol{R}(-\pi/2)\boldsymbol{v}_\mu \\ \cos\left(\frac{2m\pi}{N+1}\right)\boldsymbol{R}(-\pi/2)\boldsymbol{v}_\mu \\ \vdots \\ \cos\left(\frac{Nm\pi}{N+1}\right)\boldsymbol{R}(-\pi/2)\boldsymbol{v}_\mu \end{pmatrix} , \tag{4.43}$$

$$\langle \phi^0_{n,\xi}|\hat{h}|\phi^0_{m,\mu}\rangle = Z^2 \sin\left(\frac{m\pi}{N+1}\right)\left(\boldsymbol{v}^\dagger_\xi \boldsymbol{R}(-\pi/2)\boldsymbol{v}_\mu\right)\times \tag{4.44}$$

$$\times\left(\sum_{k=1}^{N}\sin\left(\frac{kn\pi}{N+1}\right)\cos\left(\frac{km\pi}{N+1}\right)\right) = \tag{4.45}$$

$$= \frac{Z^2}{2}\sin\left(\frac{m\pi}{N+1}\right)\left(\boldsymbol{v}^\dagger_\xi \boldsymbol{R}(-\pi/2)\boldsymbol{v}_\mu\right)\times \tag{4.46}$$

$$\times\left(\sum_{k=1}^{N}\sin\left(\frac{k(n+m)\pi}{N+1}\right)+\sin\left(\frac{k(n-m)\pi}{N+1}\right)\right). \tag{4.47}$$

The formulas for these sine summations are best derived by transforming the sines to complex exponentials as shown in A.4, which lead to the following result

$$\sum_{k=1}^{N}\left(\sin\left(\frac{(n+m)\pi}{N+1}\right)+\sin\left(\frac{(n-m)\pi}{N+1}\right)\right) = \frac{2\sin\left(\frac{n\pi}{N+1}\right)}{\cos\left(\frac{n\pi}{N+1}\right)-\cos\left(\frac{m\pi}{N+1}\right)}. \tag{4.48}$$

Substituting back into expression for matrix element of helicity, we get

$$\langle \phi^0_{n,\xi}|\hat{h}|\phi^0_{m,\mu}\rangle = \left(\boldsymbol{v}^\dagger_\xi \boldsymbol{R}(-\pi/2)\boldsymbol{v}_\mu\right)\frac{(-Z^2)\sin\left(\frac{m\pi}{N+1}\right)\sin\left(\frac{n\pi}{N+1}\right)}{\cos\left(\frac{m\pi}{N+1}\right)-\cos\left(\frac{n\pi}{N+1}\right)} \tag{4.49}$$

for odd $m+n$, otherwise the matrix element is zero. We can very simply see that the term has to be off-diagonal in polarization degree of freedom, as the bracketed term with vectors has matrix structure (first row second column corresponds to $\xi=\alpha$ and $\mu=\beta$)

$$\begin{pmatrix} 0 & 1 \\ -1 & 0 \end{pmatrix}. \tag{4.50}$$

Therefore, we have only two possibilities for non-zero helicity matrix elements, which also require that $m+n$ is odd

$$\langle \phi^0_{n,\alpha}|\hat{h}|\phi^0_{m,\beta}\rangle = \frac{(-Z^2)\sin\left(\frac{m\pi}{N+1}\right)\sin\left(\frac{n\pi}{N+1}\right)}{\cos\left(\frac{m\pi}{N+1}\right)-\cos\left(\frac{n\pi}{N+1}\right)} = -\langle \phi^0_{n,\beta}|\hat{h}|\phi^0_{m,\alpha}\rangle . \tag{4.51}$$

Therefore, after substituting from (4.36) to $\langle \phi^0_{n,\alpha}|\hat{h}|\phi^1_{n,\alpha}\rangle$ and applying the above result, we have

$$\langle \phi^0_{n,\alpha}|\hat{h}|\phi^1_{n,\alpha}\rangle = \sum_{m\neq n,(m+n)\text{ odd}}\frac{\epsilon Z^4\sin(\theta_{\mathrm{T}})\sin^2\left(\frac{n\pi}{N+1}\right)\sin^2\left(\frac{m\pi}{N+1}\right)}{2t\left(\cos\left(\frac{m\pi}{N+1}\right)-\cos\left(\frac{n\pi}{N+1}\right)\right)^2} = \langle \phi^1_{n,\alpha}|\hat{h}|\phi^0_{n,\alpha}\rangle . \tag{4.52}$$

Similarly

$$\langle \phi^0_{n,\beta}|\hat{h}|\phi^1_{n,\beta}\rangle = -\sum_{m\neq n,(m+n)\text{ odd}}\frac{\epsilon Z^4\sin^2\left(\frac{n\pi}{N+1}\right)\sin^2\left(\frac{m\pi}{N+1}\right)\sin(\theta_{\mathrm{T}})}{2t\left(\cos\left(\frac{m\pi}{N+1}\right)-\cos\left(\frac{n\pi}{N+1}\right)\right)^2} = \langle \phi^1_{n,\beta}|\hat{h}|\phi^0_{n,\beta}\rangle , \tag{4.53}$$

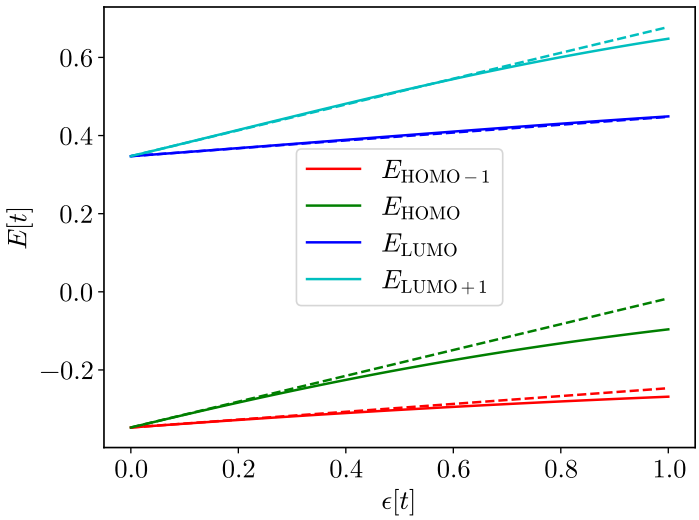

Figure 4.14: The energy of LUMO+1,LUMO, HOMO and HOMO-1 as function of the perturbation ϵ. Match in the slopes of the numerical and analytical results for $\epsilon \to 0$ indicates validity of the perturbative approach.

which leads to our final result

$$h^1_{n,\alpha} = \frac{\epsilon}{t} Z^4 \sin(\theta_{\mathrm{T}}) \zeta_{nm} \,, \tag{4.54}$$

$$h^1_{n,\beta} = -\frac{\epsilon}{t} Z^4 \sin(\theta_{\mathrm{T}}) \zeta_{nm} \,, \tag{4.55}$$

$$\zeta_{nm} = \sum_{m \neq n, (m+n) \text{ odd}} \frac{\sin^2\left(\frac{n\pi}{N+1}\right) \sin^2\left(\frac{m\pi}{N+1}\right)}{\left(\cos\left(\frac{m\pi}{N+1}\right) - \cos\left(\frac{n\pi}{N+1}\right)\right)^2} \,. \tag{4.56}$$

Notice that ζ_{nm} is always positive and hence that opposite polarisations acquire opposite helicity to the first order.

4.2.5 Comparison of Perturbative Analytic Solution and Full Numerical Solution

We evaluated the eigenstates and helicity of the states also numerically, giving us access to comparison of the perturbation theory with numerically exact results. The numerical solution uses exact numerical diagonalisation of the Hamiltonian, using the julia [40] language. The script is presented in [41]. Fig. 4.14 shows the energy of initially degenerate states, calculated both analytically and numerically. Analytically, the energy is of course linearly proportional to perturbation ϵ, as we included first order corrections. Importantly, slopes close to $\epsilon \to 0$ seem to match well, proving that the perturbation approach is valid.

We now compare the numerically calculated helicity to the analytically predicted helicity to the first order. We choose a constant ϵ and scan through all θ_{T}. We overlay the helicity prediction with the energy of the orbitals.

As can be seen in Fig. 4.15, the states with different polarisation α and β switch in energy order for $\theta_{\mathrm{T}} = \frac{\pi}{2}, \frac{3\pi}{2}$. This causes rapid change of the helicity that is numerically attributed to HOMO/HOMO-1. From Fig. 4.15 it is also

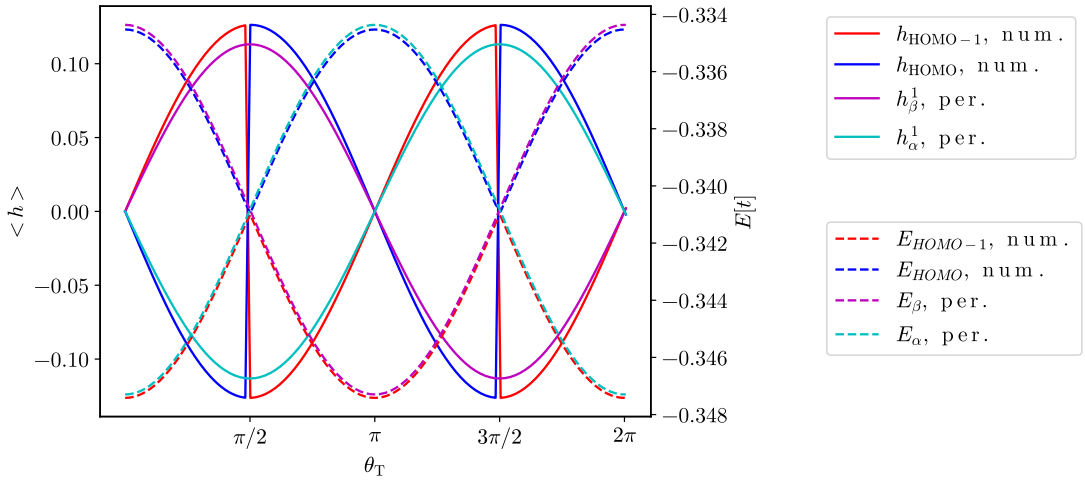

Figure 4.15: The HOMO-1 and HOMO helicities and energies, overlayed. This shows that at $\theta_{\mathrm{T}} = \pi/2, 3\pi/2$ the order of the orbitals swaps, while their helicities remain opposite. This results in a jump in numerically observed helicity, as the numerical solution switches the HOMO label from polarization α to β. The analytical first order corrections to both energy and helicity describe qualitative properties of the system well. Perturbation ϵ is kept constant at $\epsilon = 0.15t$.

clear that the majority of the helicity expectation value is explainable by the first order correction in this regime.

Finally, we provide a phase diagram of the numerically calculated helicity as function of both the angle θ_{T} and the perturbation ϵ in Fig. 4.16

4.2.6 Numerically Calculated Angular Momentum

While the presence of helicity is important for understanding of the switching behaviour around the neighbouring orbitals, the ultimate observable we are interested in is the angular momentum. The matrix representing the angular momentum operator was already derived in (4.16).

We can check that matrix elements for states $|\phi^0_{m,\gamma}\rangle$ are almost always zero as follows below.

$$\langle\phi^0_{m,\gamma}|\hat{L}_{z,S}|\phi^0_{n,\xi}\rangle = \hbar Z^2 \left(\sin\left(\tfrac{m\pi}{N+1}\right)\boldsymbol{v}^\dagger_\gamma \quad \sin\left(\tfrac{2m\pi}{N+1}\right)\boldsymbol{v}^\dagger_\gamma \quad ...\right) \times \tag{4.57}$$

$$\times \begin{pmatrix} \sin\left(\tfrac{n\pi}{N+1}\right)\boldsymbol{\sigma}_2\boldsymbol{v}_\xi \\ \sin\left(\tfrac{2n\pi}{N+1}\right)\boldsymbol{\sigma}_2\boldsymbol{v}_\xi \\ \vdots \end{pmatrix} = \tag{4.58}$$

$$= \hbar Z^2 \left(\boldsymbol{v}^\dagger_\gamma\boldsymbol{\sigma}_2\boldsymbol{v}_\xi\right)\left(\sum_{k=1}^{N}\sin\left(\frac{km\pi}{N+1}\right)\sin\left(\frac{kn\pi}{N+1}\right)\right) . \tag{4.59}$$

The last sum in the brackets is the same sum as present in the orthogonalisation sum of the original eigenvectors (see A.4) and hence equals to zero for all $m \neq n$. For $m = n$, we the summation is exactly inverse of Z^2 and we have

$$\langle\phi^0_{n,\gamma}|\hat{L}_{z,S}|\phi^0_{n,\xi}\rangle = \hbar\boldsymbol{v}^\dagger_\gamma\boldsymbol{\sigma}_2\boldsymbol{v}_\xi \tag{4.60}$$

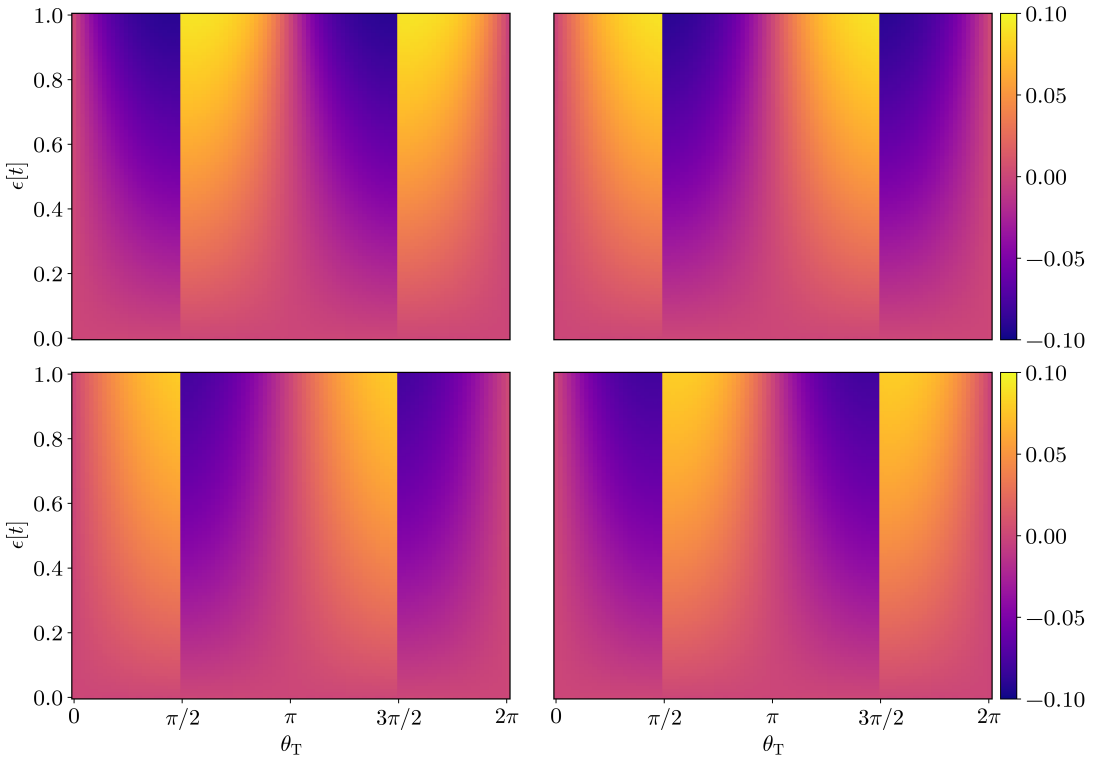

Figure 4.16: From top left clockwise : LUMO+1, LUMO, HOMO and HOMO-1 numerically calculated helicities. We observe the abrupt change of helicity at the switching of each orbital around $\theta_T = \pi/2, 3\pi/2$. We also see that states on the opposite side of the Fermi energy have the opposite helicity.

and we recover the analogous elements on planar eigenstates

$$\langle \phi^0_{n,\alpha} | \hat{L}_{z,S} | \phi^0_{n,\beta} \rangle = -i\hbar = -\langle \phi^0_{n,\beta} | \hat{L}_{z,S} | \phi^0_{n,\alpha} \rangle \,, \tag{4.61}$$

$$\langle \phi^0_{n,\alpha} | \hat{L}_{z,S} | \phi^0_{n,\alpha} \rangle = 0 = \langle \phi^0_{n,\beta} | \hat{L}_{z,S} | \phi^0_{n,\beta} \rangle \,. \tag{4.62}$$

From the form of the state corrections in (4.36) and (4.38), it is clear that not even first order corrections to the state induce the angular momentum in the system. This is because the system is still in equilibrium. For any angular momentum to occur, a current through the system must be flowing. We therefore apply standard NEGF transport formalism, as described in 2. We choose simplified form of self-energy

$$\mathbf{\Sigma}^R = \begin{pmatrix} i\eta \boldsymbol{I} & \mathbf{0} & \mathbf{0} & \dots \\ \mathbf{0} & \mathbf{0} & \mathbf{0} & \dots \\ \vdots & \vdots & \vdots & \ddots \\ \dots & \mathbf{0} & \mathbf{0} & i\eta \boldsymbol{I} \end{pmatrix} , \tag{4.63}$$

which is imaginary and independent of energy. The expectation value of the many-body angular momentum operator will be given by (in the basis of $|p_{n,x/y}\rangle$) [18]

$$\left\langle \hat{L}_z \right\rangle = \sum_{n,\gamma,m,\xi} \langle \phi^0_{n,\gamma} | \hat{L}_{z,S} | \phi^0_{m,\xi} \rangle \left\langle \hat{a}^\dagger_{n,\gamma} \hat{a}_{m,\xi} \right\rangle = \sum_n (-i\hbar) \left\langle \hat{a}^\dagger_{n,x} \hat{a}_{n,y} \right\rangle + i\hbar \left\langle \hat{a}^\dagger_{n,y} \hat{a}_{n,x} \right\rangle \,. \tag{4.64}$$

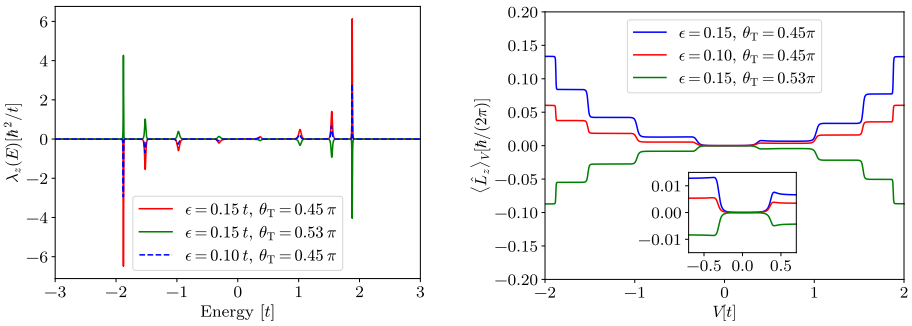

(a) Angular momentum energy density (b) Angular momentum at given bias

Figure 4.17: The angular momentum energy density (a) calculated from the lesser Green's function. The imaginary part of the coupling self-energy is $\eta = 0.1t$. Note that for different θ_T, the peaks can change in sign, while for different ϵ, they differ mainly in magnitude. The steps in (b) correspond to locations of peaks in $\lambda_z(E)$, as $\left\langle \hat{L}_z \right\rangle$ is obtained by integrating $\lambda_z(E)$ in the transport window.

Recognizing the lesser Green's function allows us to rewrite this as

$$\left\langle \hat{L}_z \right\rangle = \int \frac{dE}{2\pi\hbar} \lambda_z(E) = \int \frac{dE}{2\pi\hbar} \hbar^2 \sum_n \left(G^<_{ny,nx}(E) - G^<_{nx,ny}(E) \right) . \tag{4.65}$$

Notice that since in equilibrium, the angular momentum is zero, only the non-equilibrium part contributes, which is non-zero only in the transport window, i.e. in the energy interval given by differences in Fermi-Dirac distributions of left and right reservoir

$$\left\langle \hat{L}_z \right\rangle = \int \frac{dE}{2\pi\hbar} \lambda_z(E) \left(f_L(E) - f_R(E) \right) , \tag{4.66}$$

where $f_{L/R}(E)$ is the Fermi-Dirac distribution of the left/right electrode. Besides θ_T and ϵ, we therefore add a third free parameter to the model - η, but the role of the parameter is rather trivial - the angular momentum is directly proportional to it.

We show numerically calculated values of $\lambda_z(E)$ for chosen set of parameters in Fig. 4.17a.

The peaks in the Green's function follow same qualitative dependencies as the helicity, as is shown in Fig. 4.18 (to be compared with Fig. 4.15). The total angular momentum generated at specific bias is then shown in Fig. 4.17b.

4.2.7 Angular Symmetry and Persistent Rotation

So far, our analysis deals with a static situation - the momentum is generated by current flowing in Born-Oppenheimer approximation[25], i.e. with static nuclei. The dynamics of the molecular rotation will undoubtedly present additional aspect of the rotation. One example that we can check is whether the momentum generated for specific voltage is net positive for the whole range of angles of the molecular rotation.

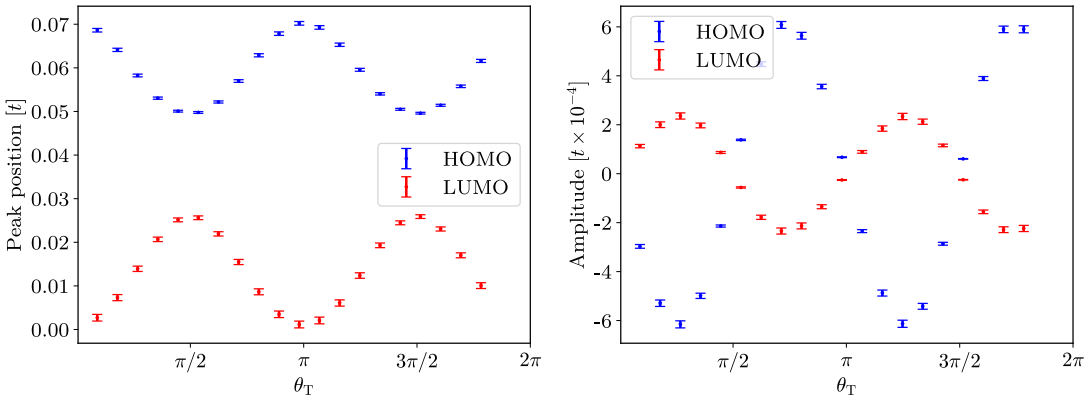

Figure 4.18: Fitted peak positions and amplitudes for $\lambda_z(E)$ for range of angles and constant penalty $\epsilon = 0.2$. The qualitative behaviour of the energy corrections coincides with energy corrections in first order perturbation theory, but the energies are somewhat offset. The amplitude of the peaks more closely resembles the helicity dependence observed in equilibrium situation.

From the shape of the dependence of peak amplitude on the twist angle as in Fig. 4.18, we suspect that over these angles, angular momentum averages to zero, and this is indeed observed, as shown in Fig. 4.19.

This would seem to predict that the molecule should not rotate continuously, but just oscillate between certain rotations with opposite momentum. But, the dynamics of the molecule can in fact play an important role and can cause the molecule to rotate faster through regions where it would gain significant angular momentum in opposite direction.

4.2.8 Conclusions for Helical Orbitals and Ring Currents

We have shown that both in a simplistic Hückel-like model and in ab-initio calculations, triple bond cumulene systems can host helical orbitals. These helical orbitals, when the system is brought out of equilibrium by applying a bias and letting electrons flow through it, induce symmetric angular momentum direction of the current with respect to the sign of the bias.

In the model system, we have shown that the operators of helicity and angular momentum commute and that the helicity is a good proxy for the behaviour of the angular momentum, indicating possibility of presence of angular momentum based only on equilibrium orbital calculations.

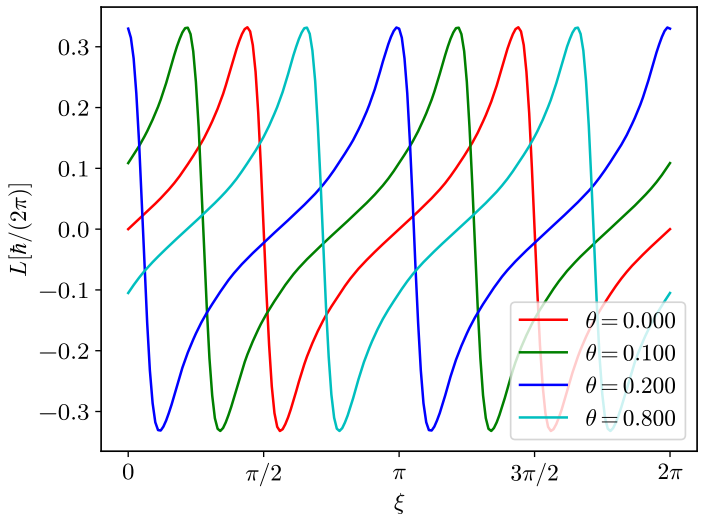

Figure 4.19: The dependence of generated angular momentum on the additional angle ξ which rotates the last basis pair, effectively transforming $\theta_{\mathrm{T}} \rightarrow \theta_{\mathrm{T}} + \xi$. As expected, θ_{T} then only sets the start position of a cyclic pattern with average zero angular momentum. The bias was chosen large enough to ensure transport through all unoccupied angular momentum energy density peaks.

4.3 Gap Scaling in Sodium Clusters

In cluster based molecular conductance calculations[1], the extended molecule includes part of the electrodes and is coupled to the rest of the electrodes via self-energy, as explained in 3. But, the exact amount of the electrode that needs to be included in the ab-initio calculation is a priori unknown. One expects that sufficient part of the electrodes has been included in the calculation if the properties of the junction are not changing with the electrode size. We would call such calculation converged with respect to electrode size.

While such convergence calculations were done on the level of DFT [42], we are not aware of such calculations at the level of evGW. Our contribution is therefore calculations of electronic structure at the evGW level of metallic clusters of different sizes. For the sake of computational simplicity, we chose the sodium clusters as these have simple metallic character while containing only few electrons. From the properties of electronic structure, we investigate the LUMO-HOMO gap of the electrodes and energy level separation of clusters, as these are known to influence the conductance significantly[42, 43, 44].

Furthermore, geometric perturbations are known to have significant effect on the desired electronic structure properties [42]. We therefore calculate average properties by choosing different random geometries of clusters with same number of atoms. These "cluster realisations" allow for systematic estimate of uncertainty due to geometry perturbations of the finite clusters.

4.3.1 DFT Starting Point

A starting point for evGW calculation in our methodology is a DFT calculation. We can therefore also note the observed electronic structure properties for comparison. We focus on the LUMO-HOMO gap of the cluster and the average

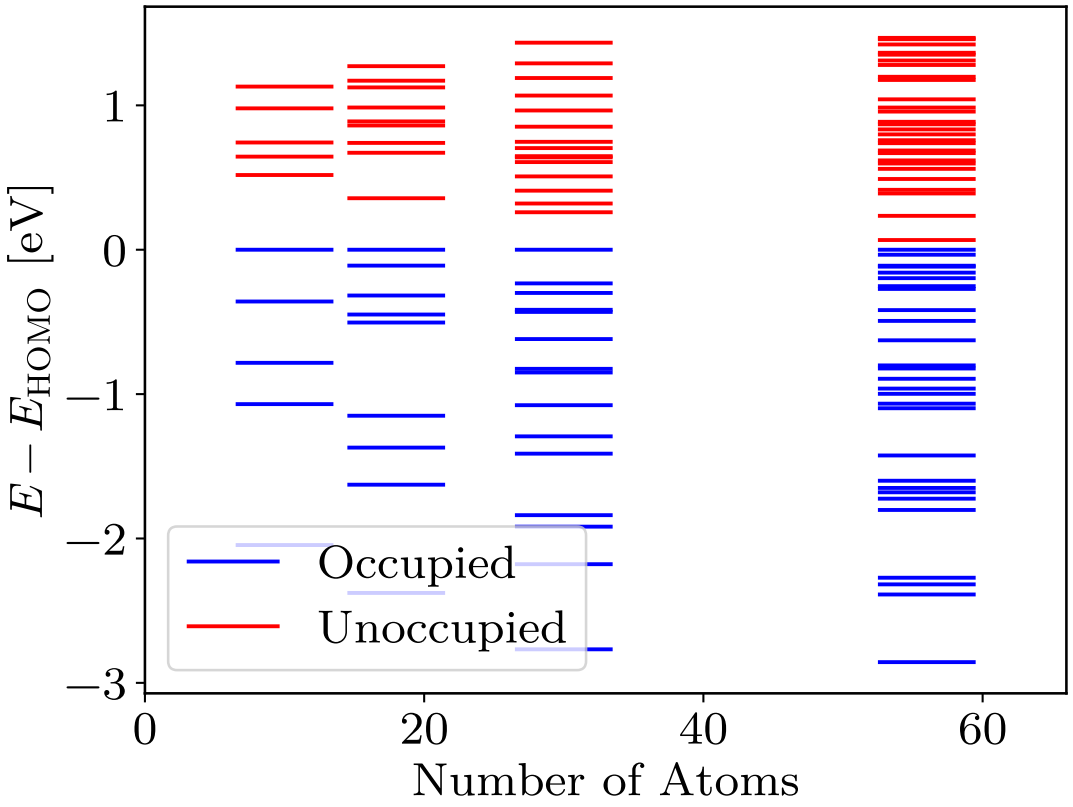

Figure 4.20: Spectrum of chosen sodium clusters calculated in DFT is shown around the LUMO-HOMO gap. Occupied quasiparticle energy levels are shown in blue and unoccupied in red. With the increasing cluster volume, the density of the states increases and the gap closes. In each cluster, symmetry degeneracies cause the spectrum to not be equidistant in energy. In order to study the convergence properties of the spectrum with cluster volume, we need to consider average values derived from ensemble of clusters.

energy level spacing of valence orbitals. The precise definitions of the gap, the average energy level spacing and their uncertainties is given in A.7. In short, the gap in DFT is determined as the average of differences between the LUMO and HOMO Kohn-Sham orbitals over available cluster realisations. The energy spacing is determined as average difference between M consecutive highest occupied or lowest unoccupied levels, where M is given as half the number of valence electrons for sodium, i.e. for $2M$ sodium atoms, M levels are taken into the averaging set. The systems are closed-shell - the orbitals are exactly pair occupied.

The Kohn-Sham spectrum of DFT calculation is shown in Fig. 4.20. The shape of the clusters was chosen to be spherical, in order to minimize possible influence of discrete symmetries present for example in pyramidal/cubic clusters - these cause energy level separation, which pollutes the statistics of the electronic structure. Examples of cluster geometries are given in Fig. 4.21.

All spherical clusters are fully geometrically optimised in the def2-TZVP basis at the DFT level. For the behaviour of the electronic structure properties as function of the basis set size and functional choice, see A.8, which also includes information about the convergence criteria for the calculations. The resultant

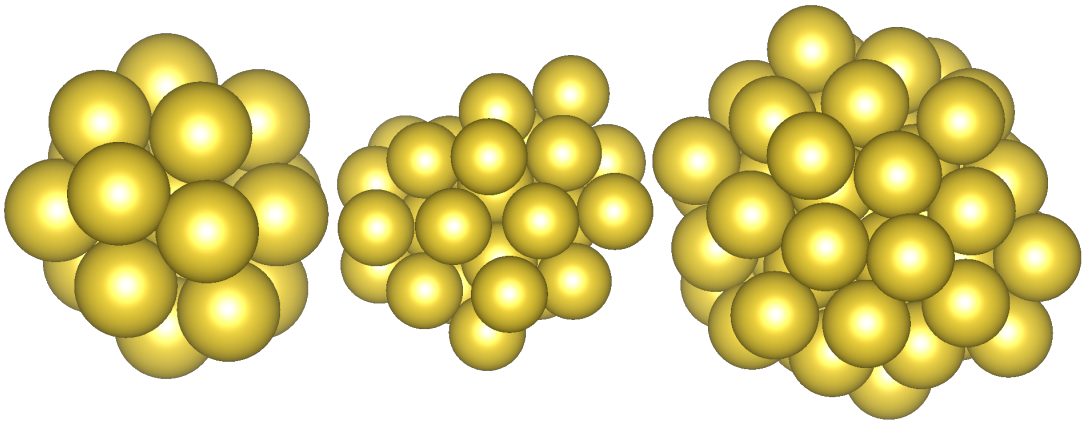

Figure 4.21: Several examples of spherical clusters of different volumes. More realisations of the spherical clusters are present in the calculations, usually differentiated by add-atom positions.

indicators of the electronic structure at the DFT level are summarized in Fig. 4.22.

The LUMO-HOMO gap scales with an exponent similar to scaling of occupied energy level spacings. The scaling is proportional to $1/V$, which is an expected result from the random matrix theory [45]. On the other hand, the unoccupied levels tend to converge slower.

4.3.2 Sodium Clusters in evGW

As correction to the DFT, evGW gives increased precision for the excited state energies while not requiring unreasonable calculation cost. The electronic structure indicators of clusters geometrically optimised in DFT and recalculated with evGW are summarized in Fig. 4.23

Clearly, the value of the LUMO-HOMO gap is significantly increased in evGW and its scaling is much slower. Our claim is that this behaviour is caused by the Coulombic repulsion of the extra charge localised on the cluster in the first excited state. To support this claim, we provide two comparisons - simple analytical scaling argument and numerical Hartree-Fock calculation, which is known to include extra single electron repulsion across the LUMO-HOMO gap[25]. Both are discussed below.

4.3.3 Charge on a Sphere - Scaling Analysis

Consider a sphere of radius R with homogeneous charge density

$$\rho = \frac{e}{\frac{4}{3}\pi R^3} \,, \tag{4.67}$$

i.e. single electron charge dispersed across the sphere volume. The energy due to self-interaction of the charge density is given by Coulomb integral

$$U = \int d^3r' \int d^3r \frac{\rho(\boldsymbol{r})\rho(\boldsymbol{r}')}{4\pi\epsilon_0|\boldsymbol{r}-\boldsymbol{r}'|} = \frac{e^2}{4\pi\epsilon_0 V^2} \int d^3r \int d^3r' \frac{1}{|\boldsymbol{r}-\boldsymbol{r}'|} \,, \tag{4.68}$$

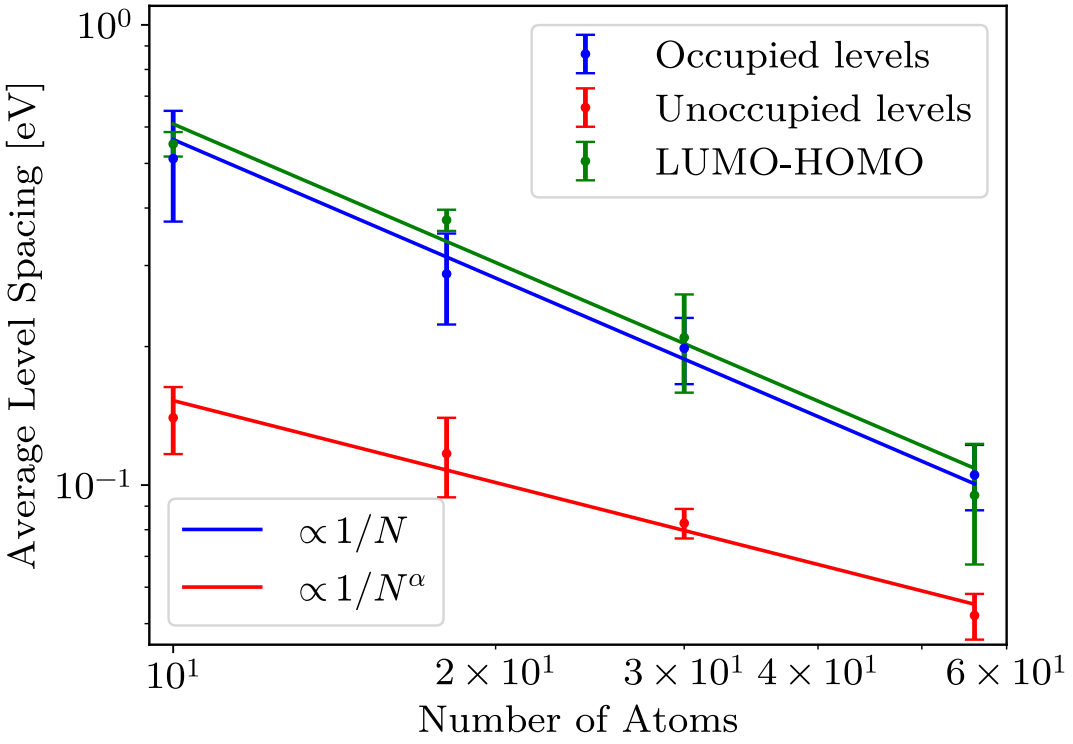

Figure 4.22: Above is presented the average spacing between quasiparticle energy levels for occupied valence orbitals (blue) and unoccupied conduction orbitals (red) of sodium clusters. In green, the average LUMO-HOMO gap of the clusters is shown. In both cases, the values reduce with cluster size, which is indicative of more and more discrete states present in any chosen energy interval. The LUMO-HOMO gap does not differ significantly in value nor in scaling from the spacing of occupied orbitals. Unoccupied orbital spacings tend to scale slower than occupied orbital spacings, but the value is overall smaller than for the occupied orbitals.

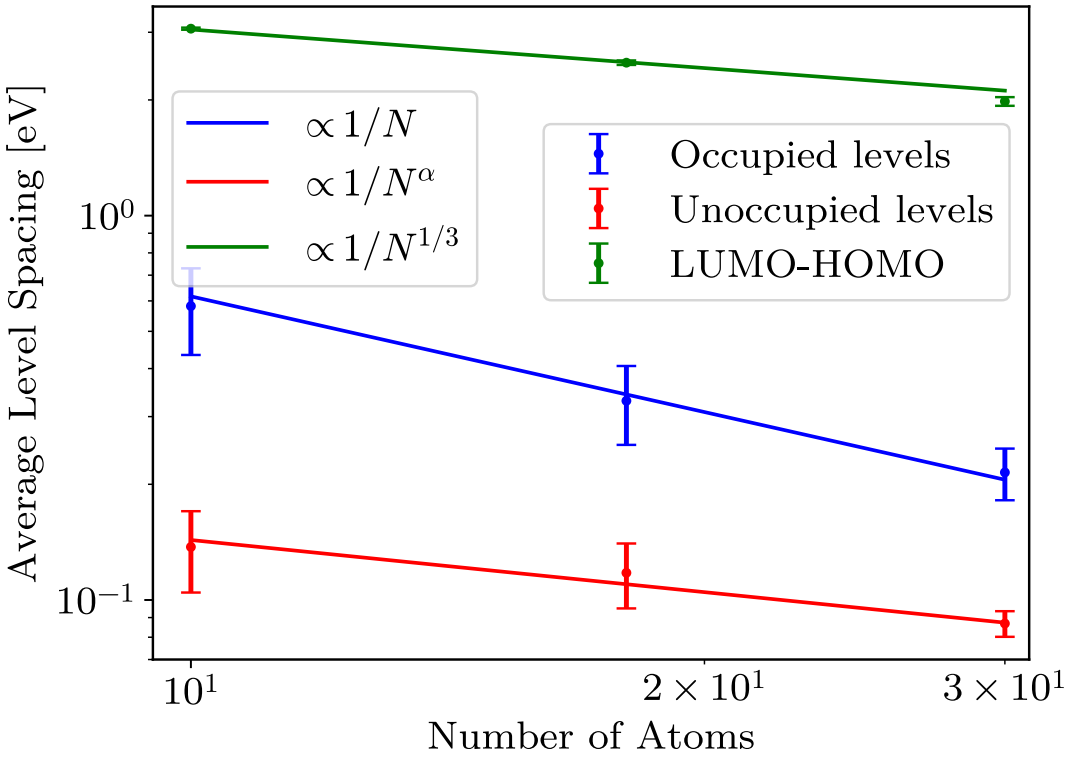

Figure 4.23: The scaling of the average quasiparticle energy level spacing for occupied and unoccupied orbitals of spherical sodium clusters in evGW and LUMO-HOMO gap in the same approach. While the occupied level spacing scales at speeds similar to DFT, the LUMO-HOMO gap scales significantly slower and acquires larger value.

where $V = \frac{4}{3}\pi R^3$ is the volume of the sphere. The integrations run over the volume of the sphere. For the inner integral, we introduce the spherical polar coordinates with z axis along the $\boldsymbol{r}$ direction. Then, the magnitude of the difference of the two position vectors is given only in terms of their respective magnitudes and polar angle θ.

$$|\boldsymbol{r} - \boldsymbol{r}'| = \sqrt{r^2 + (r')^2 - 2rr'\cos(\theta')}\,. \tag{4.69}$$

Clearly, there is no dependence on azimuthal angle in either integration, therefore we can write the parametrized integration as

$$U = \frac{\pi e^2}{\epsilon_0 V^2}\int_0^R r^2 dr \int_0^\pi \sin\theta d\theta \int_0^R (r')^2 dr' \int_0^\pi \sin(\theta')d\theta' \frac{1}{\sqrt{r^2 + (r')^2 - 2rr'\cos(\theta')}}\,. \tag{4.70}$$

The innermost integration is carried out by substitution $z = \cos\theta'$, which leads to integral

$$\int_{-1}^1 dz \frac{1}{\sqrt{r^2 + (r')^2 - 2rr'z}} = \left[\frac{-1}{rr'}\sqrt{r^2 + (r')^2 - 2rr'z}\right]_{-1}^1 = \tag{4.71}$$

$$= \frac{1}{rr'}\left(r + r' - |r - r'|\right)\,. \tag{4.72}$$

Since there is no dependence on the θ variable, the integration in θ is trivial and results in an extra factor of 2 and we are left with double integration

$$U = \frac{2\pi e^2}{\epsilon_0 V^2}\int_0^R r dr \int_0^R dr' r'(r + r' - |r - r'|)\,. \tag{4.73}$$

We eliminate the absolute value by splitting the inner integral into two parts

$$\int_0^R dr' r'(r + r' - |r - r'|) = \int_0^r dr' r'(r + r' - r + r') + \tag{4.74}$$

$$+ \int_r^R dr' r'(r + r' - r' + r) = \frac{2}{3}r^3 + \left[r(r')^2\right]_r^R = rR^2 - \frac{1}{3}r^3\,. \tag{4.75}$$

The outer integration therefore reads

$$U = \frac{2\pi e^2}{\epsilon_0 V^2}\left(\int_0^R r^2 R^2 dr - \frac{1}{3}\int_0^R r^4 dr\right) = \frac{2\pi e^2}{\epsilon_0 V^2}\left(\frac{1}{3} - \frac{1}{15}\right)R^5 = \frac{2e^2}{5\epsilon_0 V}R^2\,, \tag{4.76}$$

where we used $V = \frac{4}{3}\pi R^3$. From this definition of V we can also see that this interaction energy scales as $U \propto V^{1/3}$. This supports our claim that the LUMO-HOMO energy gap is increased by extra electron repulsion, since we observe the same scaling of the gap.

4.3.4 Extra Interaction via Hartree-Fock Method

In the Hartree-Fock method, the many-body state of the interacting electron system is approximated by a Slater determinant - an antisymmetric combination of single particle states[25]. The Hamiltonian matrix - which is constructed in

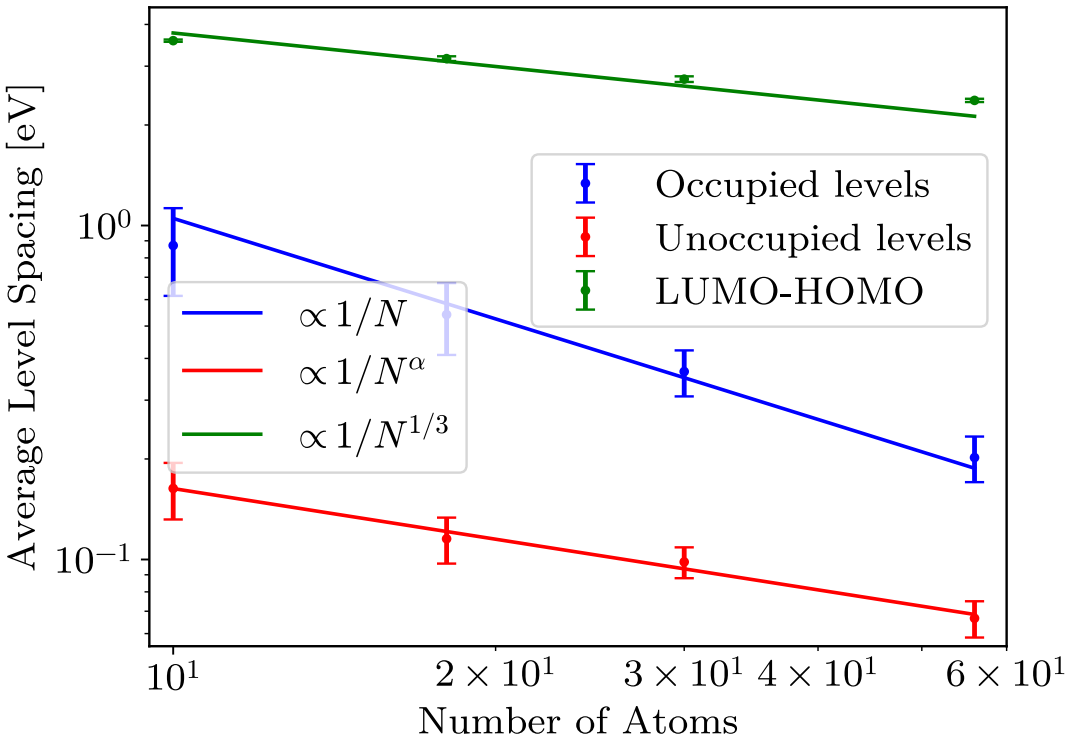

Figure 4.24: The average energy level spacing as produced by the Hartree-Fock approach, together with the LUMO-HOMO gap. The LUMO-HOMO gap scales approximately as $V^{-1/3}$, where V is the volume of the spherical sodium cluster, which is consistent with the charge on a sphere model. The occupied and unoccupied gaps scale similarly as in DFT.

the atomic orbital basis by letting the basis become Slater determinant of basis states - then acquires Hartree mean field term and Fock exchange term. Using the same notation as [25] for closed shell Hartree-Fock calculation, we can write the Hartree-Fock Hamiltonian as

$$H_{ij}^{HF} = h_{ij} + \sum_{k}^{N/2} 2J_{k,ij} - K_{k,ij} \,, \tag{4.77}$$

where i, j are atomic basis indices, k are molecular orbital indices (molecular orbitals are obtained by diagonalisation of the Hamiltonian - HF method needs to be solved self-consistently), h_{ij} is the single particle part of the Hamiltonian (kinetic and potential energies), $J_{k,ij}$ is the Hartree repulsion felt by electron due to occupied state k and $K_{k,ij}$ is the Fock exchange energy of the electron due to interaction with state k.

While for occupied levels, the electron always feels repulsion only from other occupied levels, the unoccupied levels include repulsion from all occupied levels. Therefore, across the LUMO-HOMO gap, the repulsion due to an additional orbital should be present, which should scale in the same way as predicted by our scaling argument. The LUMO-HOMO gap and energy level spacings for HF calculations on the DFT geometrically optimized ensemble of clusters are shown in Fig. 4.24.

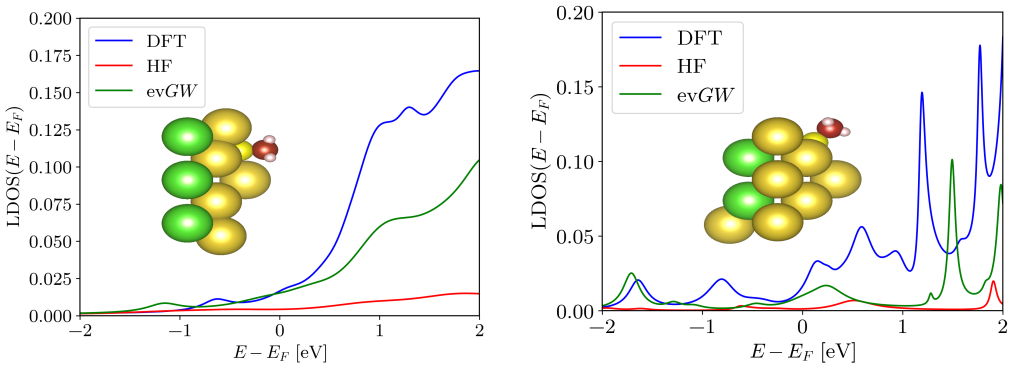

(a) Smaller sodium pyramid

(b) Larger sodium pyramid

Figure 4.25: Local density of states (LDOS) on the carbon atom of methanethiol adsorbed on pyramidal sodium electrode surface. The density is significantly reduced when using Hartree-Focks spectrum and somewhat reduced when using evGW spectrum.

4.3.5 Discussion and Cluster GW Outlook

From the exponent of power law that describes the LUMO-HOMO gap convergence (gap decreases as $V^{-1/3}$ with cluster volume in evGW), we suspect that for finite clusters, the Coulomb (Hartree) interaction term dominates the gap value in evGW approximation for finite metallic clusters. In a realistic molecular break junction setup, the clusters would be effectively infinite and the charging effect of the electrodes would be significantly weaker. In order to account for this in a cluster setup, a very large cluster has to be considered, such that the gap induced on the electrodes is not the dominant gap in the system.

In order to show the influence of the electrode gap on the molecular properties, we also calculated local density of states (LDOS) for methanethiol (MTTL) adsorbed on a pyramidal sodium cluster. In more detail, we calculated the DFT, HF and evGW electronic structure of the pyramidal cluster with the adsorbed molecule and then coupled the pyramidal cluster to reservoirs via model self-energy as in (3.4). This approach is implemented in the AITRANSS package mentioned earlier[20].

The LDOS is calculated for two cluster realisations of different sizes, as shown in Fig. 4.25.

The local density of state is depleted by the effects of the repulsion. Our conclusion is that while DFT systematically overestimates the conductance [3], evGW in cluster approach may underestimate it if care is not taken to include sufficient number of atoms of finite cluster electrodes.

5. Conclusion and Outlook

In this work, we discussed the effects of the electronic structure of molecules on their transport properties. In the first part, we have shown how the interaction with electrodes can induce atypicial conductances via hybridisation with just parts of the molecule. In the second part, we investigated how the current is spatially distributed in the molecule and how this might induce mechanical response by the molecule, specifically in the form of rotation. Lastly, we inquired about the possibility of improving the cluster based calculations via GW to more accurately describe the electronic structure of the electrodes, however we found that for small clusters, the charging energy on the metallic clusters might create unphysical depletion of local density of states on the clusters, leading to artificial decrease in conductance.

There are still many open questions in these problems, exemplifying the richness of the molecular electronics problems. In the first case, we might wonder about the effect of other central metals, for example, vanadocene is known to share some conductance properties with ferrocene[46]. What would be the effect of yet another different metallic ion in place of the iron? In the second part, a true dynamic treatment of the problem should yield description that discriminates between oscillatory and consistent rotation behaviour. In the last part, one could instead of cluster based approximations use periodic boundary conditions. But will this change lead to true elimination of the charging energy, or will this just cause the charging energy to be reduced by effectively doubling the size of the electrode pyramid?

We hope that the broadness of the topics researched in the field of molecular electronics has been introduced to the reader, accenting the necessary collaboration of experimental results, numerical modelling and analytic theoretical understanding of the systems. Our work supports this approach and we believe that the community finds the results of this work interesting and the useful in its endeavour to describe and predict the properties of molecules in junctions more accurately.

Bibliography

[1] Juan Carlos Cuevas and Elke Scheer. *Molecular electronics: an introduction to theory and experiment*. World Scientific, 2010.

[2] Intel. Exactly how small (and cool) is 22 nm? `https://www.intel.com/content/dam/www/public/us/en/documents/corporate-information/history-moores-law-fun-facts-factsheet.pdf`. Accessed: 2023-06-01.

[3] Ferdinand Evers, Richard Korytár, Sumit Tewari, and Jan M van Ruitenbeek. Advances and challenges in single-molecule electron transport. *Rev. Mod. Phys.*, 92(3):035001, 2020.

[4] María Camarasa-Gómez, Daniel Hernangómez-Pérez, Michael S Inkpen, Giacomo Lovat, E-Dean Fung, Xavier Roy, Latha Venkataraman, and Ferdinand Evers. Mechanically tunable quantum interference in ferrocene-based single-molecule junctions. *Nano Lett.*, 20(9):6381–6386, 2020.

[5] Biswajit Pabi, Štepán Marek, Adwitiya Pal, Puja Kumari, Soumya Jyoti Ray, Arunabha Thakur, Richard Korytár, and Atindra Nath Pal. Resonant transport in a highly conducting single molecular junction via metal–metal covalent bond. *Nanoscale*, 15:12995–13008, 2023.

[6] Walter Kohn and Lu Jeu Sham. Self-consistent equations including exchange and correlation effects. *Phys. Rev.*, 140(4A):A1133, 1965.

[7] Eike Caldeweyher, Sebastian Ehlert, Andreas Hansen, Hagen Neugebauer, Sebastian Spicher, Christoph Bannwarth, and Stefan Grimme. A generally applicable atomic-charge dependent london dispersion correction. *J. Chem. Phys.*, 150(15):154122, 2019.

[8] Ferdinand Evers, Amnon Aharony, Nir Bar-Gill, Ora Entin-Wohlman, Per Hedegård, Oded Hod, Pavel Jelinek, Grzegorz Kamieniarz, Mikhail Lemeshko, Karen Michaeli, et al. Theory of chirality induced spin selectivity: Progress and challenges. *Adv. Mater.*, 34(13):2106629, 2022.

[9] Ricardo Gutierrez, E Díaz, Ron Naaman, and G Cuniberti. Spin-selective transport through helical molecular systems. *Phys. Rev. B*, 85(8):081404, 2012.

[10] Marc H Garner, William Bro-Jørgensen, and Gemma C Solomon. Three distinct torsion profiles of electronic transmission through linear carbon wires. *J. Phys. Chem. C*, 124(35):18968–18982, 2020.

[11] Suman Gunasekaran and Latha Venkataraman. Tight-binding analysis of helical states in carbyne. *J. Chem. Phys.*, 153(12), 2020.

[12] Rajesh Mannancherry, Michel Rickhaus, Daniel Häussinger, Alessandro Prescimone, and Marcel Mayor. Molecular dynamic staircases: all-carbon axial chiral "geländer" structures. *Chem. Sci.*, 9(26):5758–5766, 2018.

[13] Julian Antoni Skolaut. *Molecular Motor Based on Single, Chiral, Tripodal Molecules Studied with STM*. PhD thesis, Karlsruhe Institute of Technology, 2022.

[14] Lars Hedin. New method for calculating the one-particle green's function with application to the electron-gas problem. *Phys. Rev.*, 139(3A):A796, 1965.

[15] Ferdinand Kaplan. *Quasiparticle Self-Consistent GW-Approximation for Molecules: Calculation of Single-Particle Excitation Energies for Molecules*. PhD thesis, Karlsruhe Instituts für Technologie, 2015.

[16] Michiel J van Setten, Florian Weigend, and Ferdinand Evers. The gw-method for quantum chemistry applications: Theory and implementation. *J. Chem. Theory Comput.*, 9(1):232–246, 2013.

[17] M Strange, Carsten Rostgaard, H Häkkinen, and Kristian Sommer Thygesen. Self-consistent gw calculations of electronic transport in thiol-and amine-linked molecular junctions. *Phys. Rev. B*, 83(11):115108, 2011.

[18] Henrik Bruus and Karsten Flensberg. *Many-body quantum theory in condensed matter physics: an introduction*. Oxford University Press, Oxford, 2004.

[19] Gerald D. Mahan. *Many-Particle Physics*. Kluwer Academic/Plenum Publishers, 3rd edition, 2000.

[20] A Arnold, F Weigend, and Ferdinand Evers. Quantum chemistry calculations for molecules coupled to reservoirs: Formalism, implementation, and application to benzenedithiol. *J. Chem. Phys.*, 126(17):174101, 2007.

[21] Pavel Lipavský. *Teorie transportu v kondensované látce*. MATFYZPRESS, 2007.

[22] Michael Steffen Walz. *Ab initio simulations of local current densities in mesoscopic films: Current vortices in functionalized graphene nanoribbons*. PhD thesis, Universität Karlsruhe, 2015.

[23] Richard Phillips Feynman, Robert B. Leighton, and Matthew Sands. *Feynman Lectures on Physics*, volume III. Basic Books, New York, 2013.

[24] Alexei Bagrets. Spin-polarized electron transport across metal–organic molecules: A density functional theory approach. *J. Chem. Theory Comput.*, 9(6):2801–2815, 2013. PMID: 26583870.

[25] Jorge Kohanoff. *Electronic structure calculations for solids and molecules: theory and computational methods*. Cambridge university press, 2006.

[26] John P Perdew, Kieron Burke, and Matthias Ernzerhof. Generalized gradient approximation made simple. *Phys. Rev. Lett.*, 77(18):3865, 1996.

[27] Florian Weigend and Reinhart Ahlrichs. Balanced basis sets of split valence, triple zeta valence and quadruple zeta valence quality for H to Rn: Design and assessment of accuracy. *Phys. Chem. Chem. Phys.*, 7(18):3297–3305, 2005.

[28] Sree Ganesh Balasubramani, Guo P Chen, Sonia Coriani, Michael Diedenhofen, Marius S Frank, Yannick J Franzke, Filipp Furche, Robin Grotjahn, Michael E Harding, Christof Hättig, et al. Turbomole: Modular program suite for ab initio quantum-chemical and condensed-matter simulations. *J. Chem. Phys.*, 152(18):184107, 2020.

[29] Volker Blum, Ralf Gehrke, Felix Hanke, Paula Havu, Ville Havu, Xinguo Ren, Karsten Reuter, and Matthias Scheffler. Ab initio molecular simulations with numeric atom-centered orbitals. *Comput. Phys. Commun.*, 180(11):2175–2196, 2009.

[30] Karin Eichkorn, Oliver Treutler, Holger Öhm, Marco Häser, and Reinhart Ahlrichs. Auxiliary basis sets to approximate coulomb potentials. *Chem. Phys. Lett.*, 240(4):283–290, 1995.

[31] Ferdinand Kaplan, Michael E Harding, Christian Seiler, Florian Weigend, Ferdinand Evers, and Michiel Jan van Setten. Quasi-particle self-consistent gw for molecules. *J. Chem. Theory Comput.*, 12(6):2528–2541, 2016.

[32] Koichi Momma and Fujio Izumi. Vesta 3 for three-dimensional visualization of crystal, volumetric and morphology data. *J. Appl. Crystallogr.*, 44(6):1272–1276, 2011.

[33] J. D. Hunter. Matplotlib: A 2d graphics environment. *Comput. Sci. Eng.*, 9(3):90–95, 2007.

[34] Štěpán Marek. Compphysutils. `https://github.com/StepanMarek/CompPhysUtils`.

[35] Sonia Coriani, Arne Haaland, Trygve Helgaker, and Poul Jørgensen. The equilibrium structure of ferrocene. *ChemPhysChem*, 7(1):245–249, 2006.

[36] Volker Blum, Ralf Gehrke, Felix Hanke, Paula Havu, Ville Havu, Xinguo Ren, Karsten Reuter, and Matthias Scheffler. Ab initio molecular simulations with numeric atom-centered orbitals. *Comput. Phys. Commun.*, 180(11):2175–2196, 2009.

[37] Biswajit Pabi, Jakub Šebesta, Richard Korytár, Oren Tal, and Atindra Nath Pal. Structural regulation of mechanical gating in molecular junctions. *Nano Lett.*, 2023.

[38] L. D. Landau and E. M. Lifshitz. *Quantum Mechanics: Non-relativistic Theory*. Pergamon Press, Oxford, 1965.

[39] Peter W Atkins and Ronald S Friedman. *Molecular quantum mechanics*. Oxford university press, 2011.

[40] Jeff Bezanson, Alan Edelman, Stefan Karpinski, and Viral B Shah. Julia: A fresh approach to numerical computing. *SIAM review*, 59(1):65–98, 2017.

[41] Štěpán Marek. Numerical helical eigenvectors. `https://github.com/StepanMarek/NumericalHelicalEigenvectors`.

[42] Gemma C Solomon, Jeffrey R Reimers, and Noel S Hush. Overcoming computational uncertainties to reveal chemical sensitivity in single molecule conduction calculations. *J. Chem. Phys.*, 122(22):224502, 2005.

[43] Gemma C Solomon, Jeffrey R Reimers, and Noel S Hush. Single molecule conductivity: The role of junction-orbital degeneracy in the artificially high currents predicted by ab initio approaches. *J. Chem. Phys.*, 121(14):6615–6627, 2004.

[44] San-Huang Ke, Harold U Baranger, and Weitao Yang. Electron transport through single conjugated organic molecules: Basis set effects in ab initio calculations. *J. Chem. Phys.*, 127(14):144107, 2007.

[45] C. W. J. Beenakker. Random-matrix theory of quantum transport. *Rev. Mod. Phys.*, 69:731–808, 1997.

[46] Atindra Nath Pal, Dongzhe Li, Soumyajit Sarkar, Sudipto Chakrabarti, Ayelet Vilan, Leeor Kronik, Alexander Smogunov, and Oren Tal. Nonmagnetic single-molecule spin-filter based on quantum interference. *Nat. Commun.*, 10(1):5565, 2019.

[47] Štěpán Marek and Richard Korytár. Widening of the fundamental gap in cluster *GW* for metal-molecular interfaces. *Phys. Chem. Chem. Phys.*, accepted, 2023.

[48] William H. Press, Saul A. Teukolsky, William T. Vetterling, and Brian P. Flannery. *Numerical Recipes in C*. Cambridge University Press, Cambridge, 2002.

List of Figures

List of Tables

List of Abbreviations

MBJ	Molecular break junction
STM	Scanning tunnelling microscopy
NEGF	Non-equilibrium Green's function
LDOS	Local density of states
CISS	Chirality induced spin selectivity
EoM	Equation of Motion
DFT	Density functional theory
ad-atom	Adsorbed atom
evGW	Eigenvalue self-consistent GW
LUMO	Lowest unoccupied molecular orbital
HOMO	Highest occupied molecular orbital
HOMO-1	Second highest occupied molecular orbital
TZVP	Triple zeta valency with polarisation functions
HF	Hartree-Fock

List of publications

Biswajit Pabi, Štepán Marek, Adwitiya Pal, Puja Kumari, Soumya Jyoti Ray, Arunabha Thakur, Richard Korytár, and Atindra Nath Pal. Resonant transport in a highly conducting single molecular junction via metal–metal covalent bond. *Nanoscale*, 15:12995–13008, 2023

Štěpán Marek and Richard Korytár. Widening of the fundamental gap in cluster *GW* for metal-molecular interfaces. *Phys. Chem. Chem. Phys.*, accepted, 2023

A. Attachments

A.1 Green's Function Formalism

Green's functions are defined here as propagators of single particle excitations in (generally) many-body state systems. They are widely adopted due to their prevalence in perturbation theory expansions of quantum many-body Hamiltonians. Throughout the text, we use mainly these 6 different Green's functions[19]

Retarded Green's Function is defined on a many body state characterised by a density matrix $\hat{\rho}$ as a matrix in single particle basis

$$G^R_{i,j}(t,t') = -\frac{i}{\hbar}\theta(t-t')\,\mathrm{Tr}\left(\hat{\rho}\left\{\hat{a}_i(t),\hat{a}^\dagger_j(t')\right\}\right) = \tag{A.1}$$

$$= -\frac{i}{\hbar}\theta(t-t')\left\langle\left\{\hat{a}_i(t),\hat{a}^\dagger_j(t')\right\}\right\rangle\ , \tag{A.2}$$

where $\theta(t-t')$ is the Heaviside step function, Tr marks the trace over all many-body states, $\hat{a}^{(\dagger)}_i(t)$ is the annihilation (creation) operator for fermion in state i, Heisenberg propagated to time t, $\{\hat{a},\hat{b}\}$ denotes the anticommutator of $\hat{a}$ and $\hat{b}$ and $< \ldots >$ represents a shorthand for the trace with density matrix, which corresponds to the expectation value of the operator structure within.

Similarly, one can define the **advanced Green's function**

$$G^A_{i,j}(t,t') = \frac{i}{\hbar}\theta(t'-t)\left\langle\{\hat{a}_i(t),\hat{a}^\dagger_j(t')\}\right\rangle\ . \tag{A.3}$$

These Green's functions are relevant for their relation to observable parameters. In the perturbation series, one often encounters also the following four Green's functions

Greater Green's Function

$$G^>_{i,j}(t,t') = -\frac{i}{\hbar}\left\langle\hat{a}_i(t)\hat{a}^\dagger_j(t')\right\rangle\ . \tag{A.4}$$

Lesser Green's Function

$$G^<_{i,j}(t,t') = \frac{i}{\hbar}\left\langle\hat{a}^\dagger_i(t')\hat{a}_j(t)\right\rangle\ . \tag{A.5}$$

Causal Green's Function

$$G^c_{i,j}(t,t') = -\frac{i}{\hbar}\left\langle\hat{T}\left[\hat{a}_i(t)\hat{a}^\dagger_j(t')\right]\right\rangle\ , \tag{A.6}$$

where $\hat{T}$ is the time ordering operator - for $t' > t$, it swaps the creation and annihilation operator and introduces a minus sign.

Anti-causal Green's Function

$$G^{\bar{c}}_{i,j}(t,t') = -\frac{i}{\hbar}\left\langle\hat{T}\left[\hat{a}_i(t)\hat{a}^\dagger_j(t')\right]\right\rangle\ . \tag{A.7}$$

Unless otherwise stated, the "time loop"/Keldysh contour trajectory[19] for the adiabatic application of the perturbing potential is used in the perturbative

approach in this work. The complex contour ordering of the operators can be recast as a coupled system of Dyson equations as

$$\begin{pmatrix} \boldsymbol{G}^c & \boldsymbol{G}^< \\ \boldsymbol{G}^> & \boldsymbol{G}^{\bar{c}} \end{pmatrix} = \begin{pmatrix} \boldsymbol{g}^c & \boldsymbol{g}^< \\ \boldsymbol{g}^> & \boldsymbol{g}^{\bar{c}} \end{pmatrix} \left(\boldsymbol{I} + \begin{pmatrix} \boldsymbol{\Sigma}^c & \boldsymbol{\Sigma}^< \\ \boldsymbol{\Sigma}^> & \boldsymbol{\Sigma}^{\bar{c}} \end{pmatrix} \begin{pmatrix} \boldsymbol{G}^c & \boldsymbol{G}^< \\ \boldsymbol{G}^> & \boldsymbol{G}^{\bar{c}} \end{pmatrix} \right) , \tag{A.8}$$

where $\boldsymbol{g}$ are the unperturbed Green's function matrices, $\boldsymbol{\Sigma}$ are the self-energy matrices[19, 1] and inner matrix multiplication also implies time convolution, i.e.

$$\boldsymbol{\Sigma}^c \boldsymbol{G}^c \to \int dt'' \boldsymbol{\Sigma}^c(t,t'') \boldsymbol{G}^C(t'',t') \, .$$

A.1.1 Important Green's Function Identities

From the definitions of Green's functions, we can derive a number of useful identities which have further restrictions on number of free parameters in the Dyson equation (A.8). By taking difference of (A.2) and (A.3), we get

$$\begin{aligned} G^R_{i,j}(t,t') - G^A_{i,j}(t,t') = -\frac{i}{\hbar} \Big\langle & \theta(t-t') \hat{a}_i(t) \hat{a}_j^\dagger(t') + \theta(t-t') \hat{a}_j^\dagger(t') \hat{a}_i(t) + \\ & + \theta(t'-t) \hat{a}_i(t) \hat{a}_j^\dagger(t') + \theta(t'-t) \hat{a}_j^\dagger(t') \hat{a}_i(t) \Big\rangle \, , \end{aligned}$$

$$\boldsymbol{G}^R(t,t') - \boldsymbol{G}^A(t,t') = \boldsymbol{G}^>(t,t') - \boldsymbol{G}^<(t,t') \, . \tag{A.9}$$

Similarly, by taking a sum of the same pair of equations, we get

$$\boldsymbol{G}^R + \boldsymbol{G}^A = \boldsymbol{G}^c + \boldsymbol{G}^{\bar{c}} \, , \tag{A.10}$$

where we left out the time indices. Finally, by taking difference of (A.6) and (A.5) or (A.4) and evaluating the separate cases for time index ordering, we obtain

$$\boldsymbol{G}^c - \boldsymbol{G}^< = \boldsymbol{G}^R \, , \tag{A.11}$$

$$\boldsymbol{G}^c - \boldsymbol{G}^> = \boldsymbol{G}^A \, . \tag{A.12}$$

A.1.2 Green's Functions of Free Particles

For a diagonal Hamiltonian of form

$$\hat{H} = \sum_j \epsilon_j \hat{a}_j^\dagger \hat{a}_j \, , \tag{A.13}$$

the Green's functions can be determined explicitly. The retarded Green's function is given as

$$g^R_{jk}(t,t') = -\frac{i}{\hbar} \theta(t-t') \left\langle \left\{ \hat{a}_j(t), \hat{a}_k^\dagger(t') \right\} \right\rangle = -\frac{i}{\hbar} \theta(t-t') \left\langle \left\{ \hat{a}_j(t-t'), \hat{a}_k^\dagger(0) \right\} \right\rangle \, , \tag{A.14}$$

where we used the fact that the Hamiltonian is not explicitly dependent on time and used lower case g to imply non-interacting Green's function, as in [1]. Solving the Schrödinger equation for $\hat{a}_j$ leads to

$$\frac{\partial \hat{a}_j}{\partial t} = \frac{i}{\hbar} \left[\hat{H}, \hat{a}_j \right](t) = \frac{i}{\hbar} \epsilon_j (-\hat{a}_j(t)) \, . \tag{A.15}$$

The solution is then

$$\hat{a}_j(t) = e^{-\frac{i}{\hbar}\epsilon_j t}\hat{a}_j(0) \tag{A.16}$$

and the Green's function is given by

$$g^R_{jk}(t,t') = -\frac{i}{\hbar}\theta(t-t')e^{-\frac{i}{\hbar}\epsilon_j(t-t')}\delta_{jk}\,. \tag{A.17}$$

Similarly, we can obtain

$$g^A_{jk} = \frac{i}{\hbar}\theta(t'-t)e^{-\frac{i}{\hbar}\epsilon_j(t-t')}\delta_{jk} \tag{A.18}$$

and

$$g^<_{jk} = \frac{i}{\hbar}e^{-\frac{i}{\hbar}\epsilon_j(t-t')}\left\langle \hat{a}^\dagger_j\hat{a}_k\right\rangle\,. \tag{A.19}$$

Since for the free Hamiltonian, the operator in the brackets above only has diagonal elements [18], we can write the following identity (for the Fourier transform of the lesser Green's function)

$$\boldsymbol{g}^<(E) = (\boldsymbol{g}^A(E) - \boldsymbol{g}^R(E))f(E)\,, \tag{A.20}$$

where $f(E)$ is the Fermi-Dirac distribution on the equilibrium system.

A.2 Determination of the Electrode Distance

For both the perpendicular and parallel geometry of the ferrocene MBJ, we required that the geometry of the junction is as close to being symmetric as possible. This was not a necessary requirement for the parallel geometry, where the ferrocene molecule positions itself symmetrically for many electrode distances, but for perpendicular geometry, the symmetric junction is only possible for electrodes very close to each other (see Fig. A.1). Once we have a range of distances where the junction is symmetric, we choose the distance which minimizes the energy of the junction. Both of these results are shown in the figure below.

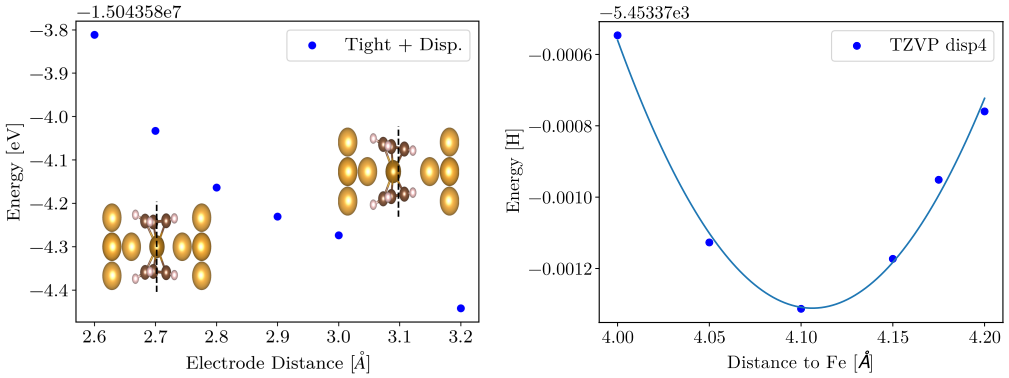

(a) Perpendicular (b) Parallel

Figure A.1: The energy dependence and junction geometry for different electrode-iron distances for perpendicular (a) and parallel (b) geometries. The parallel geometry has stable symmetric junction for all plotted values, illustration is presented in main text in Fig. 4.3a. Energies are calculated by DFT with pbe functional in FHI-AIMS for perpendicular geometry and TURBOMOLE for parallel geometry.

A.3 Convergence of TSaint Calculations

We increased the bulk unit cell to 2x1 supercell, increased the basis set size from def2-SVP to def2-TZVP and increased the number of iterations used for the determination of self-energy from 200 to 400. Furthermore, we employed both trapezoidal rule and Simpson's rule [48] for numerical spatial integration of the current density. Results are summarized in Fig. A.2

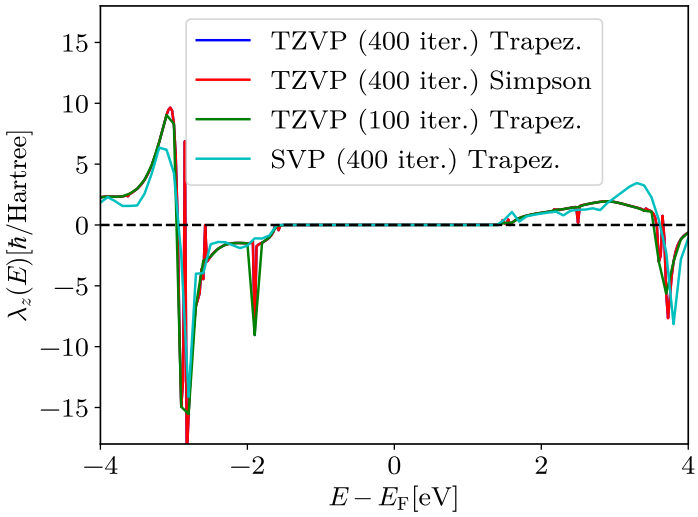

Figure A.2: While the basis size has some quantitative effect on the observed angular momentum energy density, the qualitative features do not change. The number of iterations and the integration scheme used have even weaker influence on the resulting dependence. We conclude that def2-TZVP basis is sufficient for our purposes.

A.4 Trigonometric Series for Normalisation

The normalisation constant of the eigenvectors defined in (4.20) can be derived as follows

$$1 = \langle \phi^0_{n,\alpha} | \phi^0_{n,\alpha} \rangle = Z^2 \begin{pmatrix} \sin\left(\frac{n\pi}{N+1}\right) \boldsymbol{v}_\alpha^\dagger & \sin\left(\frac{2n\pi}{N+1}\right) \boldsymbol{v}_\alpha^\dagger & \dots \end{pmatrix} \times \tag{A.21}$$

$$\times \begin{pmatrix} \sin\left(\frac{n\pi}{N+1}\right) \boldsymbol{v}_\alpha \\ \sin\left(\frac{2n\pi}{N+1}\right) \boldsymbol{v}_\alpha \\ \vdots \end{pmatrix} = Z^2 \sum_{k=1}^{N} \sin^2\left(\frac{kn\pi}{N+1}\right) . \tag{A.22}$$

We see that we are in need of analytic formula for series of trigonometric functions. These are best derived by converting the trigonometric functions to complex exponentials. For $\gamma \neq 0$, we can derive

$$\sum_{k=1}^{N} \sin(k\gamma) = \frac{1}{2i} \sum_{k=1}^{N} e^{ik\gamma} - e^{-ik\gamma} = \frac{1}{2i} \sum_{k=0}^{N-1} e^{i\gamma} e^{ik\gamma} - e^{-i\gamma} e^{ik\gamma} . \tag{A.23}$$

Using the geometric series formula

$$\sum_{k=1}^{N} \sin(k\gamma) = \frac{1}{2i} e^{i\gamma} \frac{1 - e^{i\gamma N}}{1 - e^{i\gamma}} - \frac{1}{2i} e^{-i\gamma} \frac{1 - e^{-i\gamma N}}{1 - e^{-i\gamma}} = \tag{A.24}$$

$$= \frac{e^{i\gamma} e^{i\gamma \frac{N}{2}} e^{-i\frac{\gamma}{2}}}{2i} \frac{e^{-i\gamma\frac{N}{2}} - e^{i\gamma\frac{N}{2}}}{e^{-i\frac{\gamma}{2}} - e^{i\frac{\gamma}{2}}} - \frac{e^{-i\gamma} e^{-i\gamma\frac{N}{2}} e^{i\frac{\gamma}{2}}}{2i} \frac{e^{i\gamma\frac{N}{2}} - e^{-i\gamma\frac{N}{2}}}{e^{i\frac{\gamma}{2}} - e^{-i\frac{\gamma}{2}}} = \tag{A.25}$$

$$= \frac{\sin\left(N\frac{\gamma}{2}\right)}{\sin\left(\frac{\gamma}{2}\right)} \sin\left((N+1)\frac{\gamma}{2}\right) . \tag{A.26}$$

Similarly, we can derive

$$\sum_{k=1}^{N} \cos(k\gamma) = \frac{\sin\left(N\frac{\gamma}{2}\right)}{\sin\left(\frac{\gamma}{2}\right)} \cos\left((N+1)\frac{\gamma}{2}\right) . \tag{A.27}$$

Using (A.27) in (A.22) leads to

$$1 = Z^2 \frac{1}{2} \sum_{k=1}^{N} \left(1 - \cos\left(\frac{2kn\pi}{N+1}\right)\right) = \frac{Z^2}{2} \left(N - \frac{\sin\left(\frac{Nn\pi}{N+1}\right)}{\sin\left(\frac{n\pi}{N+1}\right)} \cos(n\pi)\right) . \tag{A.28}$$

Here, we can use

$$\sin\left(\frac{Nn\pi}{N+1}\right) = \sin\left(\frac{(N+1-1)n\pi}{N+1}\right) = \tag{A.29}$$

$$= \sin(n\pi)\cos\left(\frac{n\pi}{N+1}\right) - \sin\left(\frac{n\pi}{N+1}\right)\cos(n\pi) = \tag{A.30}$$

$$= (-1)^{n+1} \sin\left(\frac{n\pi}{N+1}\right) . \tag{A.31}$$

Similarly, we could derive

$$\cos\left(\frac{Nn\pi}{N+1}\right) = (-1)^n \cos\left(\frac{n\pi}{N+1}\right) . \tag{A.32}$$

Therefore, the normalisation condition is

$$1 = \frac{Z^2}{2}\,(N+1)\ , \tag{A.33}$$

$$Z = \sqrt{\frac{2}{N+1}}\,. \tag{A.34}$$

One can also check the orthogonality of the eigenstates for $m \neq n$

$$\langle \phi^0_{m,\alpha} | \phi^0_{n,\alpha} \rangle = Z^2 \sum_{k=1}^{N} \sin\left(\frac{km\pi}{N+1}\right) \sin\left(\frac{kn\pi}{N+1}\right) = \tag{A.35}$$

$$= \frac{Z^2}{2} \sum_{k=1}^{N} \cos\left(\frac{k(m-n)\pi}{N+1}\right) - \cos\left(\frac{k(m+n)\pi}{N+1}\right) = \tag{A.36}$$

$$= \frac{Z^2}{2} \left(\frac{\sin\left(\frac{N(m-n)\pi}{N+1}\right)}{\sin\left(\frac{(m-n)\pi}{N+1}\right)} \cos\left((m-n)\pi\right) - \right. \tag{A.37}$$

$$\left. - \frac{\sin\left(\frac{N(m+n)\pi}{N+1}\right)}{\sin\left(\frac{(n+m)\pi}{N+1}\right)} \cos((m+n)\pi) \right) = 0\,. \tag{A.38}$$

A.4.1 Trigonometric Series for Helicity Matrix Elements

In the expression for helicity matrix elements, the following trigonometric series are present

$$\sum_{k=1}^{N} \sin\left(\frac{k(n \pm m)\pi}{N+1}\right) \tag{A.39}$$

Applying (A.26) leads to

$$\sum_{k=1}^{N} \sin\left(\frac{k(n \pm m)\pi}{N+1}\right) = \frac{\sin\left(\frac{(n\pm m)\pi N}{2(N+1)}\right)}{\sin\left(\frac{(n\pm m)\pi}{N+1}\right)} \sin\left(\frac{(n \pm m)\pi}{2}\right)\ . \tag{A.40}$$

The last sine is non-zero only for $n \pm m$ odd. We can also change the sine in the numerator

$$\sin\left(\frac{(n \pm m)N\pi}{2(N+1)}\right) = \sin\left(\frac{(n \pm m)\pi}{2}\right) \cos\left(\frac{(n \pm m)\pi}{2(N+1)}\right) - \tag{A.41}$$

$$- \sin\left(\frac{(n \pm m)\pi}{2(N+1)}\right) \cos\left(\frac{(n \pm m)\pi}{2}\right)\ . \tag{A.42}$$

For $n \pm m$ odd, the cosine in the last term is always zero and hence we have, for odd $n \pm m$

$$\sum_{k=1}^{N} \sin\left(\frac{k(n \pm m)\pi}{N+1}\right) = \cot\left(\frac{(n \pm m)\pi}{2(N+1)}\right) \sin^2\left((n \pm m)\frac{\pi}{2}\right) = \cot\left(\frac{(n \pm m)\pi}{2(N+1)}\right)\ , \tag{A.43}$$

since the square of the sine of $(n \pm m)\pi/2$ is always 1 for odd $n \pm m$. Therefore, we have

$$\sum_{k=1}^{N} \left(\sin\left(\frac{(n+m)\pi}{N+1}\right) + \sin\left(\frac{(n-m)\pi}{N+1}\right)\right) = \cot\left(\frac{(n+m)\pi}{2(N+1)}\right) + \cot\left(\frac{(n-m)\pi}{2(N+1)}\right) \tag{A.44}$$

for odd $n \pm m$ and zero otherwise. This can be further simplified by recognizing

$$\cot(\gamma+\eta) + \cot(\gamma-\eta) = \frac{(\cos\gamma\cos\eta - \sin\gamma\sin\eta)(\sin\gamma\cos\eta - \sin\eta\cos\gamma)}{(\sin\gamma\cos\eta + \sin\eta\cos\gamma)(\sin\gamma\cos\eta - \sin\eta\cos\gamma)} + \tag{A.45}$$

$$+ \frac{(\cos\gamma\cos\eta + \sin\gamma\sin\eta)(\sin\gamma\cos\eta + \sin\eta\cos\gamma)}{(\sin\gamma\cos\eta + \sin\eta\cos\gamma)(\sin\gamma\cos\eta - \sin\eta\cos\gamma)} = \tag{A.46}$$

$$= \frac{2\sin\gamma\cos\gamma}{\sin^2\gamma\cos^2\eta - \sin^2\eta\cos^2\gamma} = \tag{A.47}$$

$$= \frac{\sin(2\gamma)}{(1-\cos^2\gamma)\cos^2\eta - (1-\cos^2\eta)\cos^2\gamma} = \tag{A.48}$$

$$= \frac{2\sin(2\gamma)}{\cos(2\gamma) - \cos(2\eta)}\,. \tag{A.49}$$

Therefore

$$\sum_{k=1}^{N} \left(\sin\left(\frac{(n+m)\pi}{N+1}\right) + \sin\left(\frac{(n-m)\pi}{N+1}\right)\right) = \frac{2\sin\left(\frac{n\pi}{N+1}\right)}{\cos\left(\frac{n\pi}{N+1}\right) - \cos\left(\frac{m\pi}{N+1}\right)}\,. \tag{A.50}$$

A.5 Removing Rotations of p-orbital Pairs

Assume we have a generalized version of the Hückel-type Hamiltonian

$$\boldsymbol{H}_R = -t \begin{pmatrix} 0 & \boldsymbol{R}(\theta_2-\theta_1) & 0 & 0 & ... \\ \boldsymbol{R}(\theta_1-\theta_2) & 0 & \boldsymbol{R}(\theta_3-\theta_2) & 0 & ... \\ 0 & \boldsymbol{R}(\theta_2-\theta_3) & 0 & \boldsymbol{R}(\theta_4-\theta_3) & ... \\ \vdots & \vdots & \vdots & \vdots & \ddots \\ ... & ... & 0 & \boldsymbol{R}(\theta_{N-1}-\theta_N) & 0 \end{pmatrix} \tag{A.51}$$

which corresponds to local rotation of each basis pair

$$\begin{pmatrix} |x_n\rangle \\ |y_n\rangle \end{pmatrix} \to \boldsymbol{R}(\theta_n) \begin{pmatrix} |x_n\rangle \\ |y_n\rangle \end{pmatrix} \tag{A.52}$$

The unitary transformation

$$\boldsymbol{U} = \begin{pmatrix} \boldsymbol{R}(-\theta_1) & 0 & 0 & ... \\ 0 & \boldsymbol{R}(-\theta_2) & 0 & ... \\ 0 & 0 & \boldsymbol{R}(-\theta_3) & ... \\ \vdots & \vdots & \vdots & \ddots \\ ... & 0 & 0 & \boldsymbol{R}(-\theta_N) \end{pmatrix} \tag{A.53}$$

transforms the Hamiltonian to the aligned Hamiltonian given in (4.2)

$$\boldsymbol{U}^\dagger \boldsymbol{H}_R \boldsymbol{U} = -t \begin{pmatrix} \boldsymbol{R}(\theta_1) & 0 & 0 & ... \\ 0 & \boldsymbol{R}(\theta_2) & 0 & ... \\ 0 & 0 & \boldsymbol{R}(\theta_3) & ... \\ \vdots & \vdots & \vdots & \ddots \\ ... & 0 & 0 & \boldsymbol{R}(\theta_N) \end{pmatrix} \times \tag{A.54}$$

$$\times \begin{pmatrix} 0 & \boldsymbol{R}(\theta_2 - \theta_1) & 0 & ... \\ \boldsymbol{R}(\theta_1 - \theta_2) & 0 & \boldsymbol{R}(\theta_3 - \theta_2) & ... \\ 0 & \boldsymbol{R}(\theta_2 - \theta_3) & 0 & ... \\ \vdots & \vdots & \vdots & \ddots \\ ... & 0 & \boldsymbol{R}(\theta_{N-1} - \theta_N) & 0 \end{pmatrix} \times \tag{A.55}$$

$$\times \begin{pmatrix} \boldsymbol{R}(-\theta_1) & 0 & 0 & ... \\ 0 & \boldsymbol{R}(-\theta_2) & 0 & ... \\ 0 & 0 & \boldsymbol{R}(-\theta_3) & ... \\ \vdots & \vdots & \vdots & \ddots \\ ... & 0 & 0 & \boldsymbol{R}(-\theta_N) \end{pmatrix} = \tag{A.56}$$

$$= -t \begin{pmatrix} \boldsymbol{R}(\theta_1) & 0 & 0 & ... \\ 0 & \boldsymbol{R}(\theta_2) & 0 & ... \\ 0 & 0 & \boldsymbol{R}(\theta_3) & ... \\ \vdots & \vdots & \vdots & \ddots \\ ... & 0 & 0 & \boldsymbol{R}(\theta_N) \end{pmatrix} \times \tag{A.57}$$

$$\times \begin{pmatrix} 0 & \boldsymbol{R}(-\theta_1) & 0 & ... \\ \boldsymbol{R}(-\theta_2) & 0 & \boldsymbol{R}(-\theta_2) & ... \\ 0 & \boldsymbol{R}(-\theta_3) & 0 & ... \\ \vdots & \vdots & \vdots & \ddots \\ ... & 0 & \boldsymbol{R}(-\theta_N) & 0 \end{pmatrix} = -t \begin{pmatrix} 0 & \boldsymbol{I} & 0 & ... \\ \boldsymbol{I} & 0 & \boldsymbol{I} & ... \\ 0 & \boldsymbol{I} & 0 & ... \\ \vdots & \vdots & \vdots & \ddots \\ ... & 0 & \boldsymbol{I} & 0 \end{pmatrix} \tag{A.58}$$

A.6 Diagonalizing the Perturbation Matrix

With polarisation vector basis

$$\boldsymbol{v}_x = \begin{pmatrix} 1 \\ 0 \end{pmatrix} \ , \ \boldsymbol{v}_y = \begin{pmatrix} 0 \\ 1 \end{pmatrix} \ , \tag{A.59}$$

the matrix elements of $\boldsymbol{V}$ with same quantum number n states are given as (for $\xi, \xi' \in \{x, y\}$)

$$\langle \phi^0_{n,\xi} | \hat{V}' | \phi^0_{n,\xi'} \rangle = Z^2 \left(\sin\left(\tfrac{n\pi}{N+1}\right) \boldsymbol{v}_\xi^\dagger \quad \sin\left(\tfrac{2n\pi}{N+1}\right) \boldsymbol{v}_\xi^\dagger \quad ... \quad \sin\left(\tfrac{Nn\pi}{N+1}\right) \boldsymbol{v}_\xi^\dagger \right) \times \tag{A.60}$$

$$\times \begin{pmatrix} \sin\left(\tfrac{n\pi}{N+1}\right) \boldsymbol{\epsilon} \boldsymbol{v}_{\xi'} \\ \mathbf{0} \\ \vdots \\ \mathbf{0} \\ \sin\left(\tfrac{Nn\pi}{N+1}\right) \boldsymbol{R}(\theta_\mathrm{T}) \boldsymbol{\epsilon} \boldsymbol{R}(\theta_\mathrm{T})^\dagger \boldsymbol{v}_{\xi'} \end{pmatrix} = \tag{A.61}$$

$$= Z^2 \sin^2\left(\frac{n\pi}{N+1}\right) \left(\boldsymbol{v}_\xi^\dagger \boldsymbol{\epsilon} \boldsymbol{v}_{\xi'} + \boldsymbol{v}_\xi^\dagger \boldsymbol{R}(\theta_\mathrm{T}) \boldsymbol{\epsilon} \boldsymbol{R}(-\theta_\mathrm{T}) \boldsymbol{v}_{\xi'} \right) , \tag{A.62}$$

The second term in the bracket evaluates to

$$\boldsymbol{v}_\xi^\dagger \begin{pmatrix} \cos(\theta_\mathrm{T}) & -\sin(\theta_\mathrm{T}) \\ \sin(\theta_\mathrm{T}) & \cos(\theta_\mathrm{T}) \end{pmatrix} \begin{pmatrix} 0 & 0 \\ 0 & \epsilon \end{pmatrix} \times \tag{A.63}$$

$$\times \begin{pmatrix} \cos(\theta_\mathrm{T}) & \sin(\theta_\mathrm{T}) \\ -\sin(\theta_\mathrm{T}) & \cos(\theta_\mathrm{T}) \end{pmatrix} \boldsymbol{v}_{\xi'} = \tag{A.64}$$

$$= \epsilon \boldsymbol{v}_\xi^\dagger \begin{pmatrix} \sin^2(\theta_\mathrm{T}) & -\sin(\theta_\mathrm{T})\cos(\theta_\mathrm{T}) \\ -\sin(\theta_\mathrm{T})\cos(\theta_\mathrm{T}) & \cos^2(\theta_\mathrm{T}) \end{pmatrix} \boldsymbol{v}_{\xi'} = \tag{A.65}$$

$$= \epsilon \Big((\boldsymbol{v}_\xi)_1 (\boldsymbol{v}_{\xi'})_1 \sin^2(\theta_\mathrm{T}) - \tag{A.66}$$

$$- \left((\boldsymbol{v}_\xi)_1 (\boldsymbol{v}_{\xi'})_2 + (\boldsymbol{v}_\xi)_2 (\boldsymbol{v}_{\xi'})_1 \right) \sin(\theta_\mathrm{T}) \cos(\theta_\mathrm{T}) + \tag{A.67}$$

$$+ (\boldsymbol{v}_\xi)_2 (\boldsymbol{v}_{\xi'})_2 \cos^2(\theta_\mathrm{T}) \Big) . \tag{A.68}$$

Therefore, for different combinations of basis vectors $\boldsymbol{v}_\xi$, we have

$$\langle \phi^0_{n,x} | \hat{V} | \phi^0_{n,x} \rangle = \epsilon Z^2 \sin^2\left(\frac{n\pi}{N+1}\right) \sin^2(\theta_\mathrm{T}) \tag{A.69}$$

$$\langle \phi^0_{n,x} | \hat{V} | \phi^0_{n,y} \rangle = \epsilon Z^2 \sin^2\left(\frac{n\pi}{N+1}\right) (-\sin(\theta_\mathrm{T})\cos(\theta_\mathrm{T})) = \langle \phi^0_{n,y} | \hat{V} | \phi^0_{n,x} \rangle \tag{A.70}$$

$$\langle \phi^0_{n,y} | \hat{V} | \phi^0_{n,y} \rangle = \epsilon Z^2 \sin^2\left(\frac{n\pi}{N+1}\right) \left(1 + \cos^2(\theta_\mathrm{T})\right) \tag{A.71}$$

A.6.1 Matrix Elements for Different Quantum Numbers

For different quantum numbers $m \neq n$, the matrix elements of $\boldsymbol{V}$ can be derived as

$$\langle \phi^0_{m,\xi} | \hat{V} | \phi^0_{n,\xi'} \rangle = Z^2 \left(\sin\left(\tfrac{m\pi}{N+1}\right) \boldsymbol{v}_\xi^\dagger \quad \sin\left(\tfrac{2m\pi}{N+1}\right) \boldsymbol{v}_\xi^\dagger \quad ... \right) \times \tag{A.72}$$

$$\times \begin{pmatrix} \sin\left(\tfrac{n\pi}{N+1}\right) \boldsymbol{\epsilon} \boldsymbol{v}_{\xi'} \\ \mathbf{0} \\ \vdots \\ \mathbf{0} \\ \sin\left(\tfrac{Nn\pi}{N+1}\right) \boldsymbol{R}(\theta_\mathrm{T} \boldsymbol{\epsilon} \boldsymbol{R}(\theta_\mathrm{T})^\dagger \boldsymbol{v}_{\xi'} \end{pmatrix} , \tag{A.73}$$

$$\langle \phi^0_{m,\xi} | \hat{V} | \phi^0_{n,\xi'} \rangle = \epsilon Z^2 \sin\left(\frac{n\pi}{N+1}\right) \sin\left(\frac{m\pi}{N+1}\right) ((\boldsymbol{v}_\xi)_2 (\boldsymbol{v}_{\xi'})_2 + \tag{A.74}$$

$$+ \frac{(-1)^{m+n}}{\epsilon} \boldsymbol{v}^\dagger_\xi \boldsymbol{R}(\theta_\mathrm{T}) \boldsymbol{\epsilon} \boldsymbol{R}(\theta_\mathrm{T})^\dagger \boldsymbol{v}_{\xi'} \Bigg) \ . \tag{A.75}$$

Now, choosing the polarisation basis which diagonalizes the perturbation for same quantum number (see (4.31)), we obtain

$$\langle \phi^0_{m,\xi} | \hat{V} | \phi^0_{n,\xi'} \rangle = \epsilon Z^2 \sin\left(\frac{n\pi}{N+1}\right) \sin\left(\frac{m\pi}{N+1}\right) \times \tag{A.76}$$

$$\times \begin{pmatrix} \cos^2(\theta_\mathrm{T}/2)\left((-1)^{m+n}+1\right) & \sin(\theta_\mathrm{T}/2)\cos(\theta_\mathrm{T}/2)\left((-1)^{m+n}-1\right) \\ \sin(\theta_\mathrm{T}/2)\cos(\theta_\mathrm{T}/2)\left((-1)^{m+n}-1\right) & \sin^2(\theta_\mathrm{T}/2)\left((-1)^{m+n}+1\right) \end{pmatrix} . \tag{A.77}$$

A.7 Cluster Averages

We expect that for the metallic clusters, energy levels around the Fermi energy are described by combination of true uniform spacing and random error on these spacings, i.e. energy level indexed by number n lies at

$$E_{n,c} = \epsilon_0 + n\Delta + \delta_{n,c} \,, \tag{A.78}$$

where ϵ_0 is some reference quasiparticle level, Δ is the average level spacing and $\delta_{n,c}$ is the random energy shift of the level n in cluster c, caused by various factors, such as presence of unintended symmetries in the cluster geometry etc.

In our ensemble of clusters, clusters of the same size are present in multiple realisations through the addition of extra atoms (add-atoms), which are meant to break some of the unintended symmetries of the clusters. Therefore, we expect that $\delta_{n,c}$ is different for different cluster realisations.

We model the energy shift $\delta_{n,c}$ as uncorrelated between different cluster realisations and between different levels. Therefore, each $\delta_{n,c}$ is treated as separate realisation of some random variable δ.

The central question is how to determine Δ and standard error on its estimate based on different cluster realisations. One approach is to determine the average spacing for a single cluster and then do averaging over different realisations, other approach is to first determine average electronic structure for different cluster realisations and only then move to level differences. In the following text, we show that both approaches lead to the same results.

A.7.1 Mean and Variance of Energy Levels

Taking average energy difference for a single cluster gives us average

$$< \Delta >_c = \frac{1}{M-1} \sum_{n=0}^{M-1} E_{n+1,c} - E_{n,c} = \Delta + \frac{1}{M-1} \sum_{n=0}^{M-1} \delta_{n+1,c} - \delta_{n,c} = \tag{A.79}$$

$$= \Delta + \frac{1}{M-1}(\delta_{M,c} - \delta_{0,c}) \,, \tag{A.80}$$

where M is the number of energy levels of the same kind (occupied or unoccupied) and c determines the specific cluster realisation. Averaging the result over the N different cluster realisations leads to true average

$$< \Delta >= \frac{1}{N} \sum_{c}^{N} < \Delta >_c = \Delta + \frac{1}{N(M-1)} \sum_{c}^{N} \delta_{M,c} - \delta_{0,c} \,. \tag{A.81}$$

Swapping the order of the summation does not change the final sum over the energy shifts - if we first summed over the different cluster realisations, we would get average energy level placement

$$< E_n >= \frac{1}{N} \sum_{c}^{N} E_{n,c} = \epsilon_0 + n\Delta + \frac{1}{N} \sum_{c} \delta_{n,c} \,. \tag{A.82}$$

Now, averaging over the different energy levels leads to the same final expression

$$\frac{1}{M-1}\sum_{n=0}^{M-1} < E_{n+1} > - < E_n > = \Delta + \tag{A.83}$$

$$+ \frac{1}{N(M-1)}\sum_{c}^{N}\sum_{n=0}^{M-1} \delta_{n+1,c} - \delta_{n,c} =< \Delta > \ . \tag{A.84}$$

The standard error $\sigma(\Delta)$ is then determined from the variance as determined on the whole ensemble of clusters + levels. The variance of the spacing Δ is determined as

$$\mathrm{var}(\Delta) = \frac{1}{N(M-1)}\sum_{c}^{N}\sum_{n=0}^{M-1}(E_{n+1,c} - E_{n,c} - < \Delta >)^2 \tag{A.85}$$

and so the standard error

$$\sigma(\Delta) = \sqrt{\frac{\mathrm{var}(\Delta)}{N(M-1)}}\,. \tag{A.86}$$

A.8 Convergence in Cluster Calculations

The TURBOMOLE DFT and HF calculations converge to relative error in total energy of 10^{-7}, i.e. for total energy E_0 and change in energy ΔE between iterations, the convergence criterion is

$$\left|\frac{\Delta E}{E_0}\right| \leq 10^{-7} \tag{A.87}$$

The geometrical relaxation is carried out so that the elements of the gradient of total energy with respect to the atomic positions of ions are less than 0.001 a.u. and the relative energy change in the geometric optimisation steps is less than 10^{-6}.

The effect of basis set size is shown in Fig. A.3 for DFT calculations, in Fig. A.4 for evGW calculations and in Fig. A.5 for HF calculations.

The effect of different exchange-correlation functional is shown in Fig. A.6. The evGW calculation starting from the DFT calculation with given functional can also show some functional dependence, but it is weak, as shown in Fig. A.7.

A.8.1 Basis Size

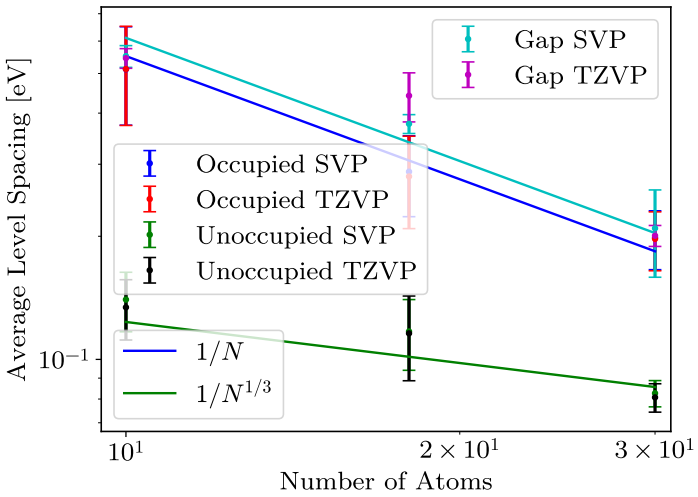

Figure A.3: Electronic structure indicators for different basis set sizes from DFT. The average values are essentially indistinguishable between the smaller and larger basis set.

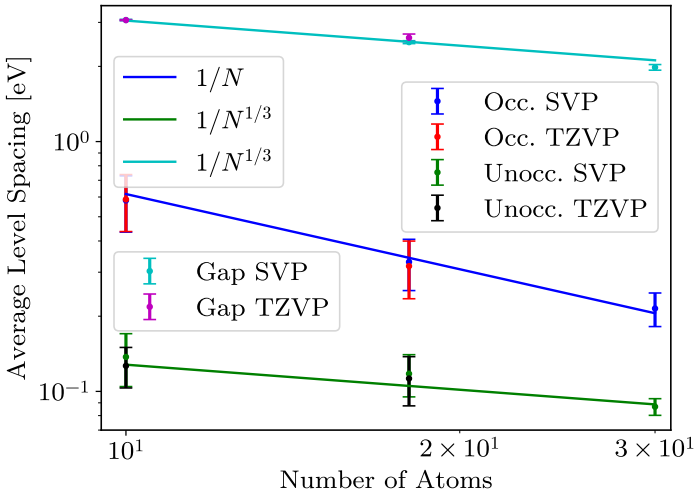

Figure A.4: Electronic structure indicators for different basis set sizes from evGW. The average values are essentially indistinguishable between the smaller and larger basis set.

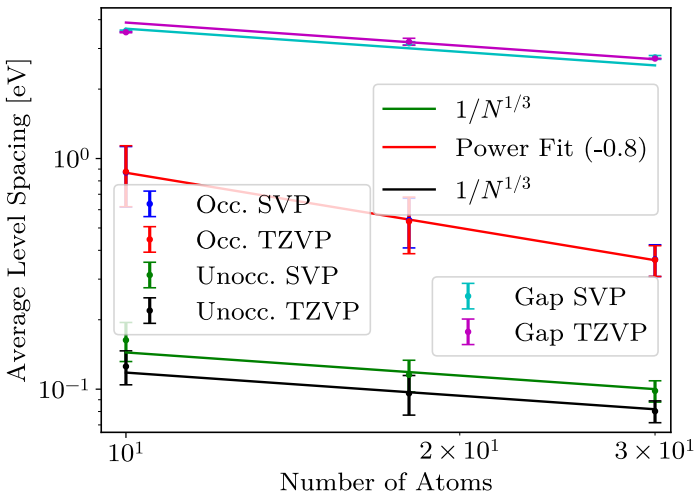

Figure A.5: Electronic structure indicators for different basis set sizes from HF. The unoccupied states show some unconverged behaviour, but the gap and the occupied states are converged for given basis set sizes.

A.8.2 Functional

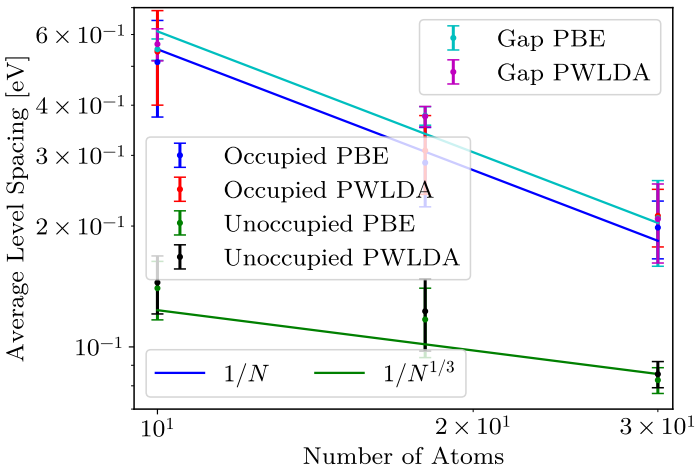

Figure A.6: Electronic structure indicators for different exchange-correlation functionals in DFT. The average values are essentially indistinguishable for different functionals.

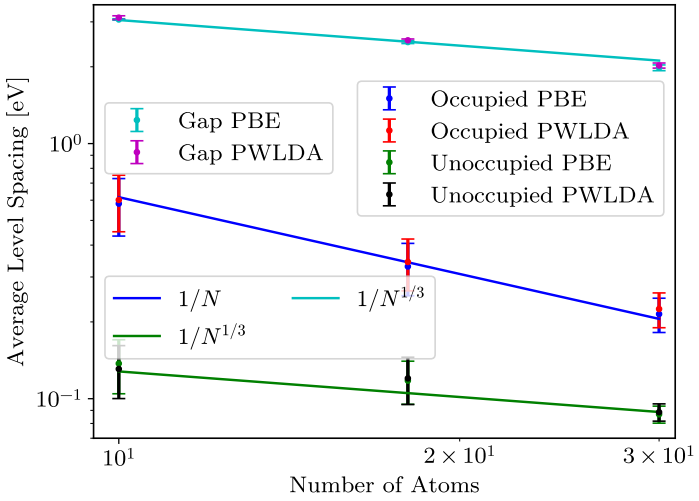

Figure A.7: Electronic structure indicators for different exchange-correlation functionals in evGW. The average values are essentially indistinguishable for different functionals.